Three Dimensional Reconstruction of the Tectorial Membrane: An Image Processing Method using Nomarski Differential Interference Contrast Microscopy

by

Kristin J. Dana

Submitted to the Department of Electrical Engineering and
Computer Science
in partial fulfillment of the requirements for the degree of

Master of Science in Electrical Engineering and Computer Science

at the

MASSACHUSETTS INSTITUTE OF TECHNOLOGY

May 1992

© Kristin J. Dana, MCMXCII.

Author . . . . / . . . .
Department of Electrical Engineering and Computer Science
May 18, 1992

Certified by . . . .
Dennis M. Freeman
Research Scientist
Thesis Supervisor

Accepted by . . . .
Campbell L. Searle
Chairman, Departmental Committee on Graduate Students

Three Dimensional Reconstruction of the Tectorial Membrane: An Image Processing Method using Nomarski Differential Interference Contrast Microscopy

by

Kristin J. Dana

Submitted to the Department of Electrical Engineering and Computer Science
on May 18, 1992, in partial fulfillment of the
requirements for the degree of
Master of Science in Electrical Engineering and Computer Science

Abstract

Signal processing methods are developed to estimate the three dimensional structure of a specimen from images obtained with a light microscope equipped with Nomarski Differential Interference Contrast (DIC) optics. Physical processes underlying image formation are modelled as a linear system that converts refractive index to light intensity. These processes include diffraction by a finite aperture and differential interference.

Methods for empirically determining the signal processing properties of a DIC microscope are developed. Images of a polystyrene microsphere are used to estimate the three-dimensional impulse response (point spread function) of the microscope. Noise and other degradations of measured images are also characterized. Measured signal processing properties of the microscope are shown to differ in significant ways from the theory.

Three-dimensional intensity patterns are obtained from optical sections, i.e. from images taken at a sequence of focal planes. However, images from a DIC microscope are difficult to interpret; the intensity patterns exhibit a shadowing effect and are blurred. Deconvolution methods are developed to estimate the underlying structure of the specimen and thereby simplify interpretation. These methods are applied to the tectorial membrane (a structure in the inner ear) of the alligator lizard.

Thesis Supervisor: Dennis M. Freeman
Title: Research Scientist

Acknowledgments

First, I would like to express a special thanks to Quentin Davis and Denny Freeman for their enormous help with final preparations of this thesis. During the last week, I developed tendonitis in both wrists, leaving me unable to type. Denny and Quentin readily agreed to share the hectic workload of final preparation. It was only through their hard work (really hard work) that I was able to finish. I cannot thank them enough.

During the project, my advisor Denny provided assistance, encouragement, and guidance. His was always willing to spend long hours brainstorming about new ideas, explaining concepts, and offering helpful criticism. His competence, kindness, and sense of humor created a work environment that was both fun and challenging. His concern for students generated a family-like atmosphere in our group that was quite contrary to what I expected from a large institution like MIT.

Tom Weiss was another source of support and guidance in this project. He helped in many stages of the work, from the initial development of the project's goals to patiently helping me communicate the results in writing. He made time for weekly meetings and enthusiastically followed the progress of my work.

My officemates Quentin and Farzad Eshani provided help and support throughout the thesis work. Sharing an office with friends who are helpful and fun to be around was a pleasure. I would also like to thank my friends Seema, Aradhana, and Rachel for making MIT a more pleasant place.

I would like to thank Jae Lim for letting me use his photo-quality printer to make the plates in this thesis.

I extend (another) thanks to Quentin for performing the surgeries for the TM's shown in this thesis.

My parents were terrific, as usual. I am lucky to have them. My fiancé David has been patient and understanding throughout this work. His love and encouragement helped me through the hard times.

Contents

Chapter 1

Introduction

Background

The tectorial membrane (TM) is an inner ear structure that may have an important role in the micromechanics of hearing. Primary sensory receptors in hearing are hair bundles located in the inner ear. The tectorial membrane is a transparent, gelatinous structure that comes in direct contact with hair bundles. This location suggests the TM may have an important role in the mechanics of hair bundle displacement. However, because the properties of the TM are not well understood, its role is not well known.

Studying the properties of the TM is difficult. The first complication arises from the goal of studying the TM in its normal chemical environment. Any changes in the chemical environment may cause a change the the TM's structure[19, 4]. The second complicating factor is the transparency of the TM. Staining and serial sectioning are often used to study transparent biological tissues. This method would certainly allow observations of the TM's transparent structure, but it would not maintain the TM's normal chemical environment. Scanning electron microscopy techniques can also be used for viewing transparent specimens. However, the specimen is typically prepared by dehydration and coated with a conductive material. This preparation does not meet the goal of maintaining the TM's normal chemical environment.

Optics

There are several advantages of using light microscopy when studying biological specimens. The use of a light microscope allows observations of a specimen while it is immersed in a solution that simulates its normal chemical environment. Also, transmission light microscopy optically sections transparent specimens. Optical sectioning is best understood by an analogy to physical sectioning. When we physically section

a specimen, we cut it into slices and view each slice individually. We observe structures in three dimensions, one plane at a time. Similarly, optical sectioning refers to viewing only the in-focus plane through a microscope. When the focus is changed by adjusting the microscope's focus-control knob, we view a different plane through the specimen. The light through a specimen in a transmission light microscope is focused onto one plane at a time, imaging each "section" of the specimen individually without cutting the specimen into physical sections. Therefore, the microscope can be thought of as a three dimensional (3D) imaging device which translates a 3D specimen into a 3D distribution of intensity.

The optical sectioning property of the microscope is not perfect. Diffraction blurs information from neighboring planes into the in-focus plane. Diffraction also causes blurring within the in-focus plane.

Interference methods such as Nomarski Differential Interference Contrast (DIC) Microscopy can be employed to facilitate viewing transparent specimens under a light microscope. DIC optics split light rays into two rays that pass through the specimen at adjacent locations. Phase differences between rays are translated into intensities. Therefore, the intensity from a DIC microscope is a function of refractive index gradients in the specimen.

Signal Processing

In the past the microscope has been used primarily for qualitative studies. Recently, with the use of computers and video cameras, the microscope can be used as a quantitative measurement device; light intensity from the specimen is digitally recorded on a computer. The goal of this project is to relate measurements of the 3D distribution of intensity to the properties of the specimen. To take advantage of well-developed signal-processing methods, we interpret the specimen and its corresponding intensity measurements as three-dimensional (3D) signals. The 3D specimen signal is converted by a system (the DIC microscope) to a 3D intensity signal. By modelling the physical processes of diffraction and interference as linear system transformations, we characterize the effect of the system. We use signal processing methods to determine an estimate of the specimen based on observations of the intensities. Specifically, Weiner deconvolution is performed. The Weiner deconvolution filter inverts the effect of the system at spatial frequencies where the signal-to-noise power in the measurement is high.

The first test of the methods involve simulated microscope images of spherical objects. We then show results for spherical objects imaged with our microscope. Finally, we show applications of these methods to the tectorial membrane (TM).

7

Chapter 2

Signal Processing Model of the Microscope

To quantitatively analyze the images obtained from our microscope we first investigate the physical principles leading to the image formation. We introduce signal processing transformations to model these principles and combine these transformations to form a signal processing model of a DIC microscope.

2.1   Diffraction Point Spread Function

We first consider the microscope image produced by an object of infinitesimal size, i.e. a point source. Ideally, the image of this point source would simply be a point. In this ideal imaging system, even objects separated by infinitesimal distances would be resolved. Of course, this is not the case in practice. The optical elements in a microscope have finite apertures that cause diffraction. This finite aperture diffraction blurs the image of a point source. We refer to this blurred image of a point source as the diffraction point spread function (PSF) of the microscope.

Compound microscopes consist of a complex collection of lenses and apertures. A theoretical computation of the effective diffraction PSF should take into account the contribution from each optical component. However, the objective lens is usually the greatest source of blurring and the effects of other sources are generally small in comparison [10]. Thus we model the diffraction PSF of the microscope by that of a single lens that focuses the light from a specimen. Even with the reduction to a single lens, there are several effects to be considered. The light distribution at the focus is affected not only by the extent of the aperture, but also by lens imperfections such as astigmatism, coma, chromatic aberrations and spherical aberrations. Modern microscope optics are generally well corrected and the finite aperture of the objective lens is usually the limiting factor. When this is the case, we say the microscope image

is diffraction limited. The problem then reduces to examining the theoretical point spread function resulting when light incident on an aperture converges to a focal point.

It is convenient to use principles of Fourier optics in order to understand this aperture problem. With some approximations (See [8]), diffraction causes the light distribution in the focal plane of the lens to be the Fourier transform of the incident light on the lens. If the lens has infinite extent and the incident light is a uniform plane wave, the light in the focal plane will be a single point. This is equivalent to saying that the Fourier transform of a constant is an impulse function. However since no lens is infinite in extent, the resulting light distribution will be the Fourier transform of the aperture. For the case of a circular aperture, the light amplitude in the focal plane is a Bessel function. The intensity of this light in the focal plane is the familiar Airy pattern [10]. Because the finite aperture causes one point to be blurred into an Airy pattern in the focal plane, the resolution of an imaging system such as the microscope is fundamentally limited.

In addition to blurring a point into an Airy disk in the focal plane, diffraction also causes blurring into planes above and below the focal plane. We can characterize the three dimensional light distribution around the focus of a lens by evaluating the Huygens-Fresnel diffraction integral (See [3]). The three dimensional distribution of the light intensity around the focus is the diffraction PSF. Define a reference coordinate frame so that the x-y plane is parallel to the microscope stage and z is parallel to the microscope's optical axis. The origin is located at the focus. Let γ_x, γ_y, and γ_z denote the position coordinates in this reference frame. The finite aperture diffraction PSF $h_a(\gamma_x, \gamma_y, \gamma_z)$ can be expressed [3] as

$$h_a(\gamma_x, \gamma_y, \gamma_z) = \left(\frac{2}{u}\right)^2 [U_1^2(u, v) + U_2^2(u, v)]I_o, \qquad (2.1)$$

where $U_n(u, v)$ is the Lommel function and u, v can be determined from γ_x, γ_y, and γ_z using

$$u = \frac{2\pi}{\lambda} \left(\frac{a}{f}\right)^2 \gamma_z \qquad (2.2)$$

and

$$v = \frac{2\pi}{\lambda} \left(\frac{a}{f}\right) \sqrt{\gamma_x{}^2 + \gamma_y{}^2}. \qquad (2.3)$$

The symbol a is the aperture radius, f is the distance from the aperture to the focus, λ is the wavelength, and I_o is the intensity at the focal point. The Lommel function can be evaluated as

$$U_n(u, v) = \Sigma_{s=0}^{\infty}(-1)^s \left(\frac{u}{v}\right)^{n+2s} J_{n+2s}(v), \qquad (2.4)$$
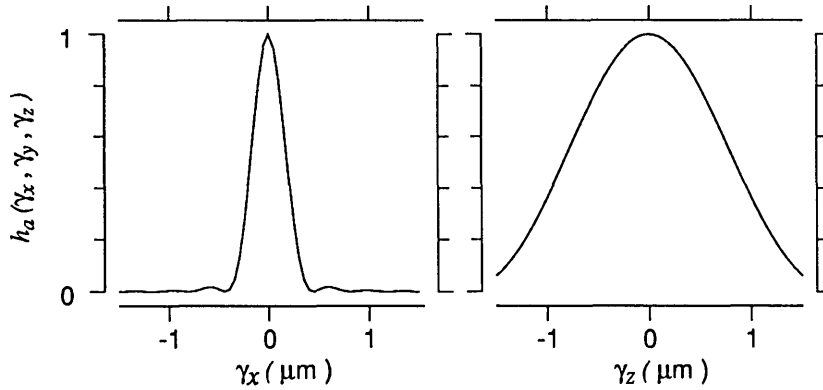
9

Figure 2-1: The theoretical diffraction point spread function $h_a(\gamma_x, \gamma_y, \gamma_z)$. Equation 2.1 has been evaluated for $a = 3.5$ mm and $f = 4.6$ mm, which are typical values for a Zeiss WL microscope with a 0.75 NA, 1.6 mm working distance, 40X objective. The left panel shows the resulting dependence of intensity on distance along x in the plane of the stage. This dependence is the same along any line in this plane that passes through the origin, i.e. the PSF is cylindrically symmetric. The right panel shows the dependence on distance along the optical axis (z).

where $J_n(v)$ represents a Bessel function of the first kind.

Figure 2-1 illustrates the PSF of Equation 2.1 evaluated for parameters appropriate for a long working distance (1.6mm), water immersion objective (Zeiss 40X, NA = 0.75). Notice that the PSF is not spherically symmetric; blurring along the optical axis is much greater than blurring perpendicular to the optical axis. The PSF is cylindrically symmetric about the optical axis. Furthermore, there is a mirror symmetry about the plane $\gamma_z = 0$.

This three dimensional PSF complicates quantitative interpretation of microscope images. Consider that even a simple spherical specimen appears as a blurred ellipsoid. To interpret this blurred ellipsoid as a sphere, one must explicitly account for the three dimensional PSF.

10

2.2 Operating Principles of DIC Microscopy

Many biological tissues are transparent and therefore difficult to study with ordinary optical methods. However, interference methods can be employed to convert differences in refractive index that are present in the specimen into differences in intensities. Nomarski Differential Interference Contrast (DIC) microscopy is one such interference method. This section provides the background necessary for a quantitative understanding of DIC . Further details about the operation of the DIC microscope are available elsewhere [12, 16, 15, 6, 9].

In DIC microscopy the incoming light is split into two coherent waves. Rays from these waves are separated by a small distance in the plane of the microscope stage. After passing through the specimen the two waves are recombined. The waves then interfere so that the resulting intensity is a function of the phase difference between the waves. Therefore differences in the index of refraction between two neighboring points in the specimen will produce a difference in the intensity. It is in this manner that DIC enhances the visibility of the edges of a transparent specimen. To accomplish the task of ray splitting and interference a DIC microscope must be equipped with special optics. In a compound microscope, light from a condenser passes through the specimen and is focused by an objective to form an image. The optical train of a DIC microscope includes additional components both before the condenser and after the objective. As illustrated in Figure 2-3, these components include a pair of polarizers and a pair of prisms. The ray splitting and recombination is the function of the prisms, and creating conditions necessary for interference is the function of the polarizers. We first describe the physical principles necessary to understand each components' role in ray splitting, recombination and interference. We then use these principles to trace the path and phase of light as it passes through each element of the microscope.

2.2.1 Physical Principles

Birefringence

To understand how a ray is split by a prism in a DIC microscope, the property of birefringence must be examined. In a uniaxial birefringent crystal, relations between the electric field vector $\mathbf{E}$ and the electric displacement vector $\mathbf{D}$ depend on direction. For a uniaxial birefringent crystal, $\mathbf{D} = \epsilon_{\parallel}\mathbf{E}$ if $\mathbf{E}$ is parallel to the crystal axis and $\mathbf{D} = \epsilon_{\perp}\mathbf{E}$ if $\mathbf{E}$ is perpendicular to the crystal axis. As a result of this anisotropy, an incident wave causes two waves to propagate inside the crystal [1]. The refractive indices and the phase velocities for each of the waves are different. These waves are usually referred to

---

[1]This result and the properties of the two waves can be derived using Maxwell's equations (See [3]).

as the o-wave and e-wave. Because of the permittivity direction dependence, the speed and refractive index of one these waves (e-wave) is dependent on the propagation direction with respect to the crystal axis. To understand the operating principles of DIC , the case in which the propagation direction is perpendicular to the crystal axis is important. For this special case, the function of a uniaxial crystal is especially simple. If $\mathbf{E}$ is parallel to the crystal axis, the phase velocity is $v_\parallel$ and the refractive index is $n_\parallel$. However, if $\mathbf{E}$ is perpendicular to the crystal axis, the phase velocity is $v_\perp$ and the refractive index is $n_\perp$.

The Wollaston Prism

A Wollaston prism is constructed from two uniaxial birefringent crystals cut at an angle α and cemented together (Figure 2-2). It is convenient to discuss the prism in a coordinate system with basis vectors $\mathbf{s}$, $\mathbf{t}$, and $\mathbf{z}$ aligned with the crystal axes. In a DIC microscope this coordinate system is rotated 45° counterclockwise about $\mathbf{z}$ with respect to the reference coordinate system which has the basis vectors $\mathbf{x}$, $\mathbf{y}$, and $\mathbf{z}$. That is, the prism coordinate axes $\mathbf{s}$, $\mathbf{t}$, and $\mathbf{z}$, are related to the reference coordinate axes $\mathbf{x}$, $\mathbf{y}$, and $\mathbf{z}$ as follows

$$
\begin{bmatrix} \mathbf{s} \\ \mathbf{t} \\ \mathbf{z} \end{bmatrix} = \frac{1}{2} \begin{bmatrix} \sqrt{2} & \sqrt{2} & 0 \\ -\sqrt{2} & \sqrt{2} & 0 \\ 0 & 0 & 2 \end{bmatrix} \begin{bmatrix} \mathbf{x} \\ \mathbf{y} \\ \mathbf{z} \end{bmatrix} .
$$

The prism causes light that is originally traveling in the $\mathbf{z}$ direction to be refracted about the $\mathbf{t}$ axis. However the amount of refraction depends on the orientation of the electric field vector. If the electric field vector of the incident ray is in the $\mathbf{s}$ direction, then the refractive index changes from $n_\parallel$ to $n_\perp$ as the ray passes between the two crystals. However, if the electric field vector of the incident ray is in the $\mathbf{t}$ direction, then the index of refraction changes from $n_\perp$ to $n_\parallel$ as the ray passes between the two crystals. Additional refraction occurs as the rays exit the Wollaston prism.

If the electric field vector of the incident ray had components in both the $\mathbf{s}$ and $\mathbf{t}$ directions, the net effect of the Wollaston prism is to split the ray into two rays propagating in slightly different directions (Figure 2-3). The angular separation of the rays is typically on the order of 0.001 radians [16]. Because the effective index of refraction is different for each ray, the rays also differ in phase as they exit the prism.

Light through a DIC microscope passes through two Wollaston prisms:[2] the compensator prism, which precedes the condenser in the optical train; and the slider prism, which follows the objective. The two prisms of a DIC microscope are oriented so that spatial differences in phase introduced by the first prism are canceled by the second prism. This cancellation is referred to as phase compensation (Figure 2-4).

---

[2]The DIC microscope uses a slightly different configuration called a modified Wollaston prism. We ignore this distinction since it is not essential for understanding DIC .
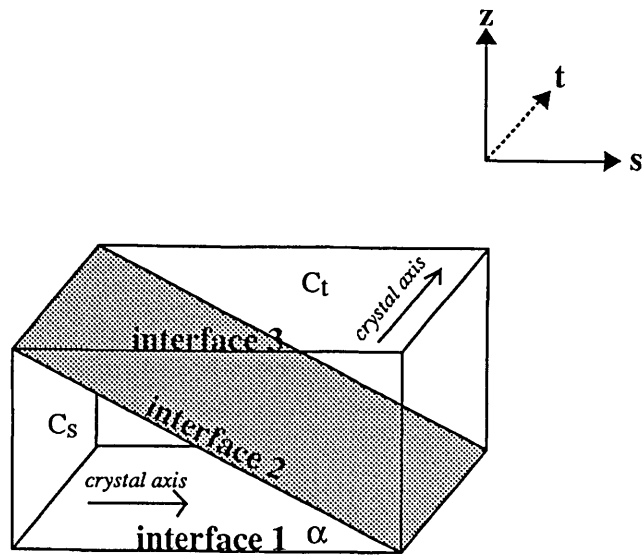
Figure 2-2: The Wollaston Prism. C_s and C_t represent uniaxial birefringent crystals with crystal axes in the s and t directions respectively. Each crystal is wedge-shaped; the angle α of the wedge is very small, but is exaggerated here for clarity. Light passes through the Wollaston prism in the direction of z which corresponds to the microscope's optical axis.

Emerging Light

Analyzer

C_s α $\otimes$ C_t **Slider Prism**

z

t

s

Objective

◁······· **Specimen Plane**

Condenser

C_s $\otimes$ C_t **Compensator Prism**
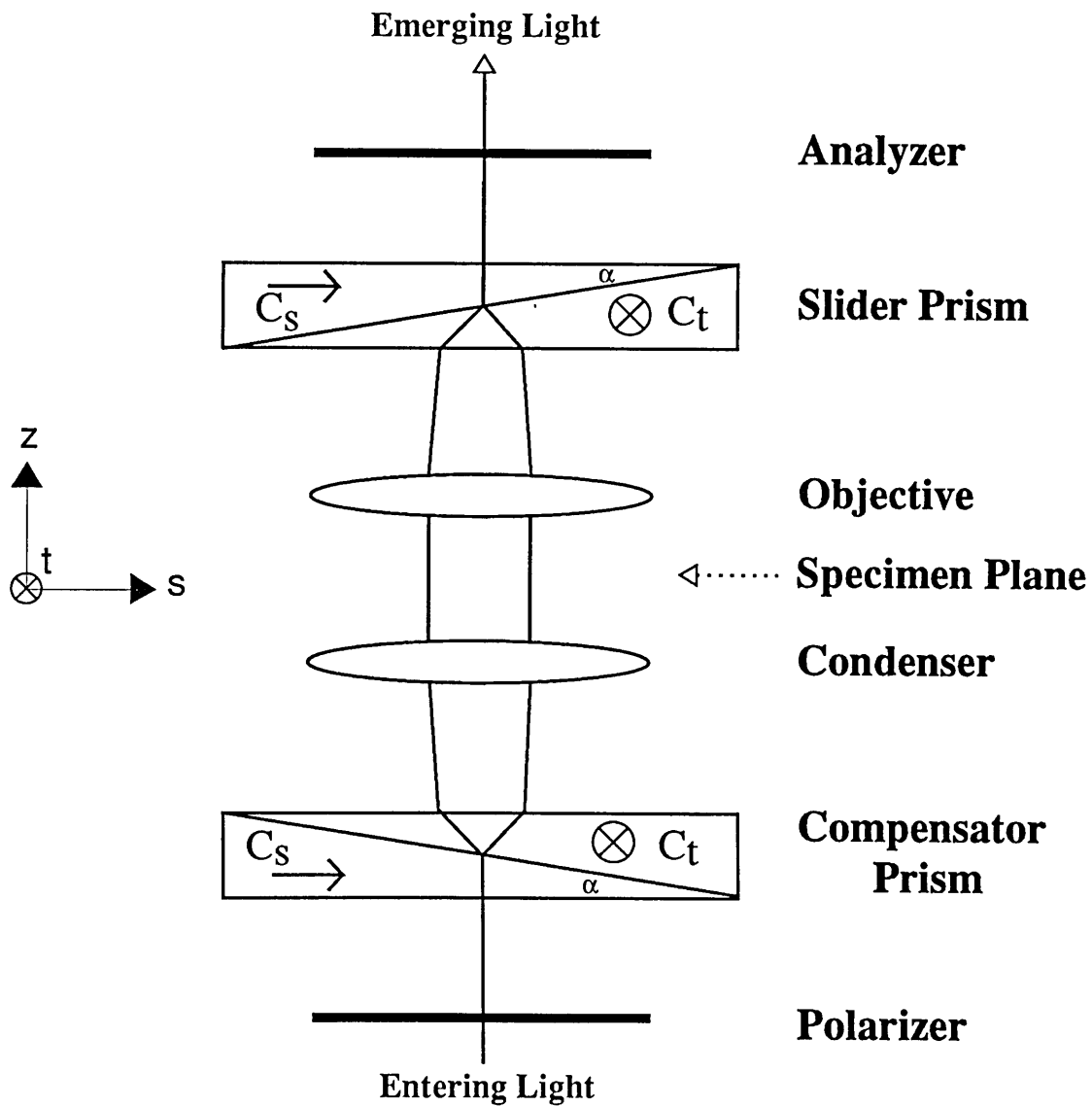
α

Polarizer

Entering Light

Figure 2-3: Light path through the elements of a DIC microscope. The path of a single ray of light is illustrated as it passes through a DIC microscope. The entering light ray passes through the polarizer and strikes the first Wollaston prism, which is called the compensator prism. This prism splits the single entering ray into two rays that pass through different parts of the condenser, specimen, and objective. These two rays are recombined into a single ray by the second Wollaston prism, which is called the slider prism. The ray then passes through a second polarizer, called the analyzer, and emerges from the microscope.
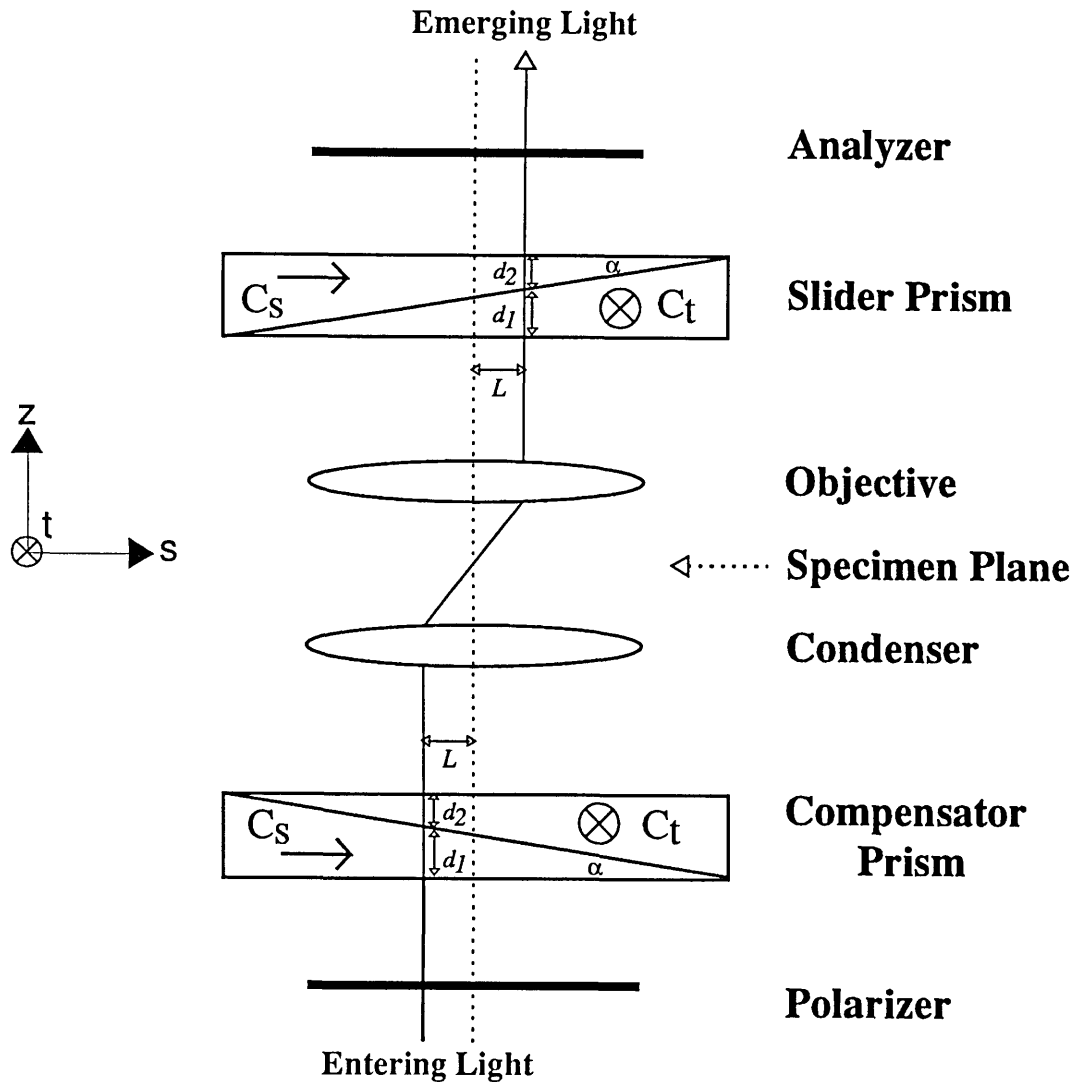
Figure 2-4: Phase compensation in a DIC microscope. This figure illustrates one light ray that is parallel to, but a distance L from the optical axis of the microscope. Its path through C_s in the slider prism is shorter than its path through C_t. However, the reverse is true in the compensator prism. Thus phase differences resulting from path length differences are canceled. For clarity, ray splitting (shown in Figure 2-3) is not illustrated in this figure.
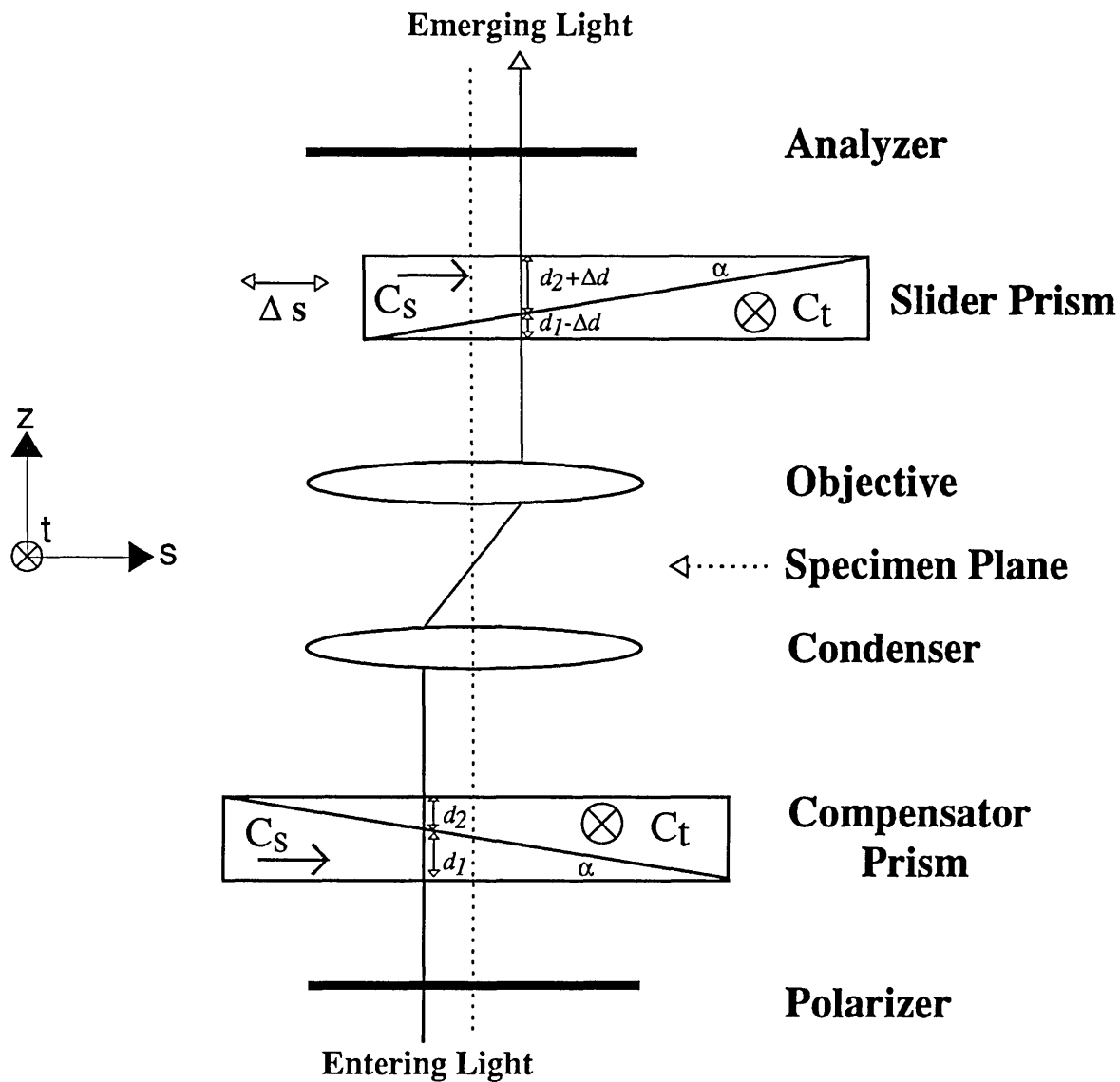
Emerging Light

Analyzer

C_s $\quad$ $d_2 + \Delta d$ $\quad$ α

Δs $\qquad$ $d_1 - \Delta d$ $\quad$ $\otimes$ C_t **Slider Prism**

z

t

$\otimes$ $\quad$ **s**

Objective

$\triangleleft$ ······ **Specimen Plane**

Condenser

C_s $\qquad$ d_2 $\qquad$ $\otimes$ C_t **Compensator**
$\qquad\qquad$ d_1 $\qquad$ α $\qquad\qquad$ **Prism**

Polarizer

Entering Light

Figure 2-5: Effect of translating the slider prism. This figure illustrates one light ray similar to the one shown in Figure 2-4. Translation Δs of the slider prism shortens the path through the C_s part of the slider prism by Δd and lengthens the path through the C_t part of this prism.

16

If the slider prism of a DIC microscope is translated in the s direction, spatial differences in phase delay are still canceled (Figure 2-5). However, a spatially uniform phase delay is introduced to all rays. In general, translations that increase the phase delay of rays whose electric field vectors are in the t direction decrease the phase delay of rays with electric field vectors in the s direction. A control on the microscope allows the user to translate the slider prism. The resulting difference in phase is called phase bias.

Because the slider prism is oriented opposite to the compensator prism, the two rays that exit the compensator prism are recombined by the slider prism as shown in Figure 2-3.

Interference

When light passes through a transparent specimen, its intensity is not attenuated. However, a phase delay is introduced due to the refractive index difference of the specimen and the surrounding media. Because light detectors (either camera or human eye) are only sensitive to light intensity, phase differences go undetected with ordinary light microscopes.

Interference methods are employed to convert phase delays to amplitude differences. The general concept of these methods is to allow two rays to pass through different parts of a specimen. After passing through the specimen, the rays have a relative phase difference proportional to the refractive index differences in the specimen. These phase shifted light rays are recombined so that the resultant intensity will depend on the phase difference. For instance, if they are 180° out of phase, the resultant intensity will be zero and the light is said to destructively interfere. If they are in phase they will interfere constructively for a maximum intensity. Phase differences between these values result in a range of intensities between the minimum and maximum.

In order for an interference method to work, the two interfering rays must be coherent. If they are incoherent, their phase differences are random and therefore cannot be used to indicate refractive index differences in the specimen. Sources of illumination used for light microscopes (e.g. halogen lamps, xenon arcs, etc.) produce light that is only weakly coherent. Such light can be understood as having components with electric field vectors in all directions (e.g. randomly polarized), with each component incoherent with all others.

Polarization is used in a DIC microscope to introduce the coherence necessary for an interference system. The first polarizer eliminates components of the entering light with electric fields oriented in all directions except one. If the orientation of a polarizer is set 45° relative to s, i.e. the y direction, then light emerging from the polarizer can be expressed as components in the s and t directions that are not only equal in magnitude but also coherent with each other.

The s and t components of the polarized light are refracted differently by the compensator Wollaston prism and pass through different parts of the specimen. The s and t components therefore accumulate different phase delays as they pass through different parts of the specimen. When the components are recombined by the slider prism, they are no longer in phase with each other. Instead of being equal at all instants of time, the s and t components are periodically bigger and smaller than each other. The original linearly polarized light is now elliptically polarized. The analyzer passes light with only one polarization and thereby converts phase differences between s and t components into amplitude modulation.

2.2.2 Light Through the DIC Microscope

We now describe the path and phase of light as it passes through each microscope element. We decompose the light ray into component A with electric field vector $\mathbf{E_A}$ in the t direction and component B with $\mathbf{E_B}$ in the s-z plane. The phase differences between components A and B along the light path are found and Table 2.1 summarizes the results.

Consider a light ray that is entering a DIC microscope parallel to the optical axis of the microscope, as shown schematically in Figure 2-4. Components A and B of the entering light are incoherent. Phase relations between $\mathbf{E_A}$ and $\mathbf{E_B}$ are random (Table 2.1 top line). The first optical element is the polarizer which is set so that the polarization direction of the emerging light is 45° with respect to the axes of both prism crystals, i.e. the y direction. After passing through the polarizer the electric field components $\mathbf{E_A}$ and $\mathbf{E_B}$ are coherent and equal in phase and magnitude;

$$\mathbf{E_A} = E_o\mathbf{t}, \tag{2.5}$$

$$\mathbf{E_B} = E_o\mathbf{s}, \tag{2.6}$$

and

$$E_o = |E_o|e^{-j\phi_o}, \tag{2.7}$$

and where $|E_o|$ and ϕ_o are constants. The random phase difference between $\mathbf{E_A}$ and $\mathbf{E_B}$ before polarization is changed to a zero phase difference (See Table 2.1).

Figure 2-4 shows the path of light through the compensator prism. The prism causes a nonuniform phase difference between components A and B because the prism is asymmetric. Specifically from Figure 2-4, we see that the ray travels a distance d_1 in C_s and d_2 in C_t. This means that the electric field components after passing through the compensator prism are

$$\mathbf{E_A} = E_o e^{j(k_\parallel d_2 + k_\perp d_1)}\mathbf{t}, \tag{2.8}$$

$$\mathbf{E_B} = E_o e^{j(k_\parallel d_1 + k_\perp d_2)}\mathbf{s}', \tag{2.9}$$

Optical Element	$\angle E_B - \angle E_A$
Illuminator	random phase variations
Polarizer	0
C_s	$d_1(k_{\parallel} - k_{\perp})$
C_t	$d_1(k_{\parallel} - k_{\perp}) + d_2(k_{\perp} - k_{\parallel})$
Condenser	$d_1(k_{\parallel} - k_{\perp}) + d_2(k_{\perp} - k_{\parallel})$
Specimen	$d_1(k_{\parallel} - k_{\perp}) + d_2(k_{\perp} - k_{\parallel}) +$ $\phi(\gamma_s, \gamma_t) - \phi(\gamma_s - s_o, \gamma_t)$
Objective	$d_1(k_{\parallel} - k_{\perp}) + d_2(k_{\perp} - k_{\parallel}) +$ $\phi(\gamma_s, \gamma_t) - \phi(\gamma_s - s_o, \gamma_t)$
C_t	$d_1(k_{\parallel} - k_{\perp}) + d_2(k_{\perp} - k_{\parallel}) +$ $\phi(\gamma_s, \gamma_t) - \phi(\gamma_s - s_o, \gamma_t) +$ $(d_1 - \Delta d)(k_{\perp} - k_{\parallel})$
C_s	$d_1(k_{\perp} - k_{\parallel}) + d_2(k_{\parallel} - k_{\perp}) +$ $d_1(k_{\parallel} - k_{\perp}) + d_2(k_{\perp} - k_{\parallel}) +$ $\phi(\gamma_s, \gamma_t) - \phi(\gamma_s - s_o, \gamma_t) +$ $+2\Delta d(k_{\parallel} - k_{\perp})$ $= \phi(\gamma_s, \gamma_t) - \phi(\gamma_s - s_o, \gamma_t)$ $+ 2\Delta d(k_{\parallel} - k_{\perp})$
Analyzer	$\phi(\gamma_s, \gamma_t) - \phi(\gamma_s - s_o, \gamma_t) +$ $2\Delta d(k_{\parallel} - k_{\perp})$

Table 2.1: This table tracks changes in the relative phase of $\mathbf{E_A}$ and $\mathbf{E_B}$ as light passes through the optical elements of the microscope. Note that $k_{\parallel} = \omega n_{\parallel}/c$, $k_{\perp} = \omega n_{\perp}/c$, and $\phi(\gamma_s, \gamma_t)$ is the phase associated with light traveling through the specimen as described by Equation 2.12.

19

where

$$k_{\parallel} = \frac{\omega n_{\parallel}}{c}, \tag{2.10}$$

$$k_{\perp} = \frac{\omega n_{\perp}}{c}, \tag{2.11}$$

s' is a unit vector in the s-z plane perpendicular to the propagation direction of the B component, ω is the radian frequency of the light, and c is the speed of light in a vacuum.

Because the refractive indices of components A and B are different in the prisms, the components refract differently and split. Figure 2-4 does not explicitly show the ray splitting by the compensator prism, because we assume this splitting is very small. Figure 2-3 shows this splitting effect by greatly exaggerating the angular difference between the rays as they emerge from the compensator prism. Typically the angular separation is 0.001 radians [16].

The condenser focuses light rays that are angularly separated onto points that are laterally separated along s in the specimen plane. This lateral separation, or shear, is typically on the order of 1 μm [16].

Consider the phase accumulated as the light passed through the specimen. We assume a thin transparent specimen with refractive index $n_s(\gamma_s, \gamma_t)$. Light traversal through the specimen results in a phase delay $\phi(\gamma_s, \gamma_t)$ given by

$$\phi(\gamma_s, \gamma_t) = \frac{n_s(\gamma_s, \gamma_t)\omega D}{c}, \tag{2.12}$$

where D is the specimen thickness. Using this phase delay term, we may now characterize the electric field of A and B just after passing through the specimen as[3]

$$\mathbf{E_A} = E_o e^{j\phi(\gamma_s, \gamma_t)} e^{-j(k_{\perp} d_1 + k_{\parallel} d_2)} \mathbf{t}, \tag{2.13}$$

and

$$\mathbf{E_B} = E_o e^{j\phi(\gamma_s - s_o, \gamma_t)} e^{-j(k_{\parallel} d_1 + k_{\perp} d_2)} \mathbf{s''}, \tag{2.14}$$

where s_o is the lateral displacement or shear of the rays in the specimen plane and s'' is a unit vector in the s-z plane perpendicular to the propagation direction of the B component. Note that the magnitude $|E_o|$ does not change since we have assumed that the specimen is transparent.

The rays then pass through the objective. We assume that the condenser and objective pair operate such that a ray, exiting the compensator prism a distance L

---

[3]In these equations and in subsequent equations we ignore phase terms that arise as the rays pass between optical elements. These phase terms are common to both the A and B components and therefore do not affect phase differences between the components. Later in this section, we show that only phase differences are important.

20

to the left of the microscope optical axis, passes through approximately the center of the specimen plane and enters the slider prism a distance L to the right of the optical axis as shown in Figure 2-4. That is, we illustrate the case of unity magnification in Figure 2-4. (Similar results hold for other magnifications with appropriate modifications of the prisms.) Because the two prisms are inverted, the ray travels a distance d_1 in C_t of the slider prism and d_2 in C_s of this prism. The slider prism introduces a phase delay to component A of $k_\perp d_2 + k_{\|} d_1$ and a phase delay of $k_\perp d_1 + k_{\|} d_2$ to component B. The total phase due to traveling through both prisms is the same for component A and B and is given by

$$\phi_{prism} = k_\perp(d_1 + d_2) + k_{\|}(d_1 + d_2). \tag{2.15}$$

This arrangement of the two prisms causes a phase compensation such that all rays emerging from the slider prism have the same phase in the absence of a specimen.

Translation of the slider prism (Figure 2-5) introduces additional phase terms. If the slider is translated by Δs, then the path through C_s is lengthened by Δd and the path through C_t is shortened by Δd where

$$\Delta d = \Delta s \tan \alpha. \tag{2.16}$$

The total phase introduced by the two prisms is $(d_1 + d_2 - \Delta d)k_{\|} + (d_1 + d_2 + \Delta d)k_\perp$ for the A component and $(d_1 + d_2 + \Delta d)k_{\|} + (d_1 + d_2 - \Delta d)k_\perp$ for the B component. These phases are no longer equal; they differ by a phase bias

$$\phi_b = 2\Delta d(k_{\|} - k_\perp). \tag{2.17}$$

As Table 2.1 indicates, the phase difference between $\mathbf{E_A}$ and $\mathbf{E_B}$ after the slider prism is due only to the specimen and ϕ_b.

The A and B components are recombined by the slider prism to form a single ray (Figure 2-3). The electric field vector of this ray can be written as

$$\mathbf{E} = \mathbf{E_B} + \mathbf{E_A} = E_o e^{j(\phi_s(\gamma_s, \gamma_t) + \phi_b)}\mathbf{s} + E_o \mathbf{t}, \tag{2.18}$$

where

$$\phi_s(\gamma_s, \gamma_t) = \phi(\gamma_s, \gamma_t) - \phi(\gamma_s - s_o, \gamma_t). \tag{2.19}$$

The next optical element is another polarizer called the analyzer. Let a_n represent the angle between the polarization direction $\mathbf{p}$ of the analyzer and $\mathbf{s}$. Then the electric field vector for light leaving the analyzer is

$$\mathbf{E} = \left(E_o e^{j(\phi_s(\gamma_s, \gamma_t) + \phi_b)} \cos a_n + E_o \sin a_n \right) \mathbf{p}. \tag{2.20}$$

The final component is a detector, either the human eye or a camera. Light detectors are sensitive to light intensity

$$i(\gamma_s, \gamma_t) = < \frac{1}{2}\mathbf{E}\mathbf{E}^* >, \tag{2.21}$$

where the angle brackets denote temporal averaging over a time that is long compared to the coherence time of the light and short compared to the characteristic response time for the detector. Substituting for $\mathbf{E}$,

$$
\begin{aligned}
i(\gamma_s, \gamma_t) &=< \tfrac{1}{2}(E_o e^{j(\phi_s(\gamma_s,\gamma_t)+\phi_b)} \cos a_n + E_o \sin a_n) \\
&\times (E_o^* e^{-j(\phi_s(\gamma_s,\gamma_t)+\phi_b)} \cos a_n + E_o^* \sin a_n) >,
\end{aligned}
\tag{2.22}
$$

which reduces to

$$
i(\gamma_s, \gamma_t) = i_o(1 + 2\cos(\phi_s(\gamma_s, \gamma_t) + \phi_b)\sin a_n \cos a_n),
\tag{2.23}
$$

where

$$
i_o = \frac{1}{2}|E_o|^2.
\tag{2.24}
$$

The first polarizer in the microscope made components A and B coherent. If components A and B were incoherent their phases would vary randomly and the term $\cos(\phi_s + \phi_b)$ would average to zero over time.

Typically the polarization directions of the polarizer and analyzer are orthogonal. For this crossed polarizer configuration, $a_n = 135°$,

$$
i_\perp(\gamma_x, \gamma_y) = i_o(1 - \cos(\phi_s(\gamma_x, \gamma_y) + \phi_b)),
\tag{2.25}
$$

or

$$
i_\perp(\gamma_x, \gamma_y) = 2i_o\left(\sin^2(\frac{\phi_s(\gamma_x, \gamma_y) + \phi_b}{2})\right).
\tag{2.26}
$$

This equation shows that a DIC microscope produces an image whose intensities are a nonlinear function of phase gradients introduced by the specimen.

Plate 2.1: Simulated DIC images of a thin transparent disk. The top panel illustrates the disk with a diameter of 19 μm. The bottom panel illustrates DIC images (calculated using Equation 2.26 with s_o equal to 2/3 μm) with three different positions of the slider prism: $\phi_b = 0$ (left), 90° (middle), and 180° (right). Each image is scaled so that the maximum intensity appears white and the minimum intensity appears dark.

2.3 Quantitative Interpretation of DIC Images

Quantitative interpretation of DIC images can be difficult for several reasons. One reason is that the mapping between object (specimen) and image is not unique. One can obtain several different images (by adjusting the slider prism) with the same object. Also the same image can be obtained with several different objects. Another difficulty in interpretation arises because the images often give a false three dimensional impression.

First we show that different images of the same object can be produced by varying the slider prism position. To illustrate this, we present two examples. In the first example, we simulate images from a thin transparent disk in the plane of the stage. Let r and D represent the radius and the thickness of the disk respectively. Let n_s represent the refractive index of the disk. For simplicity we let the refractive index of the disk's surroundings equal zero. The disk is represented by the phase

$$\phi(\gamma_x, \gamma_y) = \frac{\omega D}{c} n_s \tag{2.27}$$

if $\gamma_x{}^2 + \gamma_y{}^2 < r^2$ and zero otherwise.

Plate 2.1 and Figure 2-6 illustrate $\phi(\gamma_x, \gamma_y)$ and the simulated DIC images of this disk (effects of blurring have been ignored). Only the edges of the object can be seen in the DIC images. The appearance of the edges depends on their orientation with respect to the axis of shear and the positions of the slider.

As a second example we show images (not simulated) of a polystyrene microsphere taken at two different slider prism positions. Plate 2.2 illustrates these images. In the top image, one edge appears bright and the other appears dark as compared to the background. The other image of the same microsphere exhibits edges that are equally bright compared to the background. By changing the prism position, we have significantly changed the image. In fact, the two images of Plate 2.2 appear to represent structurally different objects.

We have illustrated how one object can produce several different images, and we now consider how a given image can represent several different objects. There are at least three different ways to alter the object without altering the image. First, the image intensity described by Equation 2.26 is a function of phase differences.
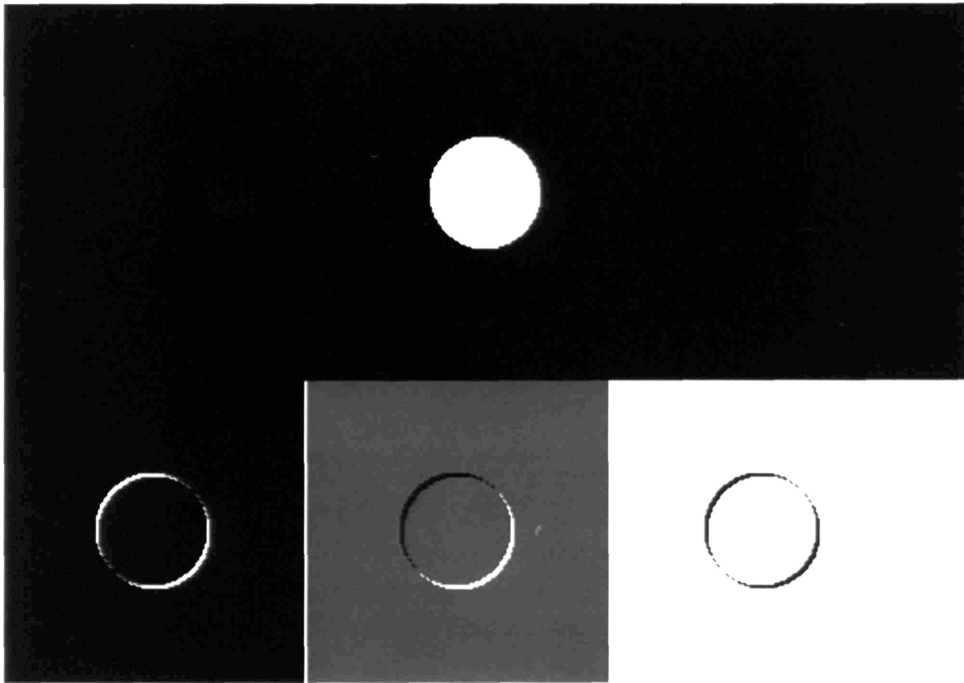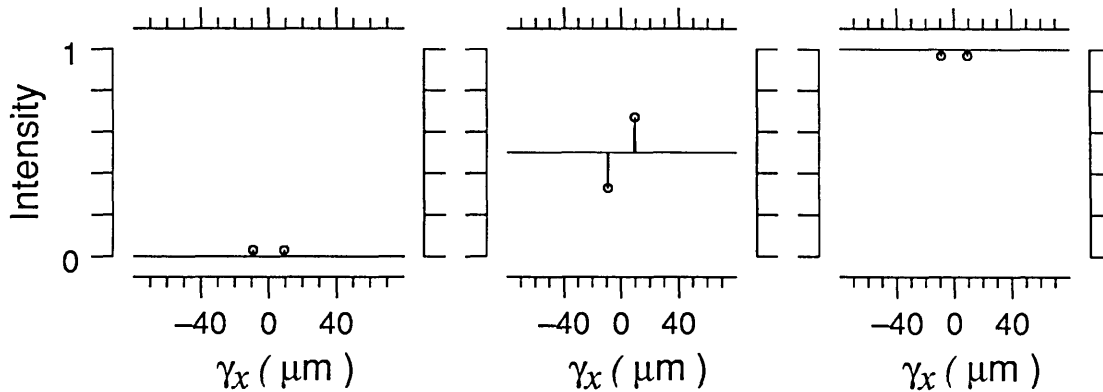
Plate 2.1

Figure 2-6: Simulated DIC images of a thin transparent disk. These plots illustrate change of intensity along a horizontal line through the center ($\gamma_y = 0$) shown in Plate 2.1. Each plot shows results for the same object (the thin transparent disk) but for a different value of ϕ_b: 0 (left), 90° (center), and 180° (right).

Plate 2.2: DIC images of a polystyrene microsphere taken at two different slider prism positions. The top image corresponds to $\phi_b = 0$ and the bottom image corresponds to ϕ_b closer to 90°.

This means that the disk images illustrated in Plate 2.1 remain the same if the refractive index of the disk and its surroundings are changed identically. Also the phase differences must be in the direction of shear. Therefore the image of an object whose refractive index gradients are exactly perpendicular to the shear direction is the same as the image of a region with no object. Finally, note that Equation 2.26 is periodic with a period of 2π. Thus the image of an object remains the same if the phase introduced by the object changes by an integer multiple of 2π.

Another important reason that DIC images are difficult to interpret is the presence of a shadow effect (lower middle panel of Plate 2.1). This shadow effect gives the viewer a false three dimensional impression. That is, the appearance of a shadow in the image gives a visual cue for interpreting the object's thickness. However, this shadow effect is not a function of object thickness. Instead, as Equation 2.26 indicates, it is a function of the shear distance, the object's refractive index, and the slider prism position.

Interpreting DIC images is not only difficult for humans, but also for machines. Consider the problem of reconstructing three dimensional shape from a series of DIC images. One simple approach is to find edges in each image, construct a three dimensional representation by stacking the contours, and then connect corresponding contours with surface elements. Although this scheme works for many kinds of images, DIC images pose a problem. Figure 2-7 shows that edges found in a DIC image may
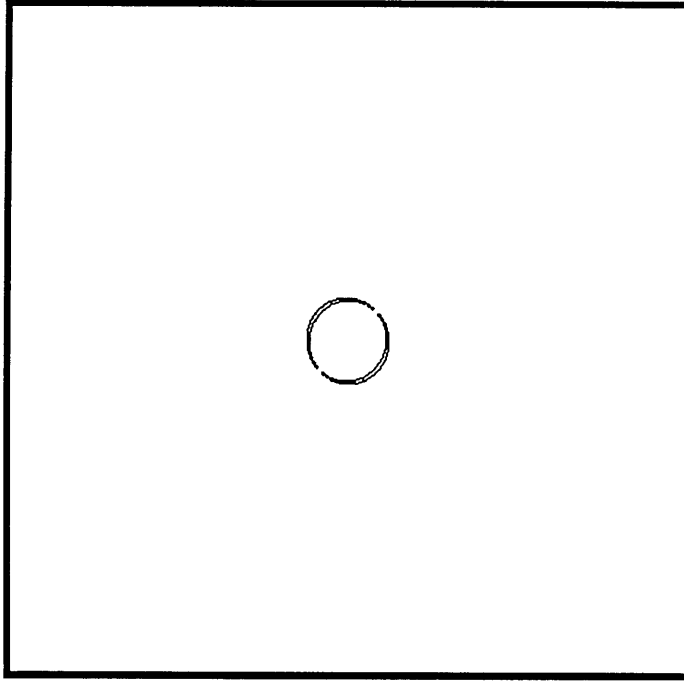
Plate 2.2

26
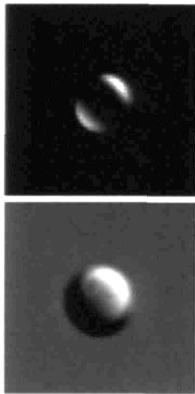
Figure 2-7: Edges in a DIC Image. The dark lines in this image are edges determined by a Laplacian-based edge detector (See [13]) for the simulated DIC images in Figure 2.1. This edge detector computes an estimate of $\nabla^2(\gamma_x, \gamma_y)$ and the zero crossings of this function are interpreted as edge points.

or may not correspond to edges of the object. Thus DIC images require additional processing.

2.4 Estimating Phase from DIC Images

The relation between phase and intensity is generally nonlinear (Figure 2-8). Furthermore the relation is not generally invertible; one cannot uniquely determine phase from intensity. However, if the range of phases never exceeds 180° (Figure 2-8, case 2), then the phase at every point is uniquely determined by the intensity at that point.

If the range exceeds 180°, the phase is not uniquely determined by the intensity. However, it may be possible to incorporate other information to recover phase. For example, if the spatial frequency content of the image is sufficiently limited, the phase correlation between nearby points can be used to "unwrap" that phase function. One can also incorporate information from multiple images. For example, one could record images of the same object with two different values of ϕ_b. If the two values differed by 90° one could uniquely determine phase for a 360° range (Figure 2-8, case 3).

2.5 DIC Point Spread Function

The index of refraction of many biological tissues (specifically the TM) differs little from that of water. For a sufficiently narrow range with $\phi_b = 90°$ (Figure 2-8, case 1), Equation 2.26 can be approximated by the first two terms of a Taylor series expansion. Then there is a linear relationship between $i(\gamma_x, \gamma_y)$ and $\phi_s(\gamma_x, \gamma_y)$ that is given by

$$i(\gamma_x, \gamma_y) = i_o \phi_s(\gamma_x, \gamma_y) + i_o. \tag{2.28}$$

Therefore, the DIC image is a linear transformation of phase and can be characterized by a linear transfer function. If we consider only intensity variations from i_o, Equation 2.28 can be written as

$$i(\gamma_x, \gamma_y) = i_o \phi_s(\gamma_x, \gamma_y) \tag{2.29}$$

or as a convolution,

$$i(\gamma_x, \gamma_y) = i_o \phi(\gamma_x, \gamma_y) * h_d(\gamma_x, \gamma_y), \tag{2.30}$$

where

$$h_d(\gamma_x, \gamma_y) = \delta(\gamma_x, \gamma_y) - \delta(\gamma_x - s_x, \gamma_y - s_y), \tag{2.31}$$

and s_x and s_y are the components of the shear along x and y respectively.

We can extend the thin specimen approximation by assuming that the total phase difference between the ray components passing through a thick specimen is primarily due to the phase difference at the focal plane. That is,

$$\begin{aligned} h_d(\gamma_x, \gamma_y, \gamma_z) &= \delta(\gamma_x, \gamma_y) - \delta(\gamma_x - s_x, \gamma_y - s_y) \quad \text{for } \gamma_z = 0, \\ &= 0 \quad\quad\quad\quad\quad\quad\quad\quad\quad\quad \text{otherwise.} \end{aligned} \tag{2.32}$$
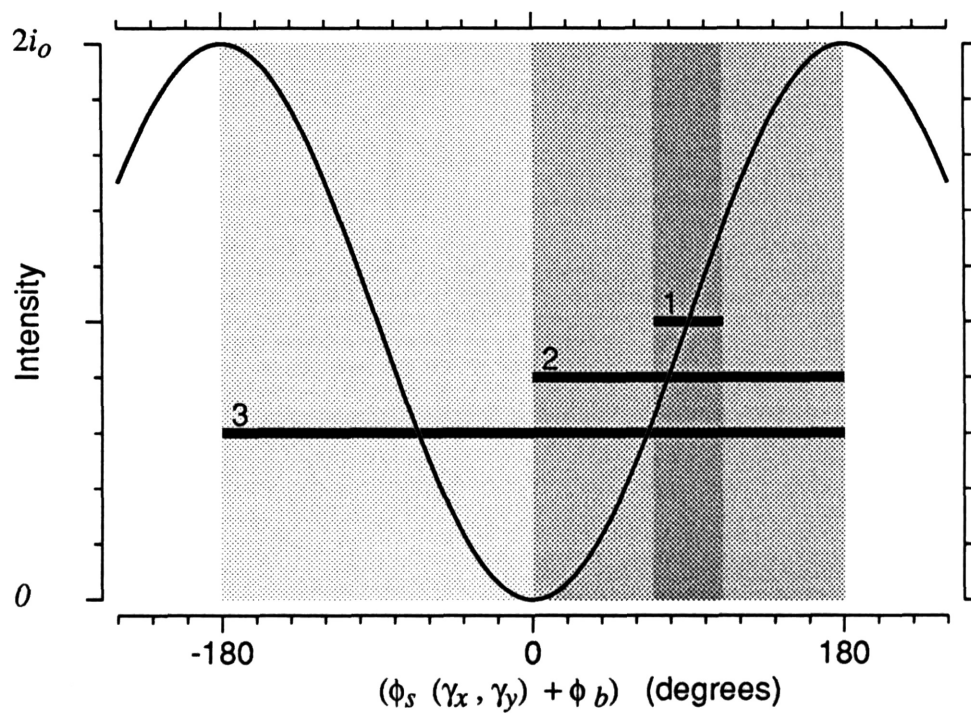
Figure 2-8: Dependence of intensity on phase. The curved line represents the relation between intensity $i(\gamma_x, \gamma_y)$ and the sum of $\phi_s(\gamma_x, \gamma_y)$ and ϕ_b (Equation 2.26). We consider three ranges of phase. Case 1: $\phi_b = 90°$ and $\phi_s(\gamma_x, \gamma_y) << i_o$; Case 2: $0 < \phi_s(\gamma_x, \gamma_y) + \phi_b < 180°$; Case 3: $-180° < \phi_s(\gamma_x, \gamma_y) + \phi_b < 180°$.

2.6 Microscope Model

Recall from Section 2.1 that blurring due to finite apertures in the microscope and camera optics can be characterized by the PSF $h_a(\gamma_x, \gamma_y, \gamma_z)$. Therefore, we can account for both the effects of finite aperture diffraction and DIC optics by combining $h_a(\gamma_x, \gamma_y, \gamma_z)$ and $h_d(\gamma_x, \gamma_y, \gamma_z)$. Equation 2.30 becomes

$$i(\gamma_x, \gamma_y, \gamma_z) = i_o \phi(\gamma_x, \gamma_y, \gamma_z) * h_d(\gamma_x, \gamma_y) * h_a(\gamma_x, \gamma_y, \gamma_z). \qquad (2.33)$$

The functions h_d and h_a can be combined into one point spread function,

$$i(\gamma_x, \gamma_y, \gamma_z) = i_o \phi(\gamma_x, \gamma_y, \gamma_z) * h_{ad}(\gamma_x, \gamma_y, \gamma_z). \qquad (2.34)$$

This leads to the important result that a DIC microscope can be characterized by a PSF which includes the effect of DIC differentiation as well as the finite aperture diffraction. Therefore a three dimensional deconvolution can recover $\phi(\gamma_x, \gamma_y)$ from $i(\gamma_x, \gamma_y, \gamma_z)$, which can then be used to estimate $n(\gamma_x, \gamma_y, \gamma_z)$ based on Equation 2.27.

Chapter 3

Measuring the Signal Processing Properties of a Microscope

In this chapter, we develop methods to characterize the signal processing properties of our microscope in terms of the model developed in Chapter 2. The measurement hardware includes a video camera and stepper motors that allow the microscope to be monitored and controlled from a personal computer. Both the point spread function of the microscope and the noise in the measurement system are empirically determined. The results are compared to theoretical predictions.

3.1 Methods

Figure 3-1 illustrates the main components of our measurement system: the microscope, video camera, stepper motor, and a personal computer equipped with a video digitizer (frame grabber). This measurement system is connected via a computer network to a graphics workstation (DecStation 5000, Digital Equipment Corp.), where all digital signal processing is implemented.

3.1.1 Sampling the Intensity Distribution

We wish to measure the output light intensity of the microscope, $i(\gamma_x, \gamma_y, \gamma_z)$. This intensity occupies a volume of continuous space and the measurement requires sampling this volume. In the x-y plane the intensity is sampled by the camera and video digitizer. We refer to the intensity samples in a single plane as an image. For our system, the spacing between the discrete intensity values in x and y is
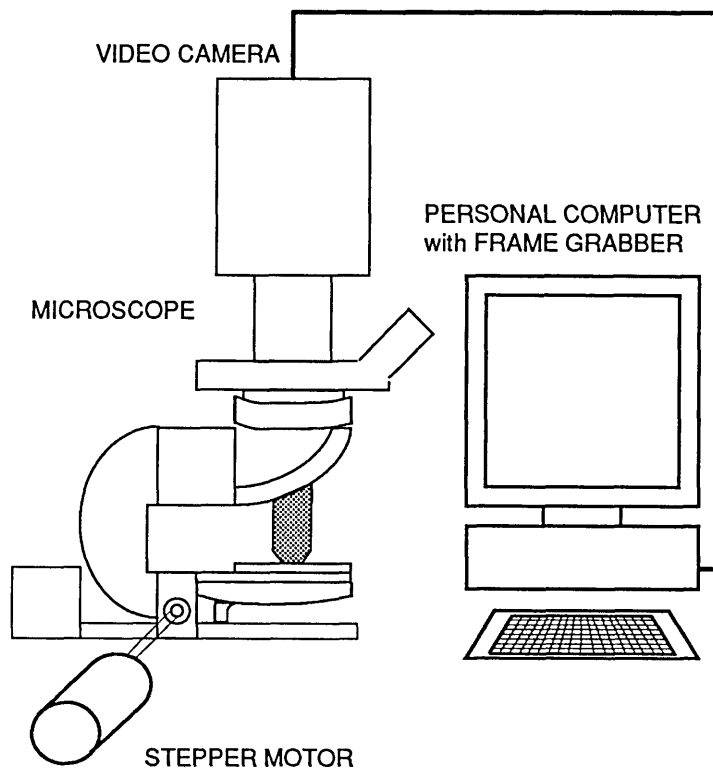
$$T_x = T_y \approx 0.33 \mu\text{m}. \tag{3.1}$$

Figure 3-1: The measurement system. The microscope is a Zeiss Standard WL with a 40X, 1.6mm working distance, 0.75 NA (numerical aperture), water immersion objective. The microscope is equipped with Nomarski DIC optics, a 2X optivar and a 0.7X optical coupler (Diagnostics Instruments). A Hamamatsu Newvicon (2400) video camera is coupled to the microscope. The output of the camera is converted to a numerical format by an 8 bit video digitizer (Data Translation DT2862) and recorded on a personal computer (IBM PC/AT clone). The computer controls the fine focus of the microscope via a stepper motor (Sigma Series 17). One step of the motor translates the stage of the microscope by 1/4 μm along the optical axis.

32

In order to record the three dimensional intensity we must not only sample in the x-y plane but also along z. To sample along z, images are recorded at discrete focal positions along the optical axis. The position along the optical axis is controlled by a stepper motor attached to the fine focus knob and driven by the PC. The spacing of these positions along z is

$$T_z \approx 1\mu\text{m}. \tag{3.2}$$

Each sample is referred to as a voxel (volume element).

3.1.2   Representation of Intensity

Intensities are converted to a sequence of integers by the camera and video digitizer. We represent this transformation by

$$i_m[g_x, g_y, g_z] = Q[ai(g_x T_x, g_y T_y, g_z T_z) + b] \tag{3.3}$$

where $i(g_x T_x, g_y T_y, g_z T_z)$ is the intensity of the light at a particular point in the image, g_x, g_y, g_z are integer indices, and $i_m[g_x, g_y, g_z]$ is an integer. The function $Q[\cdot]$ maps its argument to the nearest integer value between 0 and 255. The scaling constants a and b are determined by the camera, the analog-to-digital converter, and by uncalibrated offset and gain knobs on the video amplifier.

We assume the output light intensity of a microscope is related to the phase introduced by the specimen through a linear system (see Section 2.6) described by

$$i(\gamma_x, \gamma_y, \gamma_z) = k_1 \phi(\gamma_x, \gamma_y, \gamma_z) * h(\gamma_x, \gamma_y, \gamma_z) + k_2 \tag{3.4}$$

where k_1 and k_2 are constants. Combining Equation 3.4 and 3.3,

$$i_m[g_x, g_y, g_z] = Q[c\phi(g_x T_x, g_y T_y, g_z T_z) * h(g_x T_x, g_y T_y, g_z T_z) + d], \tag{3.5}$$

where

$$c = ak_1, \tag{3.6}$$

and

$$d = ak_2 + b. \tag{3.7}$$

Therefore the measured intensity is a quantized linear function of phase.

3.1.3   Slider Wollaston Prism Position

For precise control of the slider prism position, we have attached a stepper motor to the adjustment screw of the prism. Four hundred steps of the stepper motor turns the adjustment screw through one turn. The full range of possible prism positions corresponds to 3500 steps. To calibrate slider prism position in terms of ϕ_b, we

measured the intensity for the entire range of possible prism positions. In the absence of a specimen the expected relation (See Section 2.2.2 between ϕ_b and intensity is

$$i_\perp(\gamma_x, \gamma_y) \propto (1 - \cos \phi_b). \tag{3.8}$$

The measured intensity as a function of slider prism adjustment screw turns for the entire range of possible prism positions is shown in Figure 3-2. Notice that the range is less than one period. If we could sweep through an entire period of ϕ_b by turning the adjustment screw, then we could easily calibrate the relation between ϕ_b and slider prism position. The zero point for ϕ_b would correspond to the slider position with minimum output intensity and each turn of the slider away from the zero point would correspond to $\phi_b = 2\pi$ radians divided by the number of turns in a period.

Given sufficiently accurate measurements over a smaller range, we can still estimate the relation using a fitting procedure. The errors in the fit will be large if the range is small. Although the data shown in Figure 3-2 does not cover a complete period of the function in Equation 3.8, additional information for a fit can be obtained by adjusting the polarizers so that they are parallel. The expected intensity with parallel polarizers is

$$i_\parallel(\gamma_x, \gamma_y) \propto (1 + \cos \phi_b). \tag{3.9}$$

Our fitting procedure minimizes the mean square error obtained for both crossed and parallel polarizers. With the polarizers crossed, we measure intensity i_m as a function of stepper motor position τ and compute the mean squared error $e_\perp^2$ from the expected relation given in Equation 3.8,

$$e_\perp^2 = \frac{1}{M} \sum_\tau \sum_{g_x} \sum_{g_y} (i_m[g_x, g_y] - p_1(1 - \cos(p_2\tau + p_3)) + p_4)^2. \tag{3.10}$$

We also measure intensities with parallel polarizers and compute

$$e_\parallel^2 = \frac{1}{M} \sum_\tau \sum_{g_x} \sum_{g_y} (i_m[g_x, g_y] - p_1(1 + \cos(p_2\tau + p_3)) + p_4)^2. \tag{3.11}$$

We use an interactive method to find the values of p_1, p_2, p_3, and p_4 that minimize the sum of $e_\perp^2$ and $e_\parallel^2$. Data from both crossed and parallel polarizers are shown in Figure 3-3. Results from the fitting procedure are shown in Figure 3-4. The parameters p_2 and p_3 are fixed for a given microscope; they relate τ to ϕ_b. The parameters p_1 and p_4 depend on the illumination and the camera gain and offset.

The full range of slider prism positions corresponds to 8.75 turns of the adjustment screw (3500 motor steps). We can use p_2 and p_3 to convert this range to a range of ϕ_b,

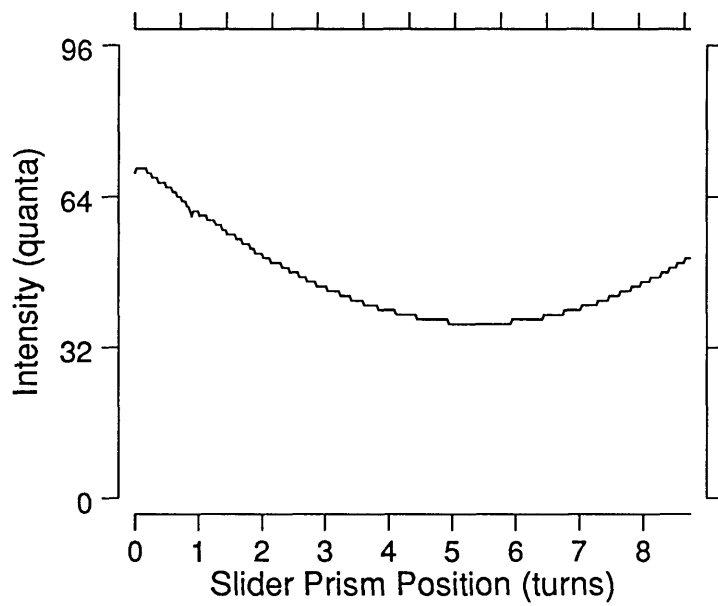$$-60° < \phi_b < 41°. \tag{3.12}$$

34

Figure 3-2: Effect of slider prism position on intensity. The microscope was set up to image an apparently empty volume in the specimen. Polarizers were crossed. Intensities were measured as a function of slider prism position and averaged over a 100 × 100 region. The stepper motor was advanced 10 steps between measurements, giving a resolution of 40 measurements per turn.
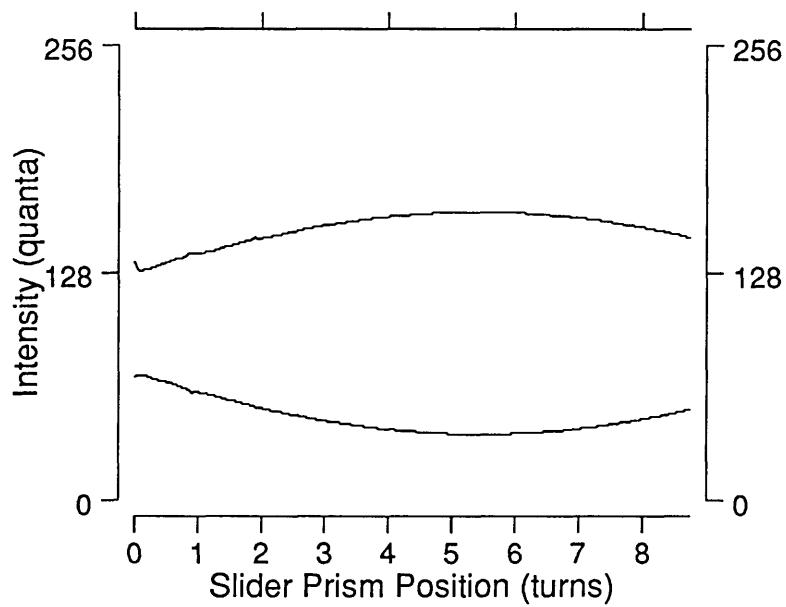
Figure 3-3: Interaction of slider prism and polarizer. The bottom curve shows the effect of slider prism position on intensity when the polarizers are crossed (same data as Figure 3-2). The top curve shows similarly measured data for parallel polarizers.
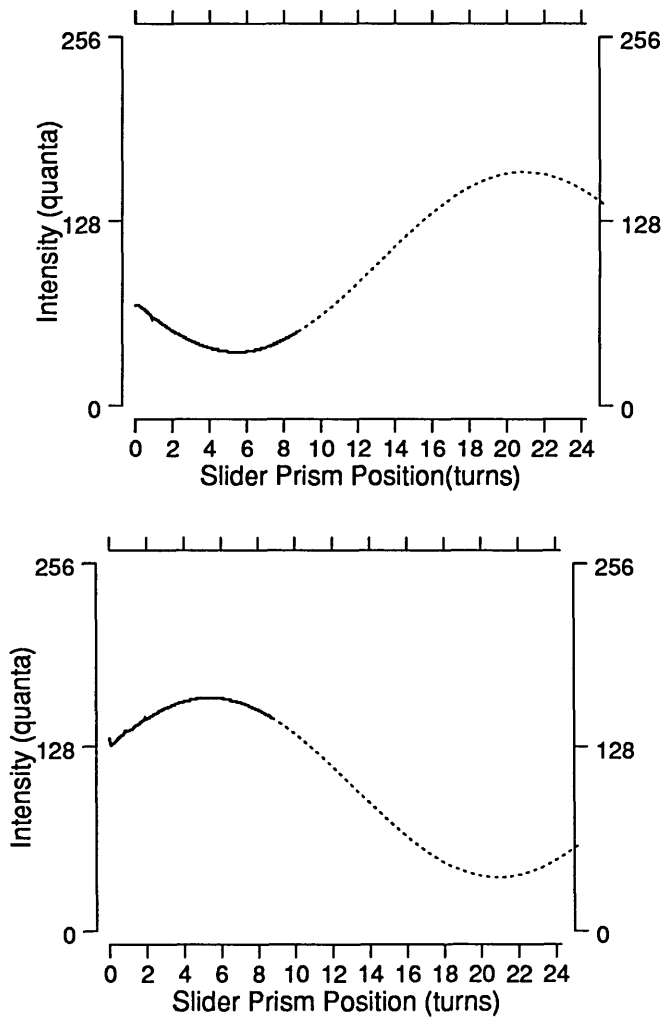
Figure 3-4: The measured and fitted data. The solid bold line shows the measured intensity points as a function of turns of the slider prism adjustment screw. The dashed lines show the results of the least mean square fit. The top panel illustrates the data from crossed polarizers and the relation of Equation 3.8. The bottom panel shows the data from parallel polarizers and the relation of Equation 3.9. The mean square error was 0.2 for the fitted parameters $p_1 = 62.31$, $p_2 = 0.000507$, $p_3 = -1.10$, and $p_4 = 36.98$.

This means that we cannot achieve the operating position of $\phi_b = 90°$. The operating point with the largest dynamic range in the linear region (See Section 2.5) is $\phi_b = 120°$.

To determine if it was important to measure intensities in both the crossed and parallel configurations, we repeated the fitting procedure using just the crossed configuration data. We obtained a good fit (i.e. small $e_\perp^2$), but the answer was wrong. Specifically, if $p_2 = 0.0034$, $p_3 = 2.38$, $p_1 = 35.71$ and $p_4 = 36.98$, then $e_\perp^2$ is equal to 0.15. However, $e_\parallel^2$ is equal to 1168. Therefore, using both the crossed and parallel data in the fitting procedure was crucial.

3.1.4 Object Preparation

Objects to be imaged by the microscope were constructed by embedding microscopic polystyrene microspheres (Polysciences). In early trials we used a gelatin embedding procedure. Two types of gelatin were used, food grade (Knox, unflavored) and research grade (Electron Microscopy Sciences) with a total bacteria count of 1000/gram. Three grams of gelatin were mixed with 90 mL H_2O and heated until the gelatin dissolved. The microspheres were dispersed in water (2.5% by weight) by the vendor. Three μL of this dispersion were mixed with the gelatin/H_2O and the mixture was cooled to room temperature. One hundred μL of 10% gluteraldehyde was added. A drop of the resulting mixture was placed on a glass slide with a coverslip. The slide was refrigerated overnight to set.

A commercially available product was used in later trials. This product is a water soluble mounting medium called Mount Quick (Electron Microscopy Sciences). Three μL of the microsphere dispersion was evaporated on a glass slide. The evaporated microspheres were mixed with Mount Quick, covered with a coverslip and allowed to set.

The two embedding methods gave similar results, but the latter method is preferable for two reasons. First, the method is easier. Second, bacteria were noticeable in the gelatin slides after storage for several weeks, even though they were stored at 4° C.

Slides were prepared using microspheres with four different diameters (0.24, 2.0, 2.8, 4.6 μm)[1]. Regions within a slide that contain no microspheres were used in some tests. Such a region is referred to as an apparently empty volume.

3.2 Measurements of Noise

To characterize noise in our measurement system, we recorded 100 images of an apparently empty volume. Two types of degradations are clear from the results.

---

[1]Microspheres with diameters of 0.15 μm were also embedded; however, they were barely visible in our microscope.

First, repeated measurements differ from each other. These differences suggest the presence of additive noise. Second, systematic patterns were apparent in the image that resulted when 100 images of an apparently empty volume were averaged. These patterns in the mean suggest the presence of stationary background degradations.

3.2.1 Noise Variance

Additive noise can result from many sources. Examples include shot noise that is implicit in the quantum nature of light and thermal noise that is introduced in the camera and video amplifiers. We estimated statistical properties of additive noise in our system by repeating measurements of an apparently empty volume 100 times. The volume contained $21 \times 21 \times 21$ voxels. We computed the temporal variance $\sigma_t^2[g_x, g_y, g_z]$ for each voxel. The average value of $\sigma_t^2[g_x, g_y, g_z]$ over the voxels was 22, corresponding to a temporal standard deviation of 4.7 which we use as an estimate of the standard deviation σ_n of the additive noise process. Variations in $\sigma_t[g_x, g_y, g_z]$ with g_x, g_y, and g_z were small. The standard deviation of $\sigma_t[g_x, g_y, g_z]$ across the volume was 0.3. We can interpret $\sigma_t[g_x, g_y, g_z]$ in terms of the dynamic range of the measured intensities. Since this range is 0-255, the noise standard deviation is 1.85% of the dynamic range for this particular configuration of illumination, camera gain, and camera offset.

3.2.2 Noise Correlation

Measuring noise correlation is important because it gives us information about the noise characteristics in our system. This information affects the signal processing methods used to reduce noise. We expect that there is negligible correlation between noise samples in time and along z. We therefore concentrate on the spatial correlations along x and y. Noise correlations can be quantified in terms of the autocorrelation function

$$R[g_x, g_y] = E\left(n_m[k_x, k_y] n_m[k_x - g_x, k_y - g_y]\right) \quad \text{for all } (k_x, k_y), \tag{3.13}$$

where $n_m[k_x, k_y]$ is the measured noise in a focal plane. The Fourier transform of $R[g_x, g_y]$ is the power spectrum $P_n[w_x, w_y]$. We can estimate $P_n[w_x, w_y]$ from the measured noise and compute an estimate of $R[g_x, g_y]$. The noise was measured by sampling the focal plane intensity from an apparently empty volume. This measurement was repeated 100 times and averaged. The difference of the averaged measurement and the unaveraged measurement is the noise measurement (without the mean). To estimate the noise power spectrum from this noise measurement we used periodogram averaging (See [13]). This method requires subdividing the image into smaller segments and averaging the periodograms from these segments. Periodogram averaging reduces the variance of the estimate by the number of segments averaged.

39

Intensity measurements for 96×96 samples were subdivided into nine 32×32 segments. For each segment, the periodogram estimate $\hat{p_N}[w_x, w_y]$ of the noise power was computed as follows:

$$\hat{p_N}[w_x, w_y] = |N[w_x, w_y]|^2/1024, \qquad (3.14)$$

where $N[w_x, w_y]$ is the discrete Fourier transform of the noise segment, and 1024 is the number of samples in each segment. The resulting periodogram estimates for each segment were averaged together to obtain the estimated noise power spectrum $\hat{P_N}[w_x, w_y]$. By taking the inverse discrete Fourier transform of $\hat{P_N}[w_x, w_y]$ we obtained an estimate for the noise autocorrelation $\hat{R}[g_x, g_y]$. The estimate is shown in Figure 3-5. If the noise is white, its discrete correlation function is given by

$$R[g_x, g_y] = \sigma_n^2 \delta[g_x, g_y], \qquad (3.15)$$

where σ_n^2 is the constant noise power, and $\delta[g_x, g_y]$ is the unit sample defined as

$$\delta[g_x, g_y] = \begin{cases} 1 & \text{if } g_x = g_y = 0, \\ 0 & \text{otherwise.} \end{cases}$$

Notice that the estimated autocorrelation in Figure 3-5 deviates most significantly from the unit sample along x. Specifically, the autocorrelation value 2/3 μm away from the origin (2 discrete samples) along x is 10% of the peak value. However along y the value 2/3 μm from the origin is 2.4% of the peak value. Since the video signal is generated by a scanning electron beam along x, we expect that there may be some correlation between samples that are adjacent along x. This is the reason that the correlation looks least like a unit sample along x. Yet because the peak value is located at the origin and is significantly larger than all the other values, this function is similar to a scaled unit sample. Therefore, to simplify analysis, we approximate the system noise as white noise.

The peak value in the autocorrelation is also an estimate of the noise power σ_n^2. For our measurement, the peak was 21, corresponding to an estimate of σ_n equal to 4.58. This compares well with our previous estimate of 4.7, obtained by computing the average temporal variance of voxels.

3.2.3   Noise Mean

Effects of averaging repeated measurements of intensity are illustrated in Plate 3.1, Plate 3.2, and Figure 3-6. Let $\beta_m[g_x, g_y, g_z]$ denote the average of M intensities measured for each voxel in an apparently empty volume. Row A illustrates $\beta_m[g_x, g_y, g_z]$ for $M = 1$ and Row B illustrates $\beta_m[g_x, g_y, g_z]$ for $M = 100$. Row A of Plate 3.1 shows
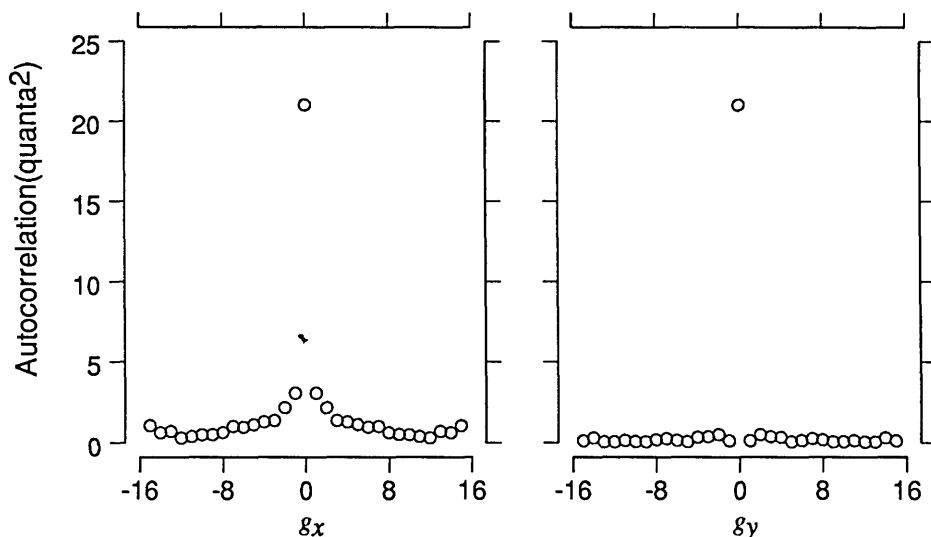
40

Figure 3-5: Noise autocorrelation estimate $\hat{R}[g_x, g_y]$ obtained from taking the inverse discrete Fourier transform of $\hat{P}_N[w_x, w_y]$, the noise power spectrum estimate. The left plot shows $\hat{R}[g_x, 0]$ and the right shows $\hat{R}[0, g_y]$. The autocorrelation estimate is 32×32 samples and the sample spacing in both x and y is $1/3$ μm.

apparently random intensities. Row B is similar; the effects of averaging are not obvious. Row A of Plate 3.2 also shows random intensities, but there is a suggestion of correlations along z. Row B of this plate shows much smaller random variations and striking lines along z. We quantify spatial variation in these results by computing the spatial standard deviation σ_v of $\beta_m[g_x, g_y, g_z]$. For $M = 1$, $\sigma_v = 8.11$; and for the $M = 100$, $\sigma_v = 6.67$. If the measurements resulted from a zero-mean additive white noise process, then averaging $M = 100$ measurements would have reduced σ_v by a factor of 10. Our results show considerably smaller reduction, leading to the conclusion that the process is not zero-mean.

Single Focus Background Subtraction

Patterns remain in our measured images even after averaging. Although measured in an apparently empty volume, these patterns will degrade all measurements. Therefore, we develop a method for estimate these patterns so that they can be removed from measurements. Measurements of $\beta_m[g_x, g_y, g_z]$ allow us to isolate these patterns and test background estimation schemes.

Background patterns arise from many sources. Camera imperfections, such as dust on the face of the camera, cause patterns that are invariant in z. An example of

Plate 3.1: Measurements $\beta_m[g_x, g_y, g_z]$ of intensity in an apparently empty volume: images parallel to the plane of the microscope stage. Intensities were measured for $21 \times 21 \times 21$ voxels, with sampling periods in x, y, and z of 1/3, 1/3, and 1 μm respectively. The rows in this figure illustrate noise reduction methods. Each row shows 5 x-y images, at $g_z = -10$ (left), -6, -2, 2, 6 (right). In each image, g_x and g_y vary from -9 to 9. For the purposes of illustration each x-y image (and subsequent images) was enlarged in x and y using bilinear interpolation (see [13]). Intensities are scaled so that largest value in each row appears as white and the smallest value appears as black. This emphasizes patterns within the row. To aid in comparisons between rows, we provide the mid value ((maximum + minimum)/2) and the range (maximum − minimum) of the data. A: No averaging (mid, range = 166, 60). For each value of g_z, a single frame from the video camera is shown. B: Averaging 100 repeated measurements (mid, range = 162.2, 45). For each value of g_z, 100 successive frames of data were collected and the average is shown. C: Single focus background subtraction (mid, range = -1.5, 49). For each value of g_z, a single frame from the video camera was recorded. The frame at $g_z = -10$ was taken as the background frame, and subtracted from all the images. D: Averaging and single focus background subtraction (mid, range = -2.4, 7.99). For each value of g_z, 100 successive frames of data were collected and the average was stored. The averaged image at $g_z = -10$ was taken as the background frame, and subtracted from all the averaged images. E: Linear background subtraction, averaging, and single focus background subtraction (mid, range = 0, 5.4). For each value of g_z, 100 successive frames of data were collected and the average was stored. For each g_x and g_y, a line was fit through the averaged intensities along g_z. The collection of these lines comprised the background volume, which was subtracted from the averaged volume.

Plate 3.2: Measurements $\beta_m[g_x, g_y, g_z]$ of intensity in an apparently empty volume: images in planes perpendicular to the microscope stage. This plate illustrates the same data shown in Plate 3.1 but from a different view. The images are perpendicular to the x axis and illustrate planes in z-y. We refer to this as the z-y view. Each row shows 5 z-y images, at $g_x = -10$ (left), -6, -2, 2, 6 (right). In each image, g_y and g_z vary from -9 to 9.

42

$g_Z = -10$ $g_Z = -6$ $g_Z = -2$ $g_Z = 2$ $g_Z = 6$
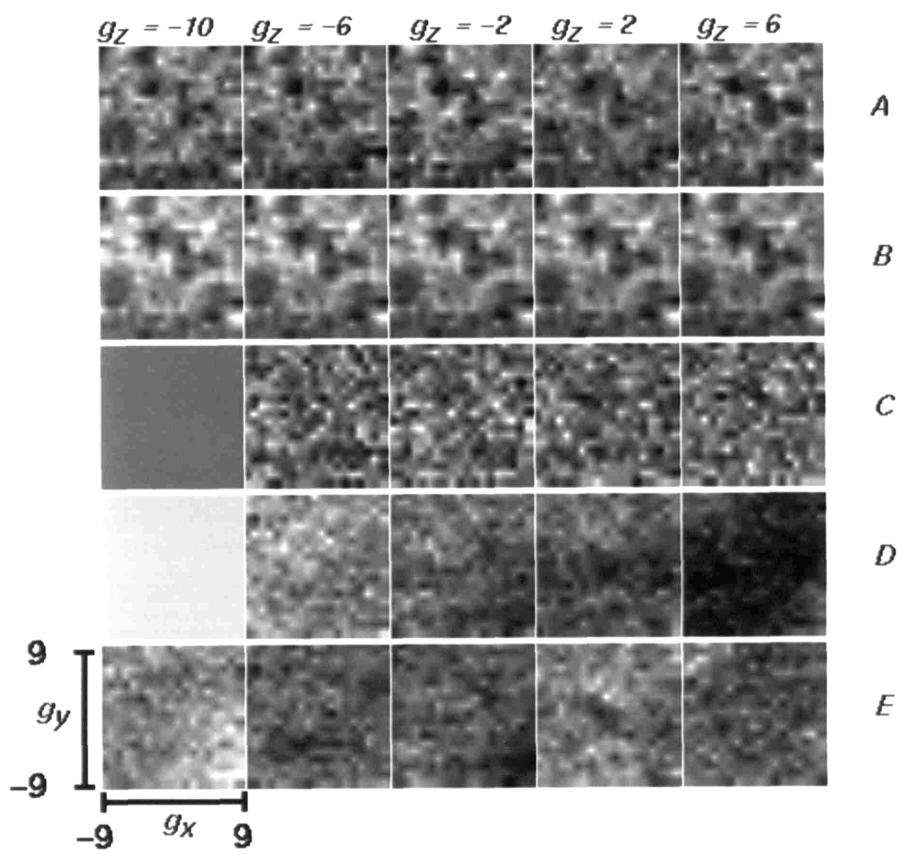
A

B

C

D

9
g_y
−9

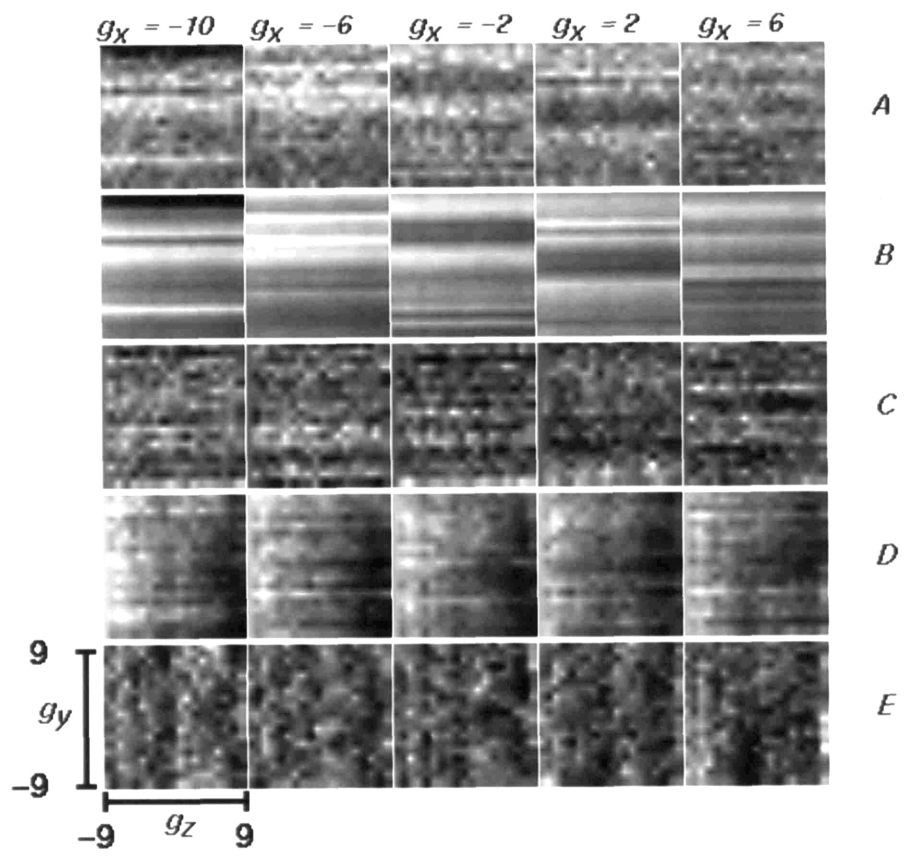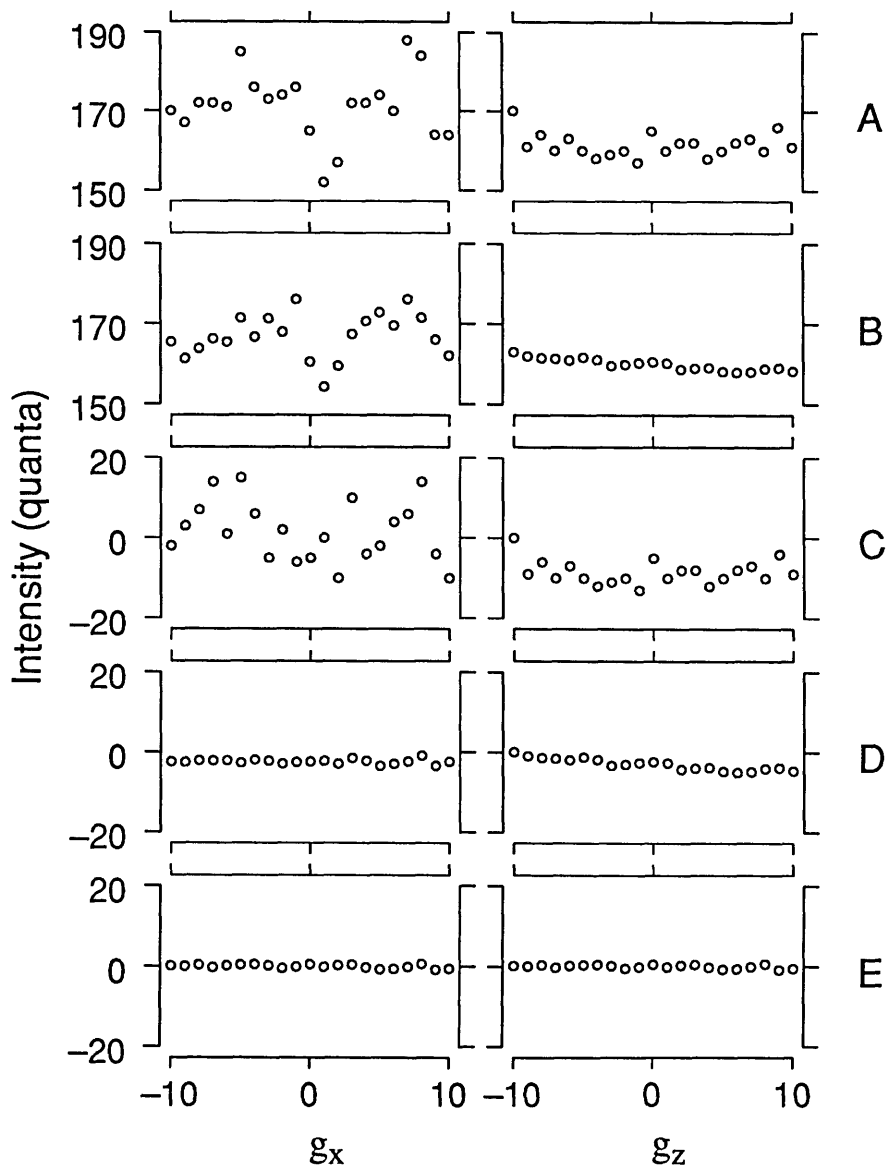−9 g_x 9

E

Plate 3.1

43

Plate 3.2

44

Figure 3-6: Measurements $\beta_m[g_x, g_y, g_z]$ of intensity in an apparently empty volume: plots of intensity. The left panels show variations in intensity along x for $g_y = g_z = 0$. The right panels show variations in intensity along z for $g_x = g_y = 0$. These plots illustrate the same data shown in Plates 3.1 and 3.2.

this type of pattern is the black stripe seen in the top of the leftmost image in Row A of Plate 3.2. Such patterns are easily removed. In practice, one moves the focus of the microscope so that all structures in the specimen are so blurred that they are no longer visible. The resulting image still contains patterns that remain constant across z. This image is called a background image and is subtracted from all other images. We refer to this method as "single focus background subtraction".

Single focus background subtraction is illustrated in Row C of Plate 3.1, Plate 3.2, and Figure 3-6. Notice that the black stripe on the top of the leftmost image in Row A of Plate 3.2 has been removed. The spatial standard deviation σ_v of the resulting volume is 6.64.

The combination of single focus background subtraction and averaging can be seen in Row D of Plate 3.1, Plate 3.2, and Figure 3-6. The spatial standard deviation σ_v for this volume is 1.43. Therefore, this combined processing significantly decreased the overall intensity variations in our measurements. However this spatial standard deviation is still much greater than would be expected if the degradations were produced by zero-mean additive white noise. Because temporal variabilities suggest that σ_n is on the order of 4.7 (see Section 3.2.1), averaging 100 measurements would result in a spatial standard deviation of 0.47.

Background Estimation

Single focus background subtraction cannot remove all background patterns. For example, dust on any optical element that moves when the focus is changed will cause patterns that change with focus.

The most apparent pattern after single focus background subtraction with averaging (Row D in Plates 3.1 and 3.2) is a systematic intensity variation in z. This light variation may be due to the configuration of our microscope that causes the condenser to move as we move the stage to change focus. This movement causes a departure from the correct Koehler illumination configuration [10]. These trends are illustrated in Figure 3-7. These trends introduce systematic low-frequency degradations into all our measurements.

Compare the x-y views (Plate 3.1) and z-y views (Plate 3.2) for the measurements in Row D. The variations with z appear systematic and generally linear, and the variations in the x-y plane appear neither systematic nor linear. These observations suggest a background estimation scheme in which intensity variations in z are represented by linear fits for each g_x-g_y pair. We refer to subtracting this estimated background as "linear background subtraction." Results of this processing scheme are shown in Row E of Plate 3.1, Plate 3.2, and Figure 3-6. The spatial standard deviation σ_v that remains after this processing is equal to 0.66. This value of σ_v is now closer to 0.47, the value we expect to be left after averaging.
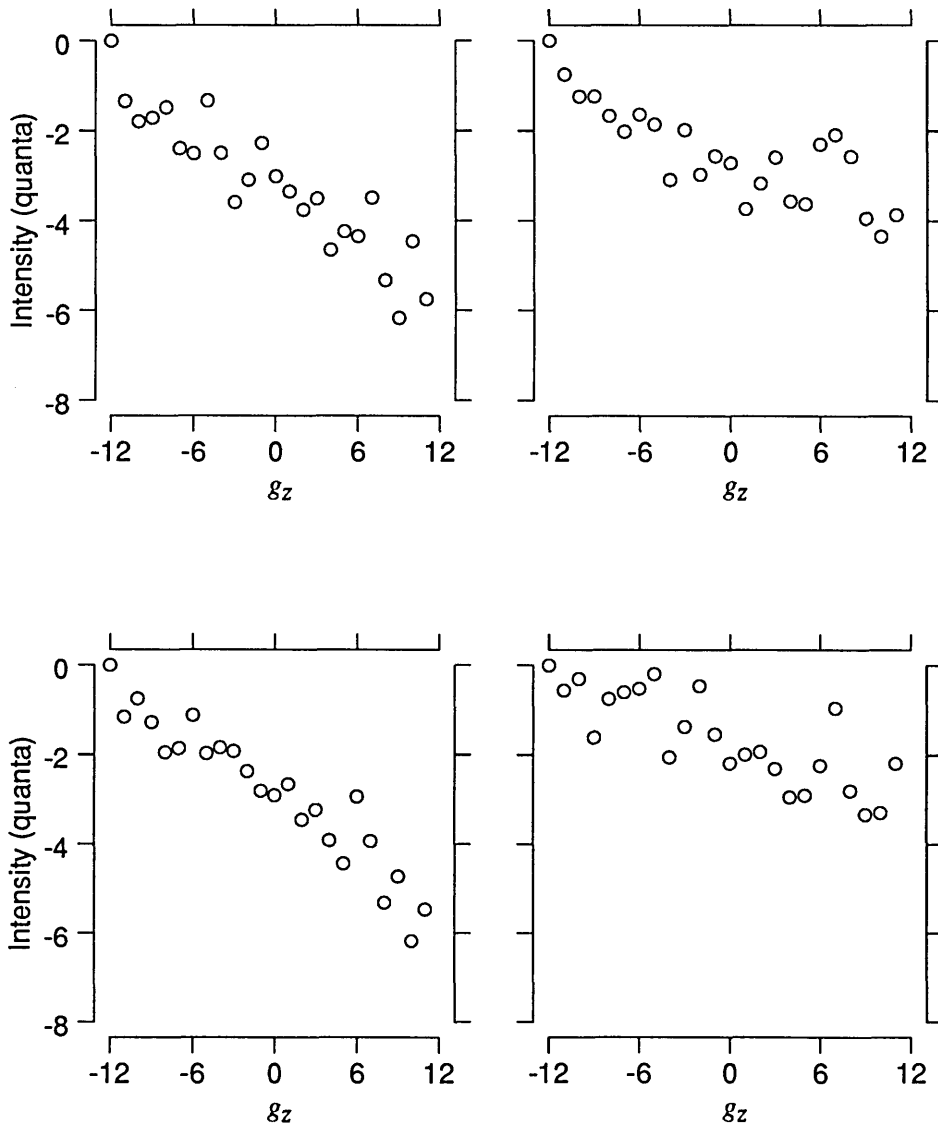
Figure 3-7: Measured background intensity $\beta_m[g_x, g_y, g_z]$ after averaging and single focus background subtraction. The figure illustrates intensities along z for 4 different g_x-g_y pairs (i.e. intensities along horizontal lines in Row D of Plate 3.2).

Plate 3.3: Measurements $h_m[g_x, g_y, g_z]$ of the PSF: images parallel to the plane of the microscope stage. Intensities were measured for $51 \times 51 \times 24$ voxels, with sampling periods in x, y, and z of 1/3, 1/3, and 1 μm respectively. The rows in this plate illustrate noise reduction methods. Each row shows 5 x-y images, at $g_z = -2$ (left), -1, 0, 1, 2 (right). In each image, g_x and g_y vary from -9 to 9. A: No averaging. B: Averaging 100 repeated measurements. C: Single focus background subtraction (background frame is at $g_z = -12$). D: Averaging and single focus background subtraction. E: Linear background subtraction, averaging, and single focus background subtraction.

Plate 3.4: Measurements $h_m[g_x, g_y, g_z]$ of the PSF: z-y views. This plate illustrates z-y views of the data shown in Plate 3.3.

3.3 Point Spread Function Measurement

To characterize the relation between object and measured image, we measure the microscope's point spread function (PSF). By definition, a PSF is the three dimensional intensity pattern that results from a point source. We approximate the point source by a polystyrene microsphere with diameter 0.24 μm. We refer to the resulting intensity pattern as $h_m[g_x, g_y, g_z]$. Measurements of $h_m[g_x, g_y, g_z]$ are shown in Row A of Plate 3.3, Plate 3.4, and Figure 3-8. Ideally, the only intensity variation in the data should be due to the presence of the 0.24 μm microsphere. However, there are significant intensity variations throughout each image, even though the microsphere occupies only a small space in the center of each image. We apply methods developed in the previous section to minimize the effects of this noise.

To quantify the effect of each method, we define a signal to noise ratio equal to the square of the peak-to-peak amplitude of the measured PSF divided by the corresponding spatial variance σ_v^2 estimated in the previous section.[2]

Row A of Plate 3.3, Plate 3.4, and Figure 3-8 illustrates unaveraged measurements. The maximum intensity of the PSF is 218 and the minimum is 96. Row A of Plate 3.1, Plate 3.2, and Figure 3-6 illustrates unaveraged measurements of $\beta_m[g_x, g_y, g_z]$, for which σ_v is equal to 8.1. The signal to noise ratio for Row A is therefore $(218 - 96)^2/8.1^2$, which is equal to 23.5 dB.

Row B of Plate 3.3, Plate 3.4, and Figure 3-8 shows the average of 100 repeated measurements of the PSF. The peak-to-peak amplitude of this average is 119. Row B of Plate 3.1, Plate 3.2, and Figure 3-6 illustrates the average of 100 repeated measurements of $\beta_m[g_x, g_y, g_z]$. The corresponding σ_v was 6.67, resulting in a signal to

---

[2]Note that in order to make this ratio useful, the gain, offset, and microscope illumination were set identically when $h_m[g_x, g_y, g_z]$ and $\beta_m[g_x, g_y, g_z]$ were measured.
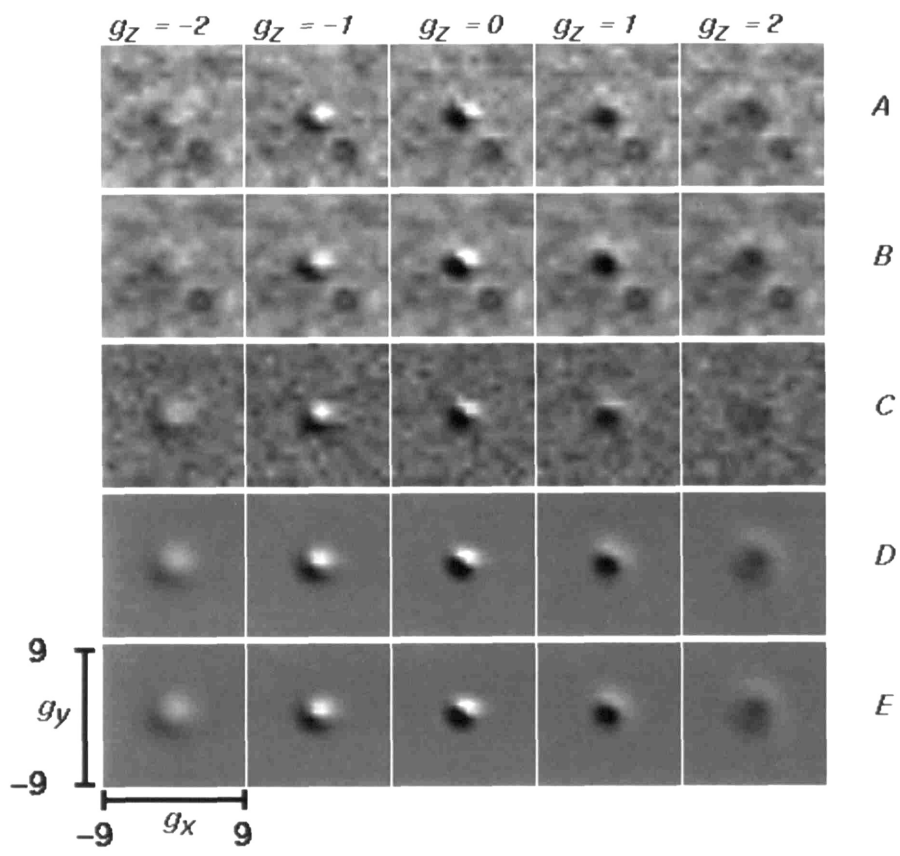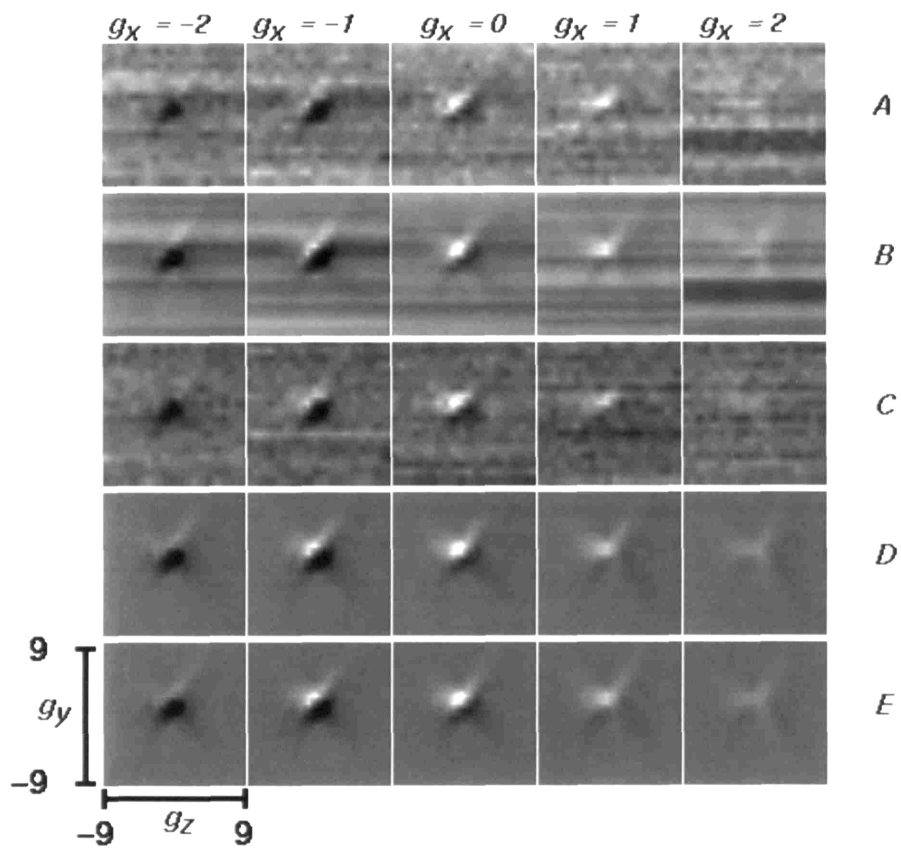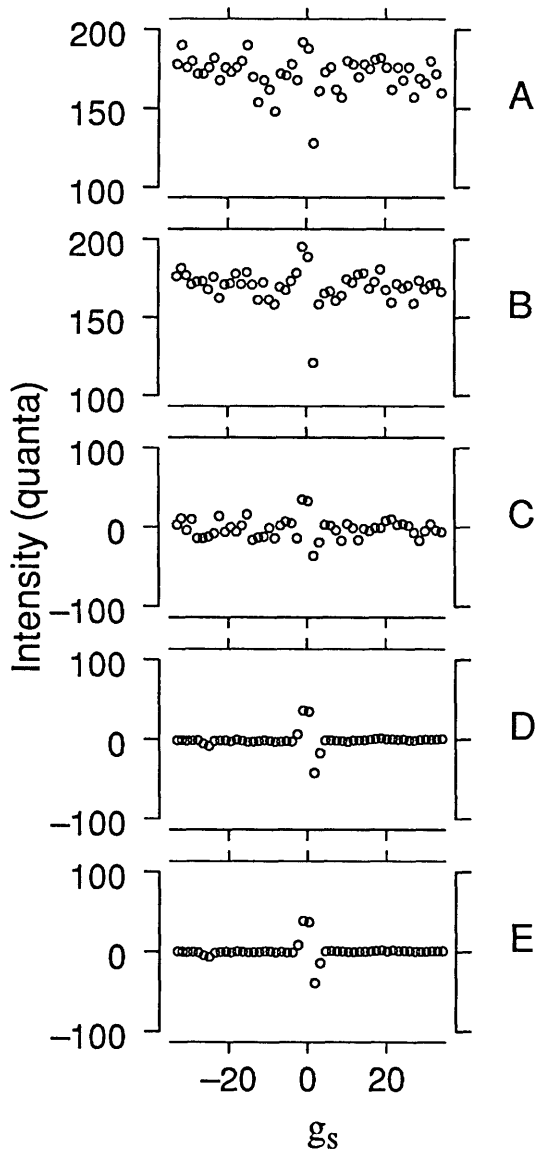
48

Plate 3.3

49

Plate 3.4

50

Figure 3-8: Measurements $h_m[g_x, g_y, g_z]$ of the PSF: Intensities along the shear direction s. These plots illustrate the same data shown in Plates 3.3 and 3.4. The sampling period along s is $T_s = \sqrt{T_x^2 + T_y^2} = \sqrt{2}/3$.

noise ratio equal to 25 dB.

Row C shows the PSF measurement after single focus background subtraction. This processing successfully removed background patterns that were independent of focus. For example, there is a black spot in the lower right corner of each image in Row A of Plate 3.3. This spot remained after averaging (Row B) but disappeared with single focus background subtraction (Row C). Nevertheless, the signal to noise ratio did not change significantly. The peak-to-peak amplitude in Row C is 127. The corresponding σ_v is 6.64, resulting in a signal to noise ratio equal to 25.5 dB.

Row D of Plate 3.3, Plate 3.4, and Figure 3-8 shows the PSF measurement after both averaging and single focus background subtraction. Intensity variations not due to the PSF are barely visible in Row D. Details of the PSF that were obscured by noise are now more apparent. For the $g_z = -2$ (left) column, the original image (Row A) seems to contain only noise, while Row D clearly shows information about the PSF. A second example of details that are more apparent in Row D can be seen in Plate 3.4. Faint diagonal lines that are part of the PSF can be seen in Row D more clearly than in Rows A, B, or C. The peak to peak amplitude of the PSF is 121, and corresponding σ_v is 1.43. Therefore the signal to noise ratio is 38.5 dB.

To implement linear background subtraction for $h_m[g_x, g_y, g_z]$, a line through z is estimated for each g_x and g_y using the voxels in the first 5 ($g_z = -10$ through -5) and the last 5 images ($g_z = 5$ through 10). These planes are used because they contain little PSF information, i.e. they represent the background surrounding the PSF. Row E of of Plate 3.3, Plate 3.4, and Figure 3-8 shows $h_m[g_x, g_y, g_z]$ after processing by linear background subtraction, averaging, and single focus background subtraction. The peak-to-peak value of the processed $h_m[g_x, g_y, g_z]$ is 120 and corresponding σ_v is 0.66. The resulting signal to noise ratio is 45 dB.

Without averaging or background subtraction, the signal to noise ratio was 23.5 dB. After processing, the signal to noise ratio was 45 dB. Thus our noise processing methods improved signal to noise ratio by more than an order of magnitude.

In subsequent sections we use the measurement in Row E to represent the microscope's PSF. Row E is actually the intensity pattern that results from transillumination of a microsphere with 0.24 μm diameter. This approximates a point source if and only if the volume occupied by the PSF is large compared to that of the microsphere. The diameter of the measured PSF (Figure 3-6, Row E) is about 1.66 μm (5 samples). This diameter is large compared to the 0.24 μm diameter of the microsphere, indicating that the point approximation is adequate.

We have found that the PSF of our microscope can be measured with the system described. These measurements are degraded by noise. We've characterized this noise as additive white noise and background degradations. Processing steps were identified (averaging, single focus background subtraction, linear background subtraction) that improve the quality of the PSF measurement.
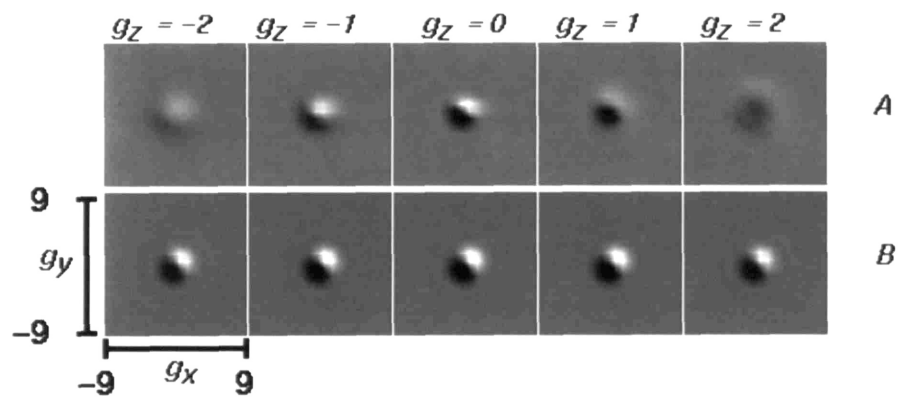
52

Plate 3.5: The theoretical and measured PSF. The top row (A) shows the x-y plane view of the measured PSF. Row B shows the theoretical PSF $h_{ad}[g_x, g_y, g_z]$ calculated with the aperture radius = 1.5, focal length = 4.6, and shear distance equal to 1/3 μm in x and 1/3 μm in y. The sampling period for both is $T_x = T_y = 1/3$ μm, $T_z = 1$ μm.

3.4 Comparison of Theoretical and Measured PSF

In this section we compare $h_{ad}[g_x, g_y, g_z]$, the theoretical PSF developed in Chapter 2, with $h_m[g_x, g_y, g_z]$, the measured PSF. The sampled theoretical PSF was obtained by discrete convolution of a sampled version of $h_a(\gamma_x, \gamma_y, \gamma_z)$ (Equation 2.1) with a sampled version of $h_d(\gamma_x, \gamma_y, \gamma_z)$ (Equation 2.32 with $s_x = s_y = 1/3$ μm). The sampling period was $T_x = T_y = 1/3$ μm, and $T_z = 1$ μm. When $h_{ad}[g_x, g_y, g_z]$ is evaluated using parameters for our microscope, its volume is much smaller than that of the measured PSF. Therefore, we reevaluated $h_{ad}[g_x, g_y, g_z]$ using a smaller aperture radius, 1.5 mm. This increases the volume of the theoretical PSF and simplifies comparing the shapes of the theoretical and measured PSFs in the x-y plane (Plates 3.5 and 3.6). Qualitatively, the measured and theoretical PSFs are similar. Both show similar dependence on shear direction (Plate 3.5) and radii in the x-y planes are similar. However there are differences. First, the theoretical PSF is symmetric about $g_z = 0$ but the measured PSF switches from primarily bright above focus to primarily dark below focus. Second, the extent along z for the theoretical PSF (Plate 3.6) greatly exceeds that for the measured PSF. This mismatch could be reduced by increasing the aperture radius used to compute the theoretical PSF. However, such an increase causes considerable mismatch in the x-y plane.

Differences in measured and theoretical PSFs have been noted in the literature [18, 11]. These differences could result because of inadequacies of our models for finite aperture diffraction [7] and DIC . Alternatively, these differences could arise from physical mechanisms that are ignored in the theory, such as lens aberrations, incorrect tube length, defocusing, and incorrect cover slip thickness. A true theoretical PSF calculation is quite complicated and may even be impossible since the exact lens specifications of the microscope are usually proprietary [18]. For this reason image processing on real microscope images will be accomplished using the measured PSF. The theoretical PSF derived with an aperture radius of 1.5 mm will be used only for creating simulations.

Plate 3.6: The theoretical and measured PSF. This plate illustrates the same PSF as Plate 3.5 from a different view. The top row (A) shows the z-y plane view of the measured PSF. Row B shows the theoretical PSF $h_{ad}[g_x, g_y, g_z]$.

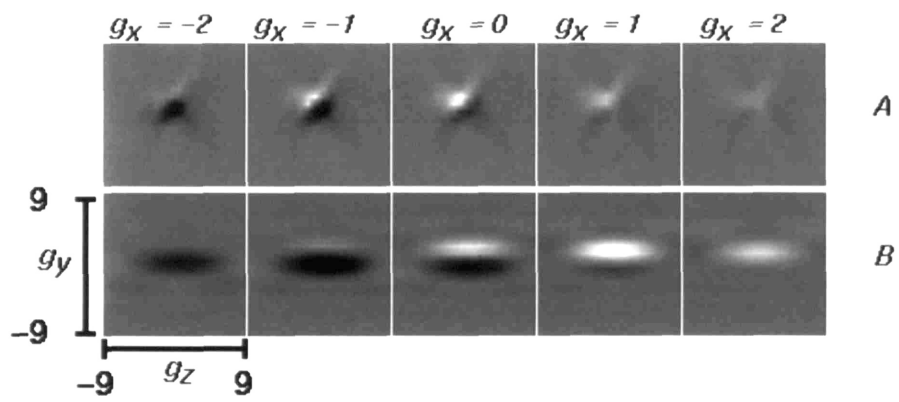$g_z = -2$ $g_z = -1$ $g_z = 0$ $g_z = 1$ $g_z = 2$

A

9

g_y

−9

−9 g_x 9

B

Plate 3.5

$g_X = -2$ $g_X = -1$ $g_X = 0$ $g_X = 1$ $g_X = 2$

A

B

9

g_y

−9

−9 g_Z 9

Plate 3.6

56

Chapter 4

Deconvolution

4.1 Method

In this chapter, we develop a signal processing method to estimate the refractive index of a transparent specimen from images obtained from a compound microscope with DIC optics. For the purposes of developing the signal processing method we assume that the measurements can be modeled as

$$i_m[g_x, g_y, g_z] = c\phi(g_x T_x, g_y T_y, g_z T_z) * h(g_x T_x, g_y T_y, g_z T_z) + n(g_x T_x, g_y T_y, g_z T_z). \quad (4.1)$$

This relation is derived from Equation 3.5 by removing the constant background, neglecting the effects of quantization and including the noise term $n(g_x T_x, g_y T_y, g_z T_z)$. Since $\phi(g_x T_x, g_y T_y, g_z T_z)$ is proportional to the refractive index in the specimen, we express the measured intensity as

$$i_m[g_x, g_y, g_z] = o[g_x, g_y, g_z] * h[g_x, g_y, g_z] + n[g_x, g_y, g_z], \quad (4.2)$$

where $o[g_x, g_y, g_z]$ represents the normalized refractive index in the sampled region. We refer to $o[g_x, g_y, g_z]$ as the object (or specimen) in our signal processing model. Our goal is to obtain an estimate $\hat{o}[g_x, g_y, g_z]$ of the object $o[g_x, g_y, g_z]$ based on observations of $i_m[g_x, g_y, g_z]$.

Consider the discrete Fourier transform [13] of Equation 4.2,

$$I_m[w_x, w_y, w_z] = O[w_x, w_y, w_z]H[w_x, w_y, w_z] + N[w_x, w_y, w_z]. \quad (4.3)$$

If there is no noise, then $O[w_x, w_y, w_z]$ can be recovered from $I_m[w_x, w_y, w_z]$ by multiplication with an inverse filter $H^{-1}[w_x, w_y, w_z]$ that satisfies

$$H[w_x, w_y, w_z]H^{-1}[w_x, w_y, w_z] = 1. \quad (4.4)$$

This direct deconvolution has limitations. For example, $H^{-1}[w_x, w_y, w_z]$ is not defined at frequencies where $H[w_x, w_y, w_z]$ is zero. The presence of noise creates further difficulties, especially at frequencies where $|N[w_x, w_y, w_z]|$ is large compared to $|O[w_x, w_y, w_z]H[w_x, w_y, w_z]|$. If $H^{-1}[w_x, w_y, w_z]$ is large at such frequencies, multiplying $I_m[w_x, w_y, w_z]$ by $H^{-1}[w_x, w_y, w_z]$ will accentuate the noise.

4.1.1 Weiner Deconvolution

Weiner filtering provides the optimal least mean square estimate of a stationary signal contaminated by additive gaussian noise. Let

$$S[w_x, w_y, w_z] = O[w_x, w_y, w_z]H[w_x, w_y, w_z], \tag{4.5}$$

so that

$$I_m[w_x, w_y, w_z] = S[w_x, w_y, w_z] + N[w_x, w_y, w_z]. \tag{4.6}$$

The Weiner filter $W[w_x, w_y, w_z]$ used to estimate $S[w_x, w_y, w_z]$ from $I_m[w_x, w_y, w_z]$ is given by

$$W[w_x, w_y, w_z] = \frac{P_S[w_x, w_y, w_z]}{P_S[w_x, w_y, w_z] + P_N[w_x, w_y, w_z]}, \tag{4.7}$$

where

$$P_S[w_x, w_y, w_z] \propto S[w_x, w_y, w_z]S^*[w_x, w_y, w_z] \tag{4.8}$$

and

$$P_N[w_x, w_y, w_z] \propto N[w_x, w_y, w_z]N^*[w_x, w_y, w_z]. \tag{4.9}$$

$P_S[w_x, w_y, w_z]$ can be written as

$$P_S[w_x, w_y, w_z] = O[w_x, w_y, w_z]O^*[w_x, w_y, w_z]H[w_x, w_y, w_z]H^*[w_x, w_y, w_z]. \tag{4.10}$$

Therefore when the Weiner filter and the inverse filter $H^{-1}[w_x, w_y, w_z]$ are combined, the resulting filter $D[w_x, w_y, w_z]$ is given by (See [13])

$$D[w_x, w_y, w_z] = \frac{P_O[w_x, w_y, w_z]H^*[w_x, w_y, w_z]}{P_O[w_x, w_y, w_z]H[w_x, w_y, w_z]H^*[w_x, w_y, w_z] + P_N[w_x, w_y, w_z]} \tag{4.11}$$

or

$$D[w_x, w_y, w_z] = \frac{H^*[w_x, w_y, w_z]}{H[w_x, w_y, w_z]H^*[w_x, w_y, w_z] + P_N[w_x, w_y, w_z]/P_O[w_x, w_y, w_z]}, \tag{4.12}$$

where $P_O[w_x, w_y, w_z]$ is the power spectrum of the object that is to be estimated. Unfortunately, it is not generally possible to measure $P_O[w_x, w_y, w_z]$. In practice, the noise to signal ratio in the denominator of this equation is often assumed to be

constant. Because this assumption simplifies analysis and has been found to yield useful deconvolution [1, 2], we shall make this assumption. Substituting the constant η into the deconvolution filter, we obtain the approximate deconvolution filter

$$D_a[w_x, w_y, w_z] = \frac{H^*[w_x, w_y, w_z]}{|H[w_x, w_y, w_z]|^2 + \eta}. \qquad (4.13)$$

When η is small compared to $|H[w_x, w_y, w_z]|^2$,

$$D_a[w_x, w_y, w_z] \approx \frac{1}{H[w_x, w_y, w_z]} \qquad (4.14)$$

and when η is large compared to $|H(w_x, w_y, w_z]|^2$,

$$D_a[w_x, w_y, w_z] \approx \frac{H^*[w_x, w_y, w_z]}{\eta}. \qquad (4.15)$$

At frequencies where the signal to noise ratio is expected to be large, the Weiner deconvolution filter looks like the direct inverse filter. When the signal to noise ratio is low, the deconvolution filter is small so noise is not amplified.

4.1.2 Application of Weiner Deconvolution to Nomarski DIC Images

The special form of the PSF for a microscope equipped with Nomarski optics has important implications for Weiner deconvolution. In order to explore these implications, we shall first examine mathematical models of the effects of differential interference contrast and of the finite aperture of the microscope. In Section 2.6 we found that the theoretical PSF $h_{ad}(\gamma_x, \gamma_y, \gamma_z)$ of a Nomarski microscope can be expressed as

$$h_{ad}(\gamma_x, \gamma_y, \gamma_z) = h_a(\gamma_x, \gamma_y, \gamma_z) * h_d(\gamma_x, \gamma_y, \gamma_z). \qquad (4.16)$$

The blurring due to the finite apertures of the optical elements is represented by $h_a(\gamma_x, \gamma_y, \gamma_z)$. The general form of $h_a(\gamma_x, \gamma_y, \gamma_z)$ is given in Equation 2.1. We evaluated this relation using an aperture radius of 1.5 mm and a focal length of 4.6 mm [1]. The directional differentiation due to the Nomarski optics is represented by $h_d(\gamma_x, \gamma_y, \gamma_z)$ given in Equation 2.32, evaluated with $s_x = s_y = 1/3$ μm.

We seek a discrete representation of Equation 4.16. To that end, $h_a(\gamma_x, \gamma_y, \gamma_z)$ and $h_d(\gamma_x, \gamma_y, \gamma_z)$ are sampled to generate

$$h_a[g_x, g_y, g_z] = h_a(g_x T_x, g_y T_y, g_z T_z) \qquad (4.17)$$

---

[1]Although our microscope has an aperture of 3.5 mm radius, we found that evaluation of the relation with a 1.5 mm radius gave results that were closer to the measured PSF (See Section 3.4).

Plate 4.1: Frequency domain representation of the PSF of a microscope equipped with Nomarski optics. Row A illustrates the magnitude of $H_a[w_x, w_y, w_z]$ (Equation 2.1 with $a = 1.5$ mm and $f = 4.6$ mm) which represents the effect of blurring due to finite aperture. Row B illustrates the magnitude of $H_d[w_x, w_y, w_z]$ (Equation 2.32 with $s_x = s_y = 1/3$ μm), which represents the effects of Nomarski DIC. Row C illustrates the magnitude of $H_{ad}[w_x, w_y, w_z]$ (Equation 4.19), which represents the combined effects of H_a and H_d. The frequency representations were obtained by performing a 64^3 3D FFT [17] of sampled versions of h_a, h_d, and h_{ad}. The sampling period was $T_x = T_y = 1/3$ μm and $T_z = 1\mu$m. In each row, black corresponds to the smallest magnitude in the row (0) and white corresponds to the largest magnitude: 337.1 (Row A), 2 (Row B), and 48.6 (Row C).

and

$$h_d[g_x, g_y, g_z] = h_d(g_x T_x, g_y T_y, g_z T_z), \tag{4.18}$$

where $T_x = T_y = 1/3$ μm, and $T_z = 1\mu$m.

The discrete Fourier transform of Equation 4.16 is

$$H_{ad}[w_x, w_y, w_z] = H_a[w_x, w_y, w_z]H_d[w_x, w_y, w_z]. \tag{4.19}$$

The Fourier transform of a PSF is referred to as a transfer function. We first consider the transfer function $H_a[w_x, w_y, w_z]$ due to finite aperture diffraction. The magnitude of $H_a[w_x, w_y, 0]$ is illustrated in Row A of Plate 4.1 and Figure 4-1. Notice that this transfer function is a low pass filter. As noted in Section 2.1 this transfer function is cylindrically symmetric, and the blurring in z is more significant than in x and y.

Next consider $H_d[w_x, w_y, w_z]$ the part of the transfer function that is due to Nomarski optics. With $s_x = s_y = T_x = T_y$, the discrete M point Fourier transform of $h_d[g_x, g_y, g_z]$ is

$$H_d[w_x, w_x, w_y] = 1 - e^{-j\frac{2\pi}{M}(w_x + w_y)}. \tag{4.20}$$

Row B of Plate 4.1 and Figure 4-1 illustrate $|H_d[w_x, w_y, 0]|$ for M = 64. We see that at low frequencies, this frequency response is that of a directional high pass filter.

Plate 4.1 and Figure 4-1 illustrate $|H_{ad}[w_x, w_y, 0]|$. Along the shear direction $|H_{ad}[w_x, w_y, 0]|$ decreases to zero for both high and low frequencies, it is a bandpass filter. Orthogonal to the shear direction, $|H_{ad}[w_x, w_y, 0]|$ is zero.

To understand the special issues that affect Weiner deconvolution of DIC images, we compare this problem to the deconvolution of images that are simply blurred by diffraction. The primary goal in the latter case is to amplify high frequencies that are attenuated by blurring. In DIC, we want to do this same deblurring, but we also want to reconstruct low frequencies that were lost due to Nomarski DIC differentiation. In both cases, object information at high frequencies cannot be reconstructed because

60

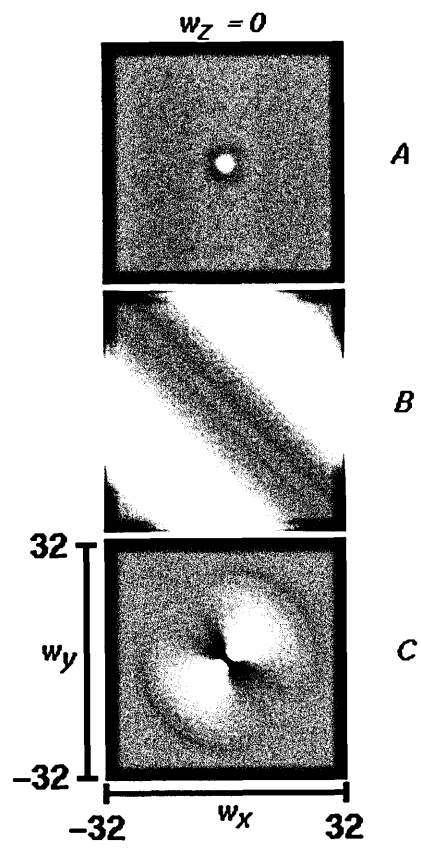$w_Z = 0$

A

B

32

w_y

−32
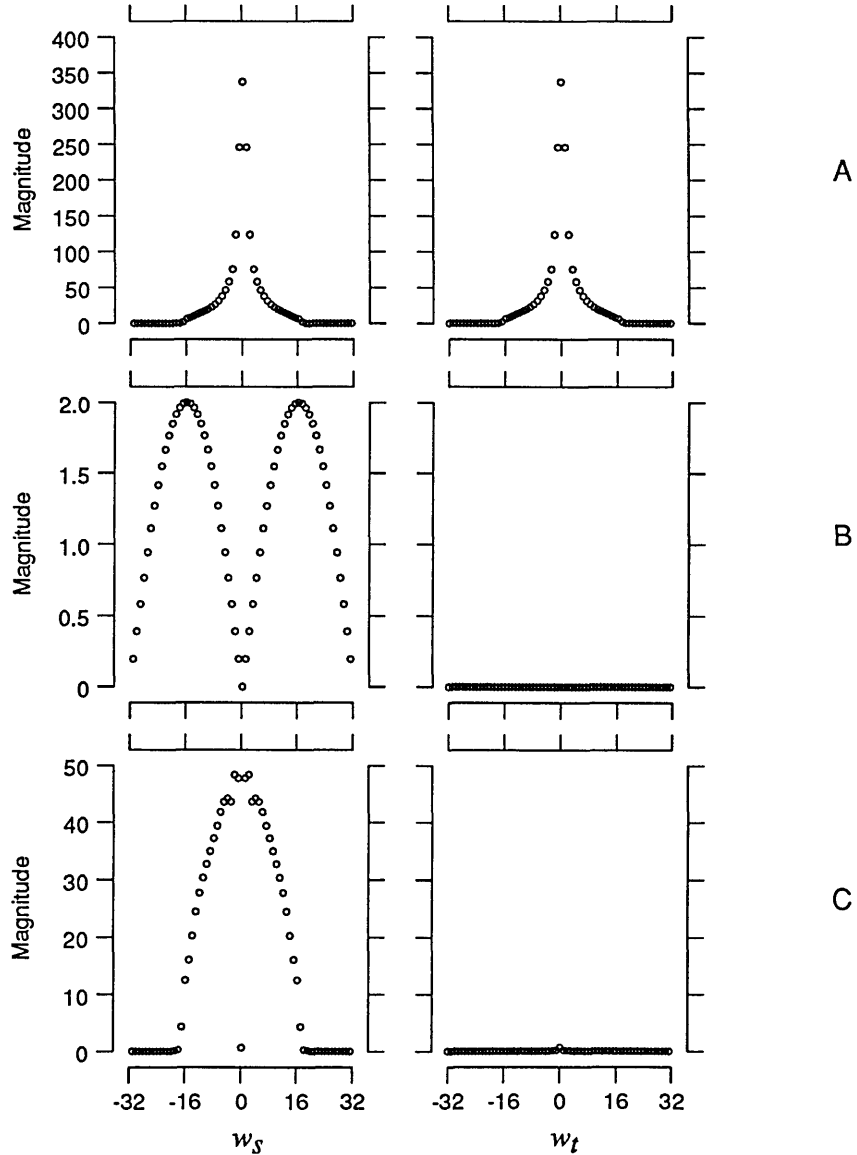
C

−32 w_x 32

Plate 4.1

Figure 4-1: Frequency domain representation of the PSF of a microscope equipped with Nomarski optics. These rows illustrate $|H_a[w_x, w_y, 0]|$ (Row A), $|H_d[w_x, w_y, 0]|$ (Row B), and $|H_{ad}[w_x, w_y, 0]|$ (Row C) as a function of w_s with $w_z = 0$ (left), and w_t (right) with $w_z = 0$. The index w_s is used to denote the discrete frequencies along the shear direction s and w_t denotes the discrete frequencies orthogonal to s. The frequency samples along s and t are separated by $\sqrt{2}\ 2\pi/64$ radians.

Plate 4.2: The spherical object and simulated microscope images. Each row illustrates five images orthogonal to z: with $g_z = -6$ (left), -3, 0, 3, 6. Each image shows intensity variations for g_x from -19 to 19 and g_y from -19 to 19. Row A shows o$[g_x,g_y,g_z]$, samples of the spherical object defined in Equation 4.21. Row B illustrates the simulated microscope images or equivalently the simulated discrete intensity $i[g_x,g_y,g_z]$. This simulation was constructed by convolving the discretized spherical object o$[g_x,g_y,g_z]$ with the theoretical PSF $h_{ad}[g_x, g_y, g_z]$ (Equation 2.32 evaluated with an objective aperture of 1.5 mm, an objective focal length of 4.6 mm and a shear distance $s_x = s_y = 1/3$ μm.) Gaussian white noise with variance equal to 0.01 was added.

Plate 4.3: The spherical object and simulated microscope images: y-z views. This plate shows y-z views of the same data shown in Plate 4.2.

$H_a[w_x, w_y, w_z]$ is close to zero. In DIC gradients perpendicular to the shear direction cannot be reconstructed either.

Examination of $H_{ad}[w_x, w_y, 0]$ also indicates potential problems with DIC deconvolution based on measured PSFs. Measured PSFs are expected to be small at both high and low frequencies. Where the PSF is small, the measurement is particularly sensitive to measurement noise. Low frequency degradation (such as nonuniformities in the microscope illumination system) that would not normally be a problem can have large effects.

4.2 Deconvolving Simulated Microscope Images

To test these image processing methods, we have used simulated microscope images. Images are simulated using Equation 4.2 with $h[g_x, g_y, g_z]$ equal to the theoretical $h_{ad}[g_x, g_y, g_z]$ and $n[g_x, g_y, g_z]$ obtained from a Gaussian white noise generator. Simulations give us the benefit of a priori knowledge of the object o$[g_x,g_y,g_z]$. This provides a reference for comparison with the deconvolution results. In addition, the simulations allow us to isolate degradations so that we can clearly see their effect. Through these tests, we hope to determine the fundamental limits of the methods and how known degradations affect these limits.

To test the deconvolution method, we applied it to simulated images of a sphere. The sphere is defined on a volume of 41 × 41 × 41 voxels, as

$$o[g_x, g_y, g_z] \begin{aligned} &= 1 \quad \text{if} (T_x g_x)^2 + (T_y g_y)^2 + (T_z g_z)^2 < R^2 \\ &= 0 \qquad \text{otherwise,} \end{aligned} \tag{4.21}$$

where $T_x = T_y = 1/3$ μm, $T_z = 1$ μm, and $R = 3/2$ μm. The simulated images were

$g_Z = -6$ $g_Z = -3$ $g_Z = 0$ $g_Z = 3$ $g_Z = 6$
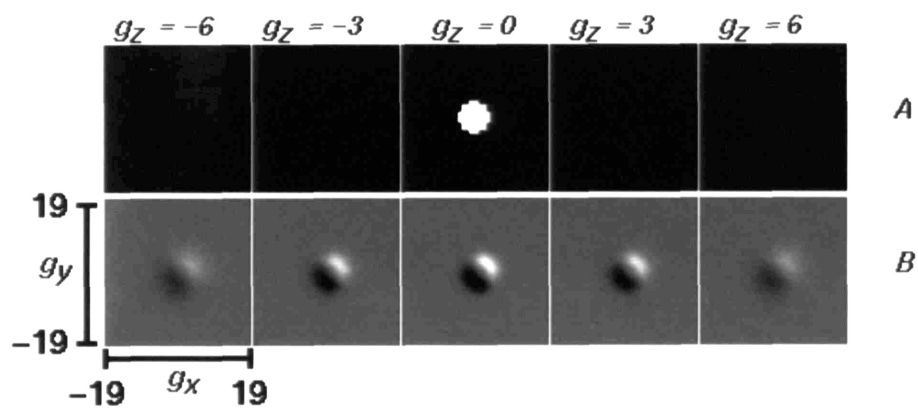
A
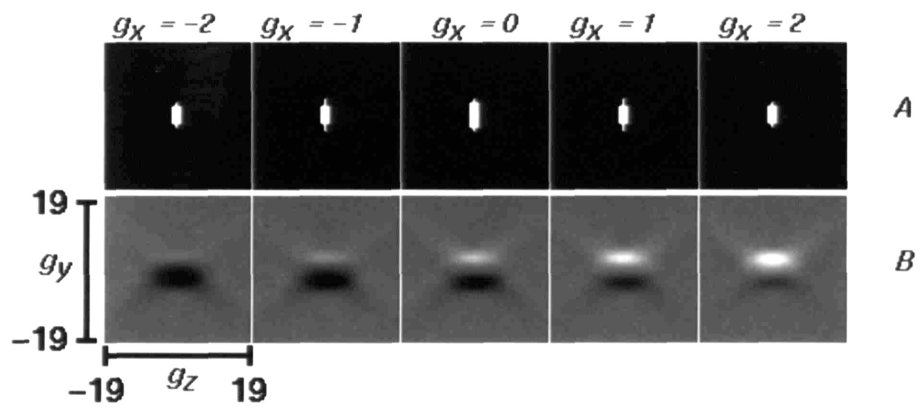
19
g_y
−19

B

−19 g_x 19
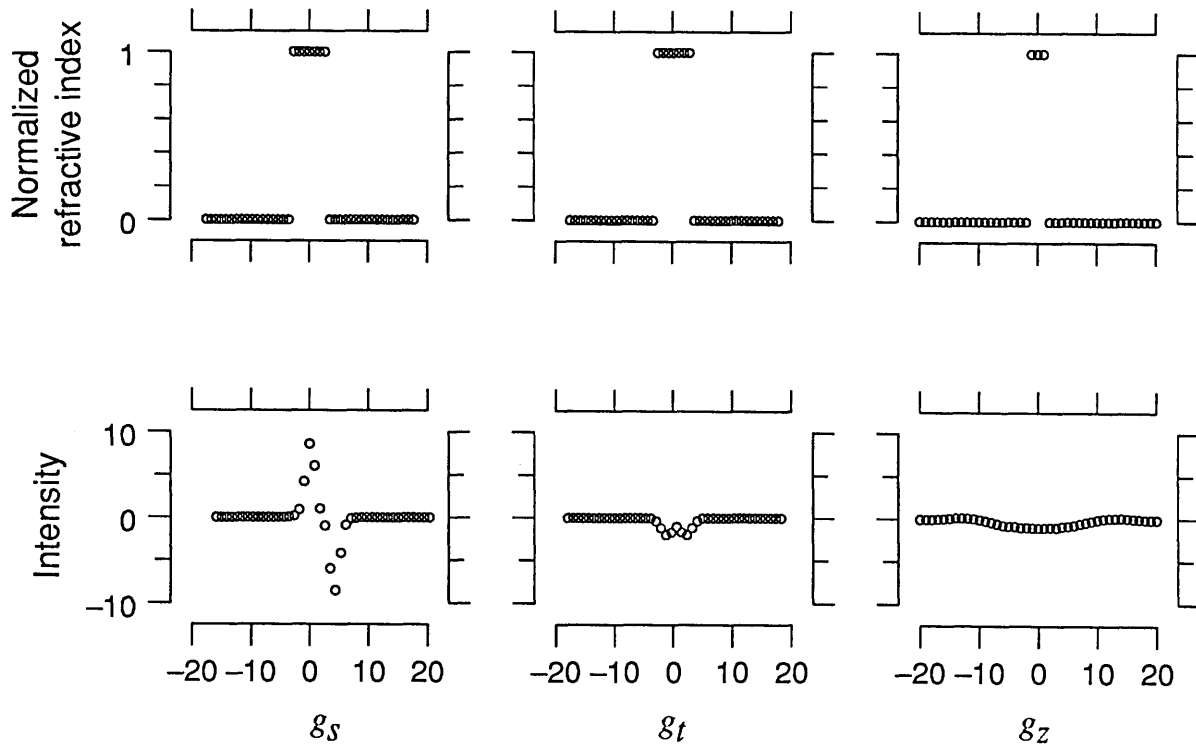
Plate 4.2

64

Plate 4.3

65

Figure 4-2: The spherical object and simulated microscope images: intensity plots. This figure illustrates the same object and simulated images shown in Plates 4.2 and 4.3. Row A illustrates refractive index of the spherical object along a line through the origin and parallel to s (left), t (middle) and z (right). Row B illustrates intensities in the simulated images along these axes. All parameters are as in Plate 4.2.
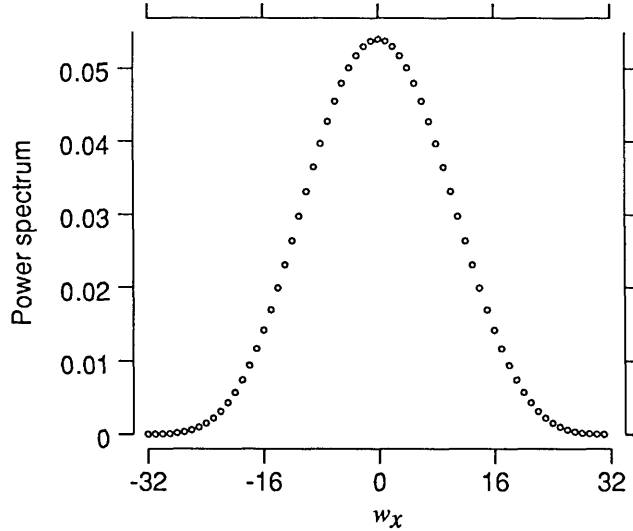
Figure 4-3: Power Spectrum of the spherical object. This figure illustrates the power spectrum $P_O[w_x, w_y, w_z]$ along w_x with $w_y = w_z = 0$. The power spectrum was computed using Equation 4.22 for the spherical test object defined in Equation 4.21.

Plate 4.4: Deconvolution of simulated sphere images contaminated by noise with $\sigma_n^2 = 0.01$. Each row illustrates five images orthogonal to z: with $g_z = -4$ (left), -2, $0, 2, 4$. Each image shows intensity variations for g_x from -19 to 19 and g_y from -19 to 19. A: Spherical test object. B: Results of deconvolution by Equation 4.12. C: Results of deconvolution by Equation 4.13 with $\eta = 0.04$. D: Results of deconvolution by Equation 4.13 with $\eta = 0.4$. E: Results of deconvolution by Equation 4.13 with $\eta = 4$. The FFT size used in the deconvolution was 64^3. The deconvolution was implemented using a 64^3 FFT.

Plate 4.5: Deconvolution of simulated sphere images contaminated by noise with $\sigma_n^2 = 0.01$: z-y views. This plate shows z-y views for the same data shown in Plate 4.4.
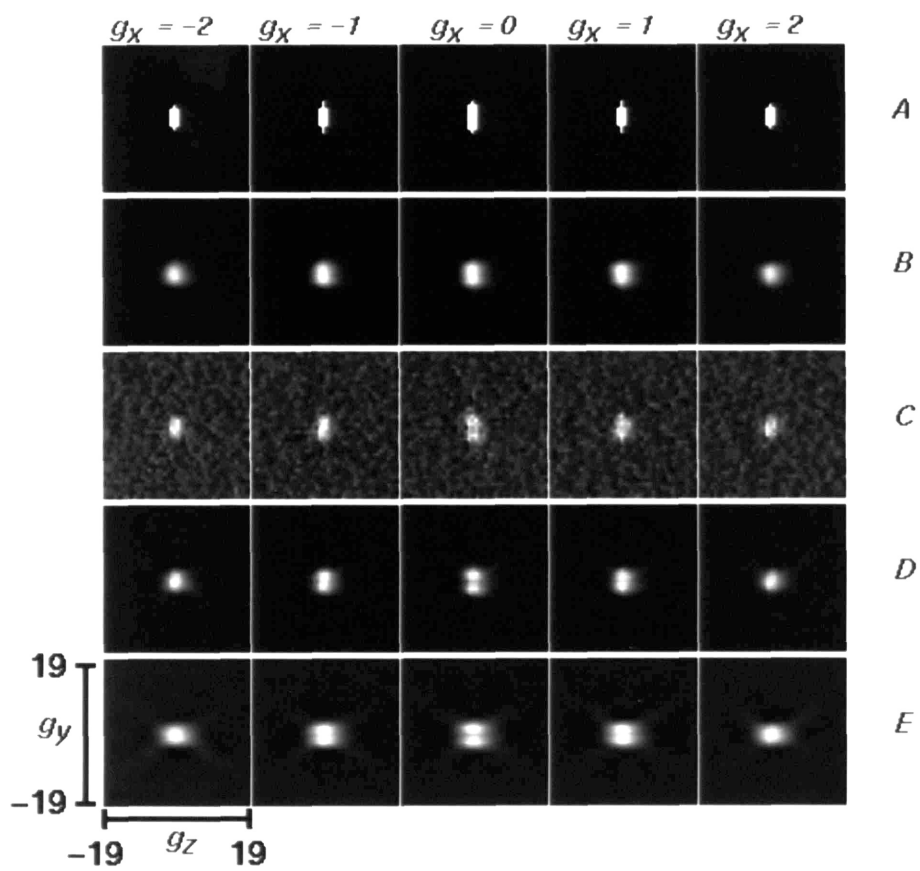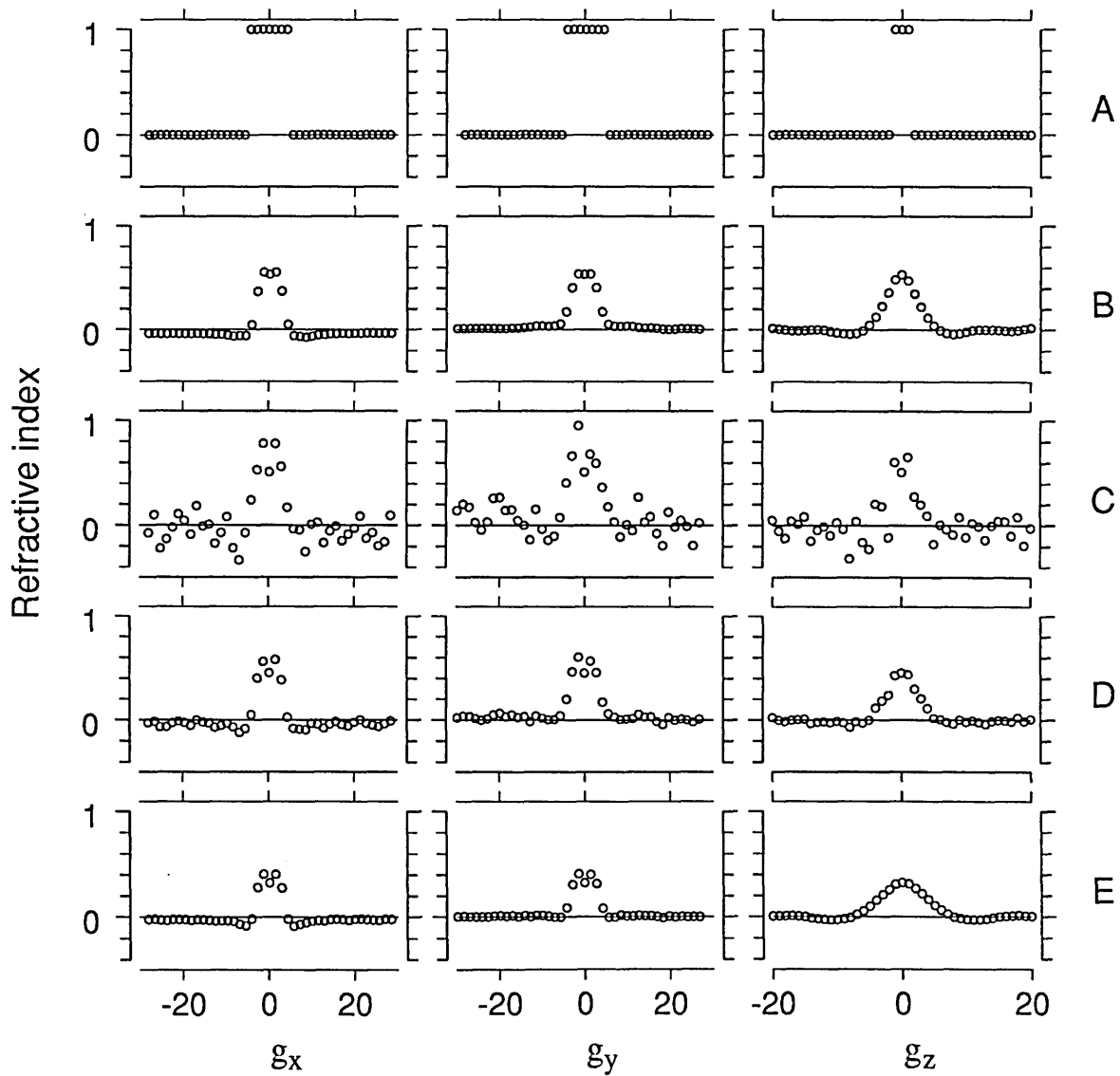
Plate 4.4

68

Plate 4.5

69
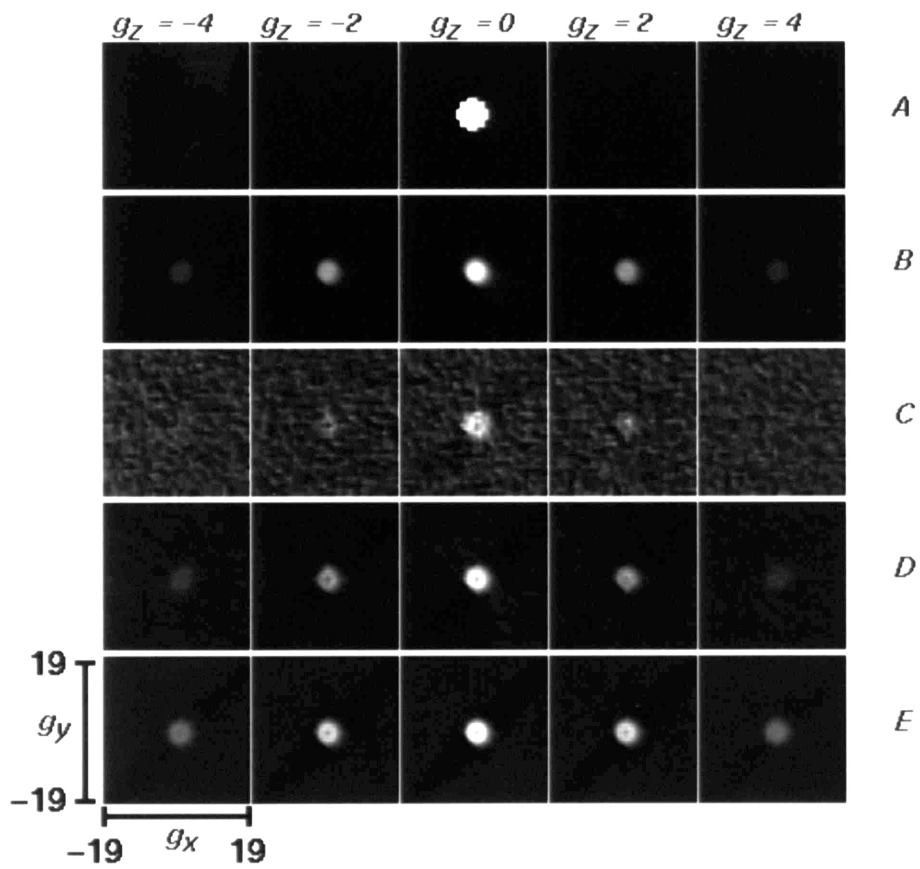
Figure 4-4: Deconvolution of simulated sphere images contaminated by noise with $\sigma_n^2 = 0.01$: intensity plots. This figure shows results for the same data shown in Plates 4.4 and 4.5. The rows illustrate deconvolution results (refractive index) along a line through the origin and parallel to s (left), t (middle) and z (right).

obtained by convolving samples of a sphere with the theoretical PSF $h_{ad}[g_x, g_y, g_z]$ (Plates 3.5 and 3.6) and adding Gaussian white noise with variance $\sigma = 0.01$. This value was chosen so that the ratio of peak-to-peak signal intensity (17 for the simulated sphere) to noise intensity was 45 dB, similar to that measured in Chapter 2.

Because the power spectrum of the object is known, we use the Weiner deconvolution filter $D[g_x, g_y, g_z]$ defined in Equation 4.12 to estimate the object from the simulated images. To obtain the object power spectrum, we can use a periodogram estimate [13]

$$P_O[w_x, w_y, w_z] = \frac{|O(w_x, w_y, w_z)|^2}{M}, \tag{4.22}$$

where $O[w_x, w_y, w_z]$ is the spherical test object (Equation 4.21) and $M=64^3$ is the number of points in the discrete Fourier transform. The resulting spectrum is shown in Figure 4-3. The noise power is equal to the variance of the added noise,

$$P_N[w_x, w_y, w_z] = \sigma^2 = 0.01. \tag{4.23}$$

The result of convolving the Weiner deconvolution filter

$$D[w_x, w_y, w_z] = H_{ad}^*/(|H_{ad}|^2 + P_N/P_O) \tag{4.24}$$

with the simulated images is shown in Row B of Plate 4.4, Plate 4.5, and Figure 4-4. The results appear to have sufficient noise reduction. Also the effect of Nomarski differentiation (a prominent dark and white peak along s in Row B of Plate 4.2 and Figure 4-2) has been removed. Therefore the results can be easily interpreted as a sphere of higher refractive index than the background.

Although the estimated objects in Row B are blurred compared to the originals in Row A they are much less blurred than the simulated images (Compare Row B of Plates 4.2 and 4.4 with Plates 4.3 and 4.5. The reason that the deblurring is not perfect is that frequencies where the transfer function is small could not be reconstructed. From the plots of Row B Figure 4-4, it is clear that the blur remaining after deconvolution is most significant along z. Because the PSF blurs more along z, this is the direction that the reconstruction will be poorest.

The deconvolution was performed with the approximate deconvolution filter $D_a[w_x, w_y, w_z]$ defined in Equation 4.13. The value of η should be chosen to approximate the ratio of power in the noise to power in the signal. The power in the noise is 0.01. The power in the signal varies from 0 to 0.05 (Figure 4-3). We chose η to be 0.01 divided by half the maximum power in the signal,

$$\eta = 0.01/0.025 = 0.4. \tag{4.25}$$

We want to determine the effect of overestimating and underestimating the value η. To do this, we repeat the deconvolution with η ten times larger and ten times smaller

than our original estimate, i.e. $\eta = 0.04$ and $\eta = 4$ respectively. Rows C through E of Plate 4.4, Plate 4.4, and Figure 4-4 illustrate the deconvolutions corresponding to $\eta = 0.04$, 0.4 and 4.

From the results of Plate 4.4, Plate 4.5, and Figure 4-4 we can draw several conclusions. First, when η is too low (Row C), noise dominates the result. Conversely, when η is too large (Row E), high frequency information is not reconstructed sufficiently, i.e. the results are too blurred. When a reasonable value of η is used (Row D), the approximate deconvolution results are comparable to the deconvolution results of (Row B).

Although the results of Row B and Row D similar, there are differences that illustrate limitations of the constant approximation. Notice that noise is still apparent in Row D of Figure 4-4. If η is increased to reduce this noise (Row E), the results become blurred before the noise power is as small as that seen in Row B. Another difference between Row B and Row D is a dip in the center of the reconstructed sphere (most noticeable in Figure 4-4) of Row D. This dip indicates that the deconvolution filter is overemphasizing high frequencies. This results because the constant approximation underestimates the noise to signal ratio at high frequencies.

4.3 Deconvolving Microscope Images of Test Objects

We also tested our image processing methods using measured intensities from test objects with known structure. The test objects were transparent polystyrene microspheres (Polyscience) with diameters of 2.0, 2.8, and 4.6 μm. The deconvolution filters were based on measurements of the microscope's PSF (Chapter 3, Section 3.3) and measurements of the noise in the system (Chapter 3, Section 3.2). Because the power spectrum of the object was known *a priori*, this information could have been used to implement the ideal Weiner filter given in Equation 4.12. However, our goal was to evaluate how well the image processing methods would work if no information about the object were available. We therefore implemented only the approximate deconvolution filter given in Equation 4.13. Three different values of the constant η are illustrated for every set of measured data.

It was not always possible to measure the test objects and PSF without altering the illumination system for the microscope and the gain and offset controls for the camera. Therefore, the deconvolution results are proportional to the index of refraction of the test object, but the constant of proportionality is not known. We report such results as normalized refractive index.

Results for the 2.0 μm microsphere (Plate 4.6, Plate 4.7, and Figure 4-5) and for the 2.8 μm microsphere (Plate 4.8, Plate 4.9, and Figure 4-6) are generally similar.

Plate 4.6: Deconvolution of 2.0 μm microsphere images. Intensities from a 2 μm microsphere (51 × 51 × 61 voxels) were measured as described in Chapter 3 (i.e. with linear background subtraction and averaging) and are illustrated in Row A. The DC value was subtracted. The data were windowed with a three dimensional Hamming window [13] and deconvolved using Equation 4.13 with a measured PSF (Chapter 3). Results are shown for three different values of η: 10 (Row B), 1000 (Row C), and 10000 (Row D). Each row illustrates five images orthogonal to z: with $g_z = -2$ (left), -1, 0, 1, 2. Each image shows intensity variations for g_x from -19 to 19 and g_y from -19 to 19.

Plate 4.7: Deconvolution of 2.0 μm microsphere images: y-z views. This plate shows y-z views of the same data shown in Plate 4.6.

We make comments about results for the 2.0 μm microsphere, but similar comments equally apply for results for the 2.8 μm microsphere.

The measured images exhibit the shadowing effect that is typical of Nomarski images. For example, the center image of Row A in Plate 4.6 is black in the lower left region and white in the upper right. This shadowing effect is greatly reduced by deconvolution. The center images in Rows B, C, and D in Plate 4.6 are nearly radially symmetric. Only the second images in Rows C and D show obvious asymmetries.

Deconvolution simplifies interpretation of the images in terms of index of refraction. The microspheres are known to be regions of high refractive index surrounded by the lower refractive index of the medium. This interpretation in clear from Rows B, C, and D in Plate 4.6 and much less apparent from the measured images in Row A.

Blurring along the optical axis of the microscope is reduced by deconvolution. The measured data in the center image of Row A in Plate 4.7 has greater extent in the z direction than that of any of the corresponding results after deconvolution.

Both the measured images in Plate 4.7 and the results after deconvolution contain diagonal lines drawn from the center of the microsphere. These diagonals in the z-y plane can also be seen in x-y images. They appear as open circles in the last images in Rows B, C, and D of Plate 4.7 and as larger circles for larger values of g_z (not shown). Thus, these artifacts would fall on the surface of an elliptic cone if viewed in three dimensions. Because similar patterns are apparent in the simulated images of a 3 μm microsphere (Plates 4.2 and 4.3), they result from the three dimensional structure of the PSF. These patterns in the simulated images were removed by ideal Weiner filtering (Row B of Plates 4.4 and 4.5) and are greatly diminished by the approximate Weiner filtering illustrated in Rows C, D, and E. The fact that these patterns in the measured images of Plate 4.7 are not removed by deconvolution suggests that the measured PSF may not have accurately represented all of the three dimensional
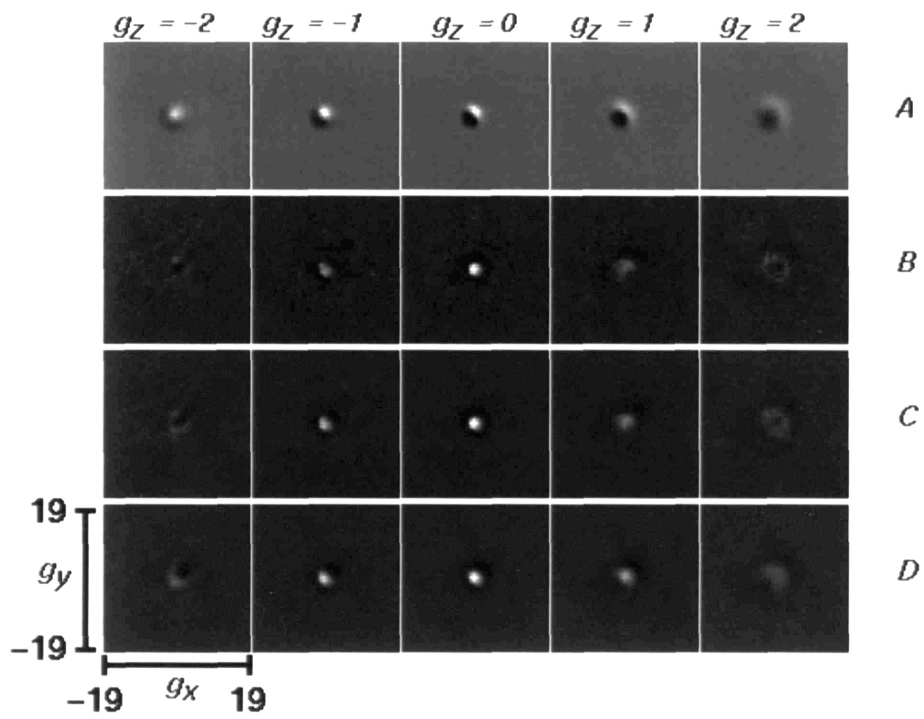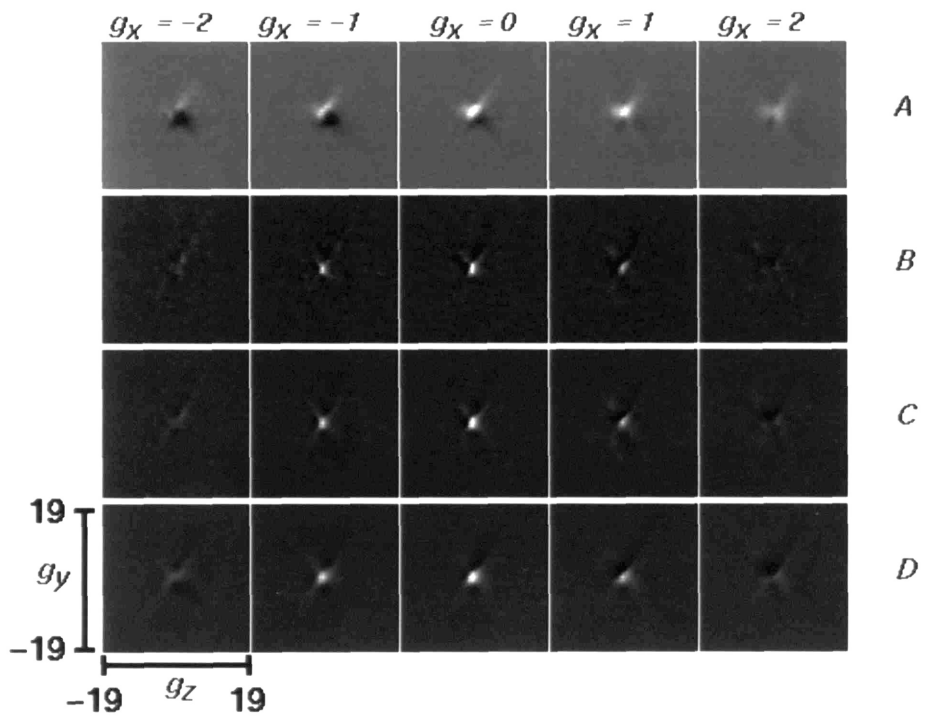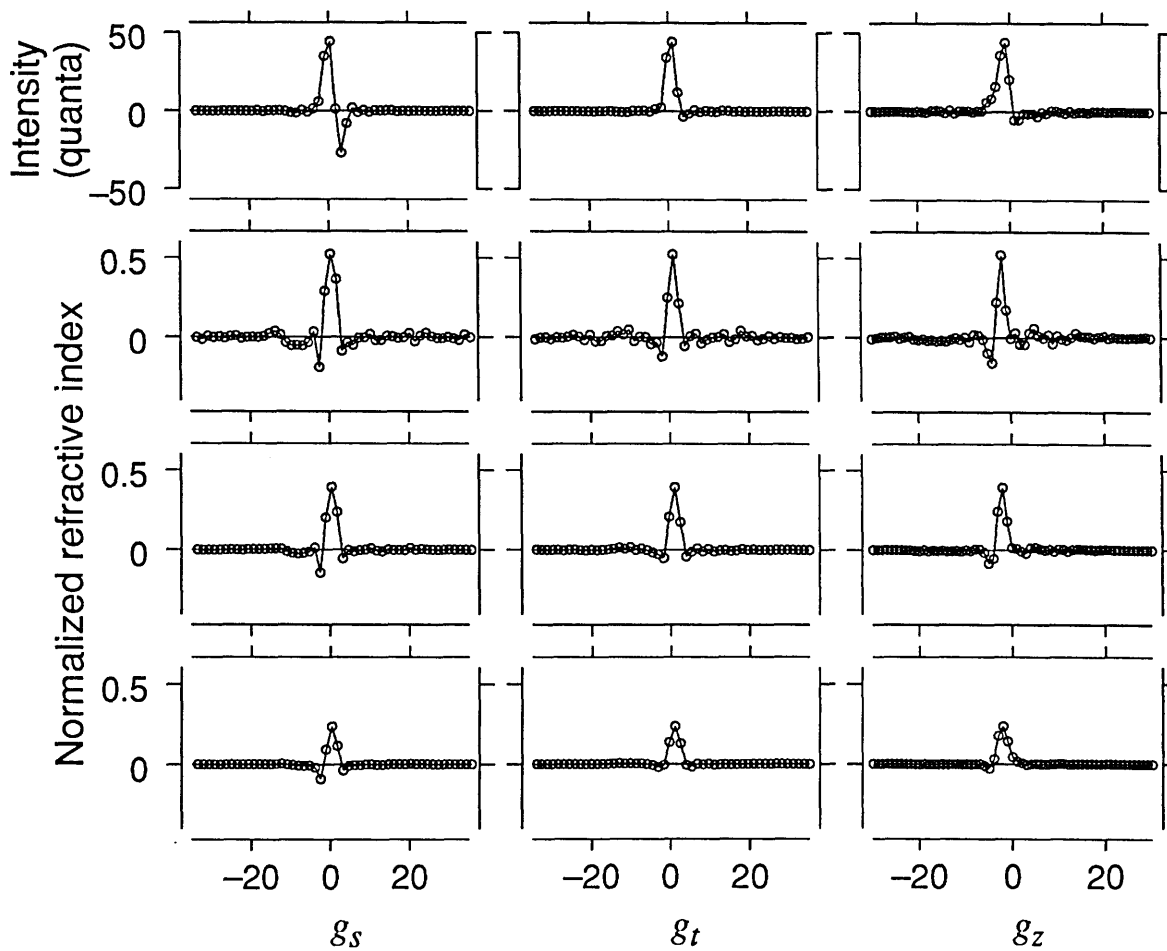
Plate 4.6

74

Plate 4.7

Figure 4-5: Deconvolution of 2.0 μm microsphere: plots. This figure shows intensity plots for the same data shown in Plates 4.6 and 4.7. The left panels show intensities along s for $g_t=g_z=0$. The center panels show intensities along t for $g_s=g_z=0$. The right panels show intensities along z for $g_s=g_t=0$.

Plate 4.8: Deconvolution of 2.8 μm microsphere images. Intensities from a 2.8 μm microsphere (51 $\times$ 51 $\times$ 39 voxels) were measured as described in Chapter 3 (i.e. with linear background subtraction and averaging) and are illustrated in Row A. The DC value was subtracted. The data were windowed with a three dimensional Hamming window [13] and deconvolved using Equation 4.13 with a measured PSF (Chapter 3). Results are shown for three different values of η: 10 (Row B), 1000 (Row C), and 10000 (Row D). Each row illustrates five images orthogonal to z: with $g_z = -2$ (left), -1, 0, 1, 2. Each image shows intensity variations for g_x from -19 to 19 and g_y from -19 to 19. The deconvolution was implemented using a 64^3 FFT.

Plate 4.9: Deconvolution of 2.8 μm microsphere images: z-y views. This plate shows z-y views of the same data shown in Plate 4.8.

structure of the microscope's PSF.

Increasing η had two effects on the deconvolutions shown in Plate 4.6, Plate 4.7, and Figure 4-5: it decreased the noise power in the background and blurred the reconstructed image. Blurring is most easily seen as decreases in the slopes of edges in Figure 4-5. Ideally, deconvolution would reconstruct an abrupt change in refractive index and the plots in Figure 4-5 would show rectangular pulses; the edges would have infinite slopes. Slopes in the reconstructions are greatest for the smallest value of η. For small values of η, the deconvolution filter acts like an inverse filter for higher frequencies. In effect, η defines a cutoff frequency above which the deconvolution filter ceases to look like the inverse filter. That cutoff frequency decreases as η increases and less high frequency information can be reconstructed. We see this as a decrease in slope in Figure 4-5 as η increases. Similar effects were observed for deconvolution of simulated images (Figure 4-4).

The normalized refractive index resulting from deconvolution depends on η. The maximum value decreases with increasing η (Figure 4-5). In order to accurately estimate refractive index, it is important to accurately estimate η.

Results for the 4.6 μm microsphere (Plate 4.10, Plate 4.11, and Figure 4-7) are qualitatively different from results for the 2.0 or 2.8 μm microsphere. In general the deconvolutions did not work as well as they did for the 2.0 and 2.8 μm microspheres. Results for $g_z = 0$ in Plate 4.10 can readily be interpreted as a circular region whose refractive index is greater than that of the background. Results for $g_z = -2$ suggest the implausible presence of regions with index less than that of the background.

A black halo surrounds the white circular region in the results for $g_z = 0$ in Plate 4.10. This halo is also present but less prominent in the 2.0 μm and 2.8 μm microsphere deconvolutions. The black halo can also be seen as negative dips in Figure 4-7. Ideally the transition from the background to the microsphere region
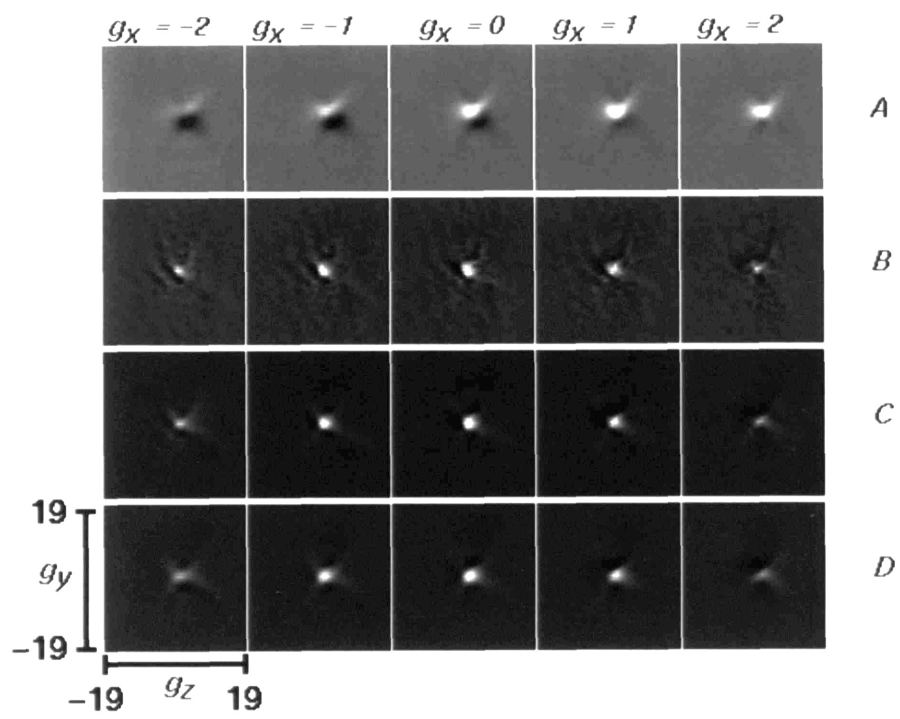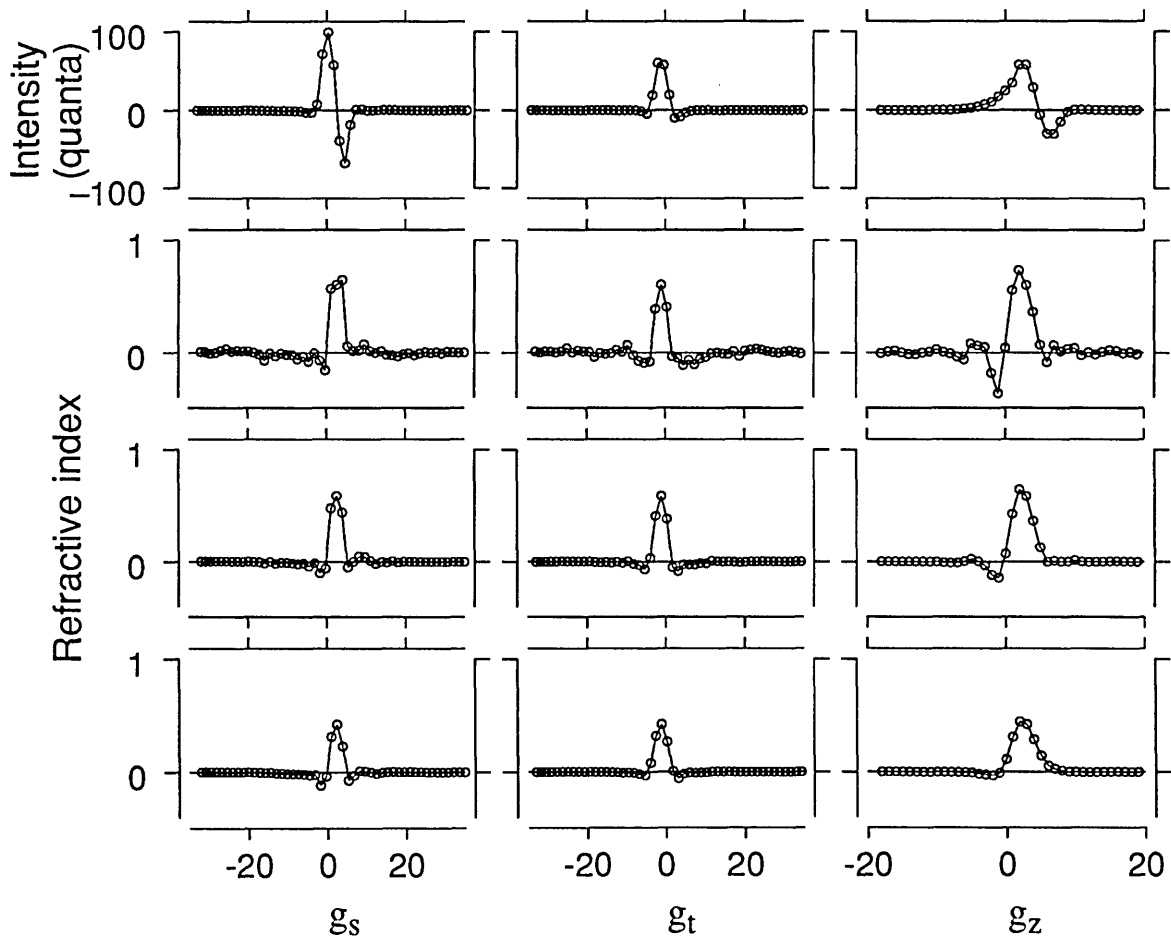
Plate 4.8

$g_X = -2$ $g_X = -1$ $g_X = 0$ $g_X = 1$ $g_X = 2$

A

B

C

19

g_y

−19

D

−19 g_z 19
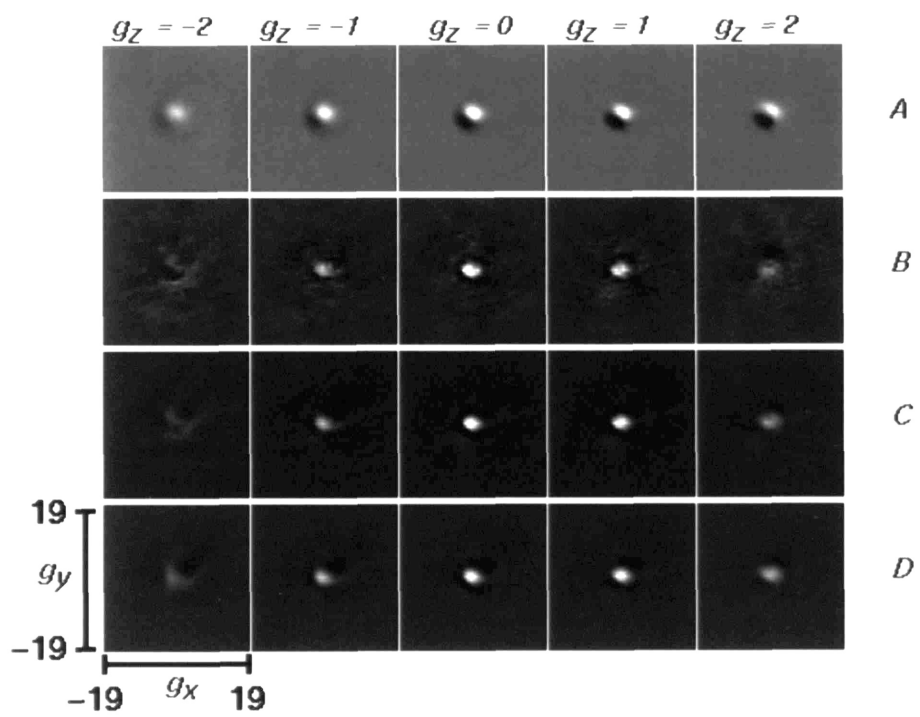
Plate 4.9

79

Figure 4-6: Deconvolution of 2.8 μm microsphere: plots. This figure shows intensity plots for the same data shown in Plates 4.8 and 4.9. The left panels show intensities along s for $g_t=g_z=0$. The center panels show intensities along t for $g_s=g_z=0$. The right panels show intensities along z for $g_s=g_t=0$.

Plate 4.10: Deconvolution of 4.6 μm microsphere images. Intensities from a 4.6 μm microsphere (61 $\times$ 61 $\times$ 61 voxels) were measured as described in Chapter 3 (i.e. with linear background subtraction and averaging) and are illustrated in Row A. The DC value was subtracted. The data were windowed with a three dimensional Hamming window [13] and deconvolved using Equation 4.13 with a measured PSF (Chapter 3). Results are shown for three different values of η: 10 (Row B), 1000 (Row C), and 10000 (Row D). Each row illustrates five images orthogonal to z: with $g_z = -2$ (left), -1, 0, 1, 2. Each image shows intensity variations for g_x from -19 to 19 and g_y from -19 to 19. The deconvolution was implemented using a 64^3 FFT.

Plate 4.11: Deconvolution of 4.6 μm microsphere images: y-z views. This plate shows y-z views of the same data shown in Plate 4.10.

would be appear as a step function in the plots. The dips result because high spatial frequencies are not reconstructed.

The original images of the 4.6 μm microsphere (Row A) are somewhat different from those for the 2.0 and 2.8 μm microspheres. For the smaller microspheres, the brightest and darkest intensities differed equally from the mean. However, for the 4.6 μm microsphere, the brightest intensity differed more from the mean. This may indicate that phase differences between sheared rays were too large for the linear approximation on which the model is based (See Section 2.6). If this were the case, nonlinear methods may be required for the reconstruction.

4.4 Applications to the TM

We applied these methods to the tectorial membrane of an alligator lizard (*Gerrhono-tus multicarinatus*). We show the results of a two data segments. The first segment is a tectorial membrane hole. This data was taken from a fixed alligator lizard TM mounted on a glass slide. The hole is shown in Row A of Plate 4.12, Plate 4.13 and Figure 4-8. The structure in the images in Row A of Plate 4.12 has an ambiguous interpretation. It gives the impression of an indentation of a defineable thickness, or it can also be interpreted as a circular protrusion of defineable thickness. In fact the apparent thickness is a function of the shear distance, not of the specimen's thickness (See Section 2.3). The deconvolution results are in Rows B, C, and D. The ambiguity of interpretation is removed by the deconvolution. The deconvolved images can easily be interpreted as a hole with refractive index lower than the background. As with the microsphere deconvolutions, increasing η reduced noise at the expense of high frequency reconstruction.
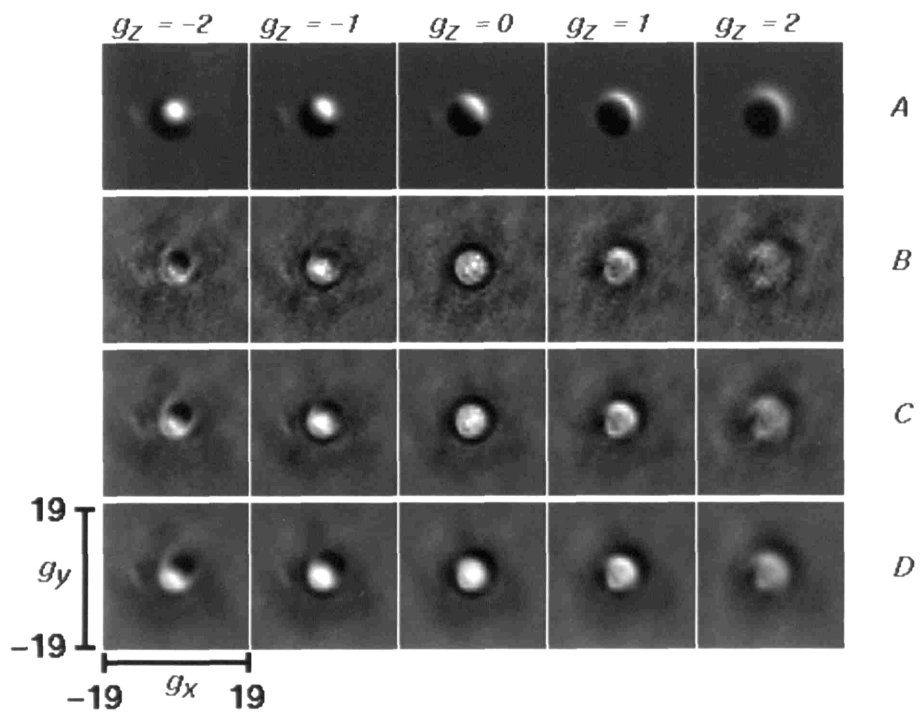
Plate 4.10

$g_x = -2$ $g_x = -1$ $g_x = 0$ $g_x = 1$ $g_x = 2$
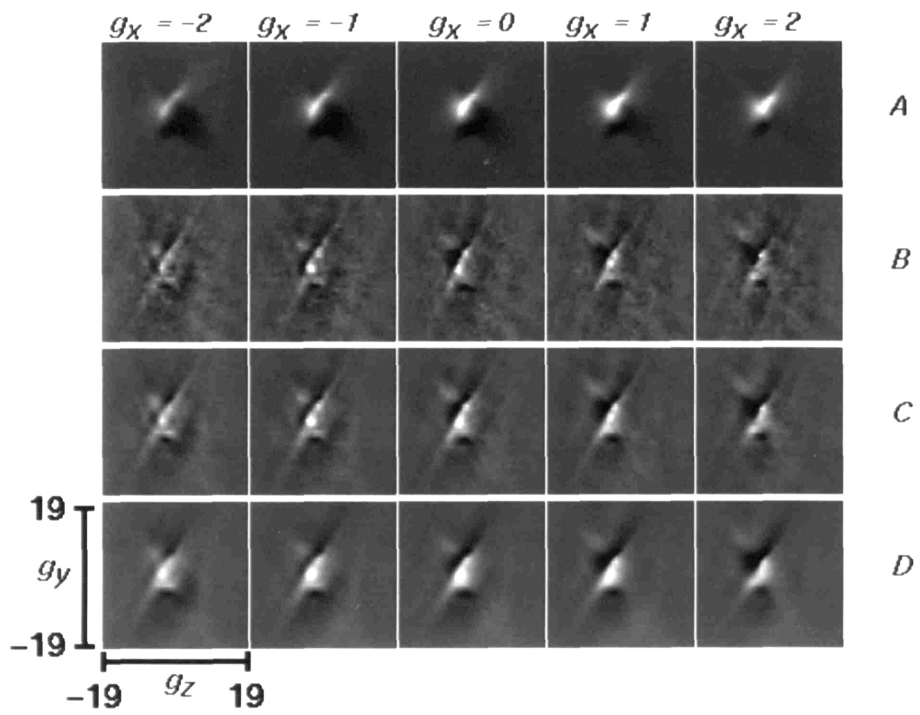
A

B

C

19
g_y
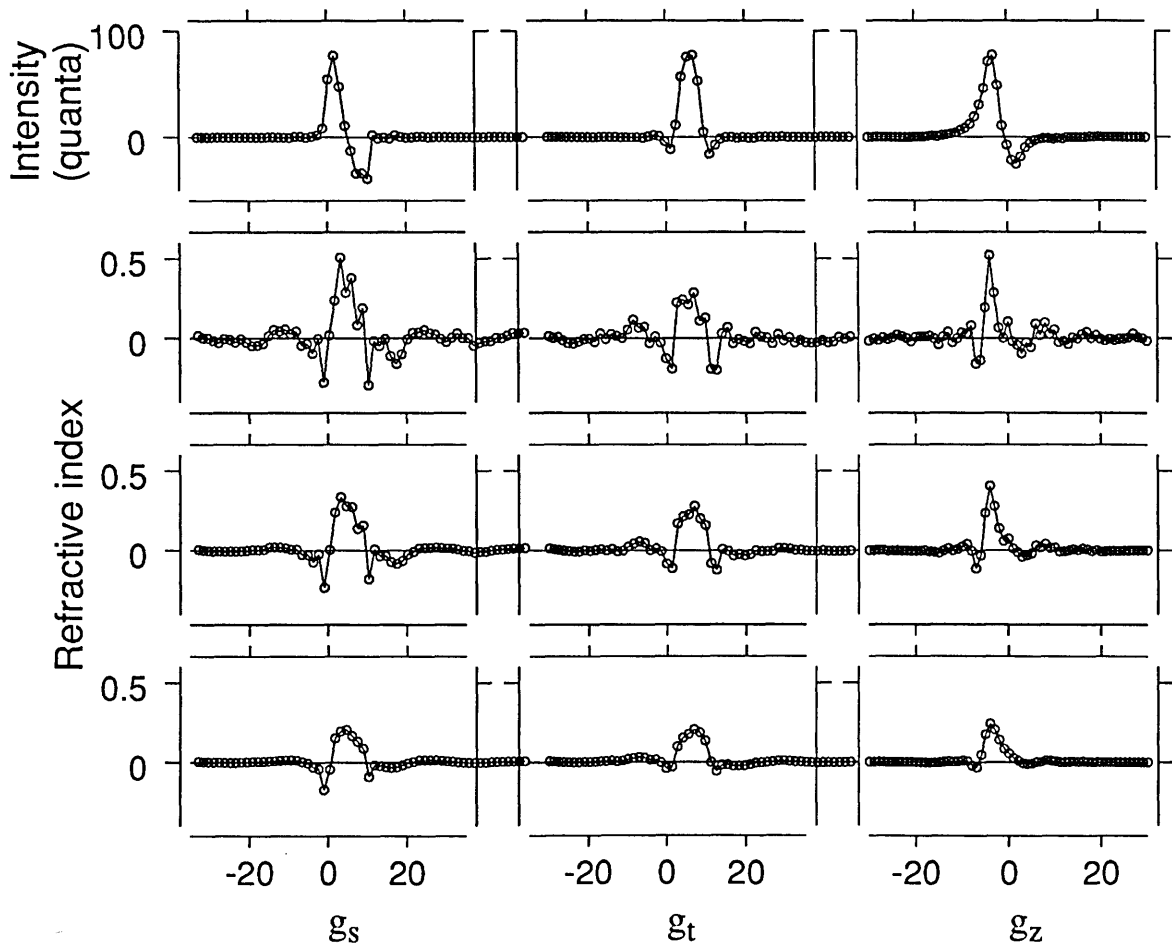−19

D

−19 g_z 19

Plate 4.11

Figure 4-7: Deconvolution of 4.6 μm microsphere: plots. This figure shows intensity plots for the same data shown in Plates 4.10 and 4.11. The left panels show intensities along s for $g_t=g_z=0$. The center panels show intensities along t for $g_s=g_z=0$. The right panels show intensities along z for $g_s=g_t=0$.

Plate 4.12: Images of a TM hole and its deconvolution. The sampled volume (51 ×
51 × 39 voxels) of a TM hole was processed by subtracting the DC value and by win-
dowing with a three dimensional Hamming window [13]. The data were deconvolved
using a measured PSF (processed as described in Chapter 3) and the deconvolution
filter in Equation 4.13 with $\eta = 10$ (Row B), 1000 (Row C), 10000 (Row D). The rows
illustrate five images along z with g_z = -2(left),-1,0,1,2. Each image shows variations
in g_x from -19 to 19 and g_y from -19 to 19.

Plate 4.13: Images of a TM hole and its deconvolution. This plate illustrates the
same TM and deconvolution as Plate 4.12 with a view of z -y planes.

The z-y images in Plate 4.13 explicitly show that the reconstruction of refractive
index works only in the shear direction. Notice that the values of z below and above
the hole in the deconvolution results do not have the same intensity as the interior
of the hole. We expect that they should because the regions have the same refractive
index. Because the DC value of the transfer function and the inverse filter are zero,
the values along the shear direction are reconstructed so as to preserve a zero average
value. Intensities in x-y planes both above and below the hole are near zero after
background subtraction. They remain near zero after the deconvolution. This is the
reason the intensity within the hole does not match that above the hole. This problem
can be resolved by deconvolving the data from the entire TM so that its boundaries
are within the sampled volume. We can then use the information that the background
volume has the same refractive index to recover the DC values in the shear direction.
This processing step has not been included in the deconvolution results shown and
remains a goal for future work.

A DIC image of an alligator lizard TM is shown in Plate 4.14. A subvolume
from the alligator lizard TM was deconvolved. One plane of this volume is shown
before and after deconvolution in Plate 4.15. The deconvolved TM makes certain
structural characteristics apparent. For instance, the original TM image has the
problem of ambiguity in structural interpretation of holes. That is, the holes look like
indentations or protrusions of a certain thickness. The deconvolved version resolves
that ambiguity; the holes clearly appear to be regions of lower refractive index. Also
small protrusions of higher refractive index are more apparent in the upper part of
the hole in the deconvolved result. Another small hole in the center of the image of
lower refractive index is visible in the deconvolved image. This feature is difficult to
identify in the original image.

Results in this section show that these image processing methods are valuable for
studying DIC images of the tectorial membrane and suggest that they are generally
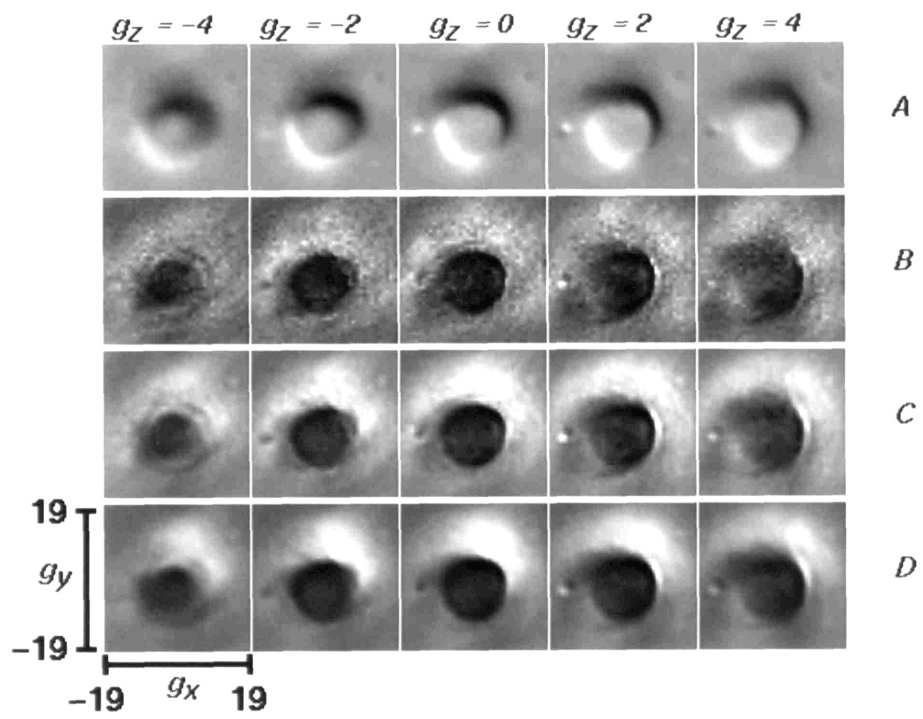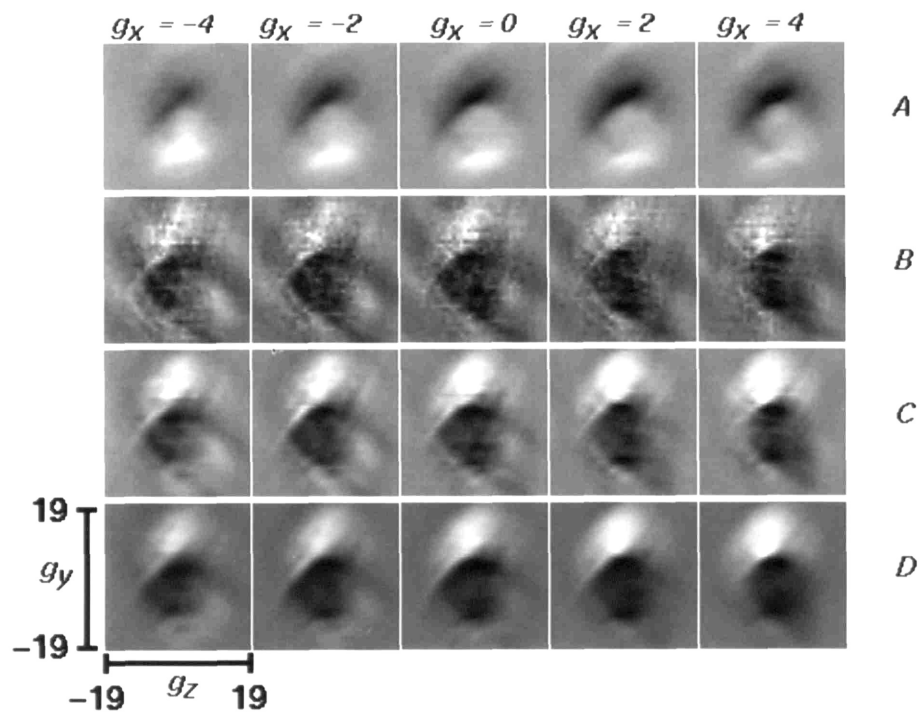applicable.
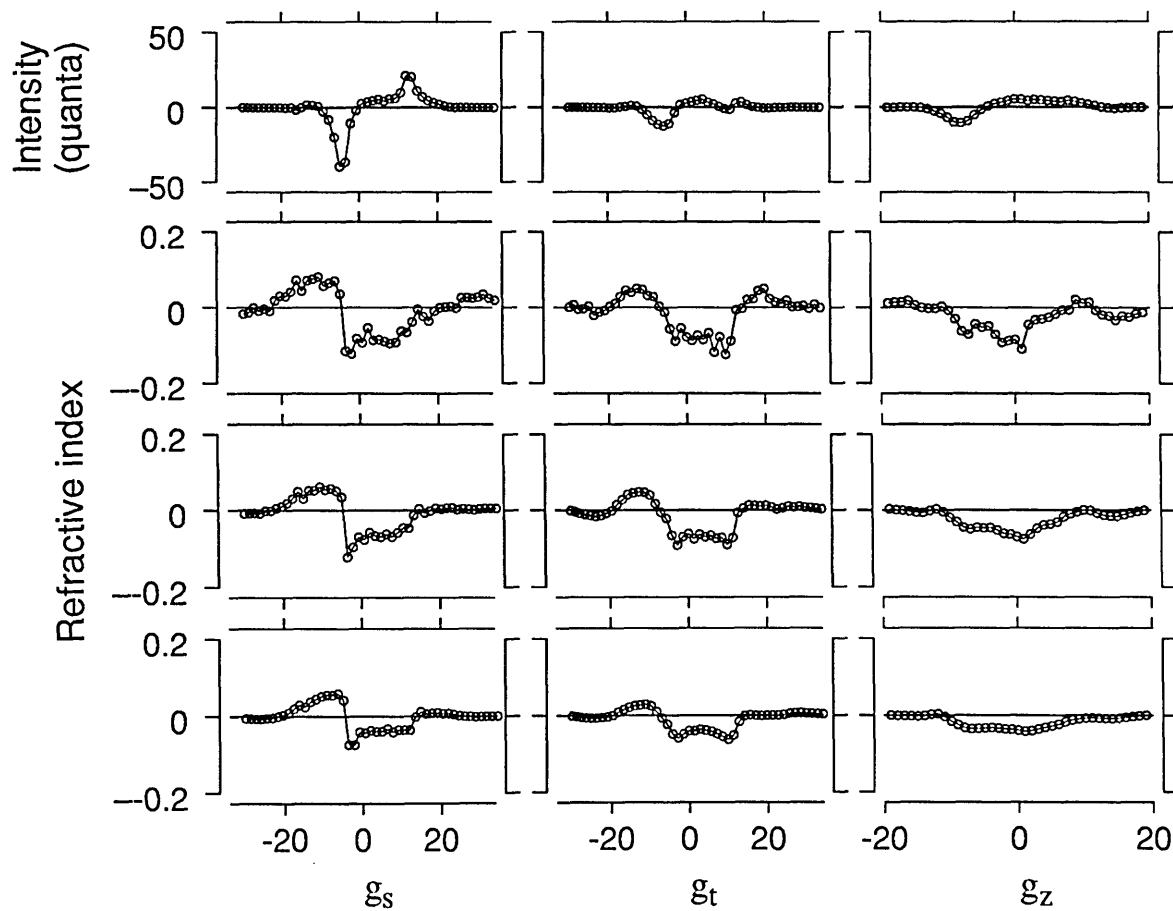
Plate 4.12

86

Plate 4.13

Figure 4-8: A TM hole and its deconvolution. This figure illustrates the same TM and deconvolution as Plate 4.12 as plots of intensity along s (left), t (middle) and z (right). The data are deconvolved using a measured PSF (processed as described in Chapter 3) and the deconvolution filter in Equation 4.13 with $\eta = 10$ (Row B), 1000 (Row C), 10000 (Row D).

Plate 4.14: A DIC image of the TM of an alligator lizard for one x-y plane. The TM was isolated from the cochlear duct and immersed in an artificial endolymph solution (concentrations in 10^{-3} molar: K^+ 171, Na^+ 2, Ca^{2+} 0.02, Dextrose 3, HEPES buffer 5) to mimic its native environment[5].
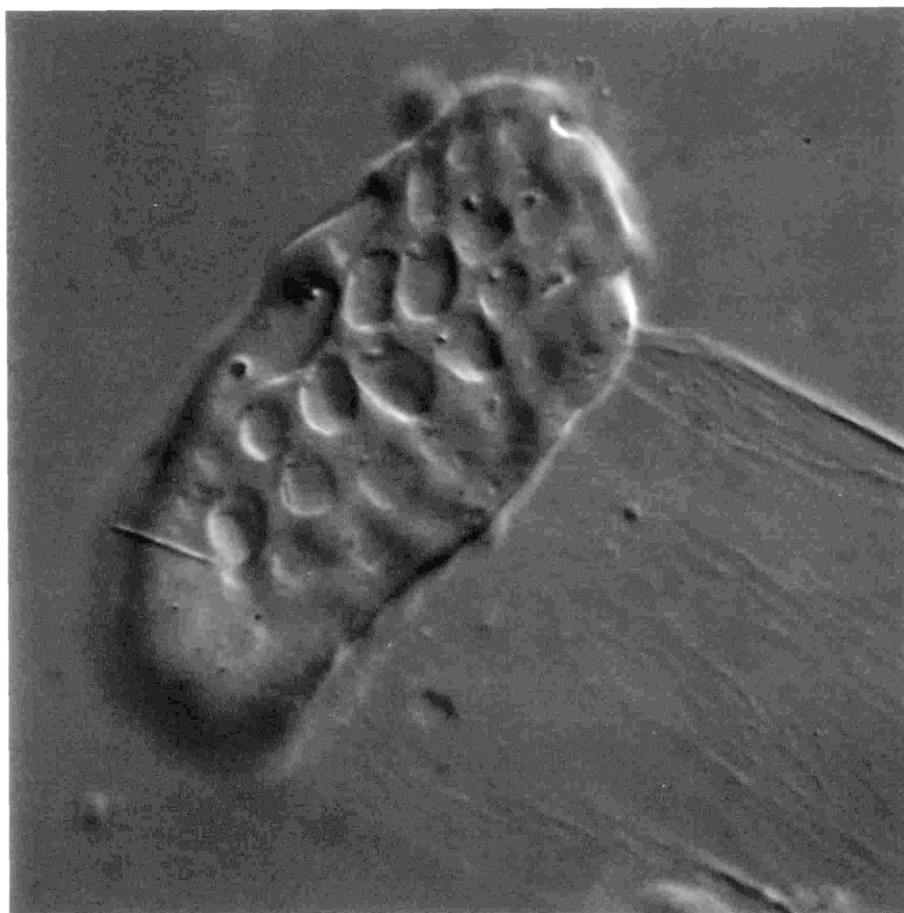
Plate 4.14

Plate 4.15: Images of a TM and its deconvolution. The subvolume ($128 \times 128 \times 50$) of an isolated TM shown in Plate 4.14 was processed by subtracting the DC value. It was deconvolved using a measured PSF (processed as described in Chapter 3) and the deconvolution filter in Equation 4.13 with $\eta = 1000$ The top image shows one x-y image of the subvolume. The bottom image shows the deconvolution results. The deconvolution was performed with 128^3 FFTs.
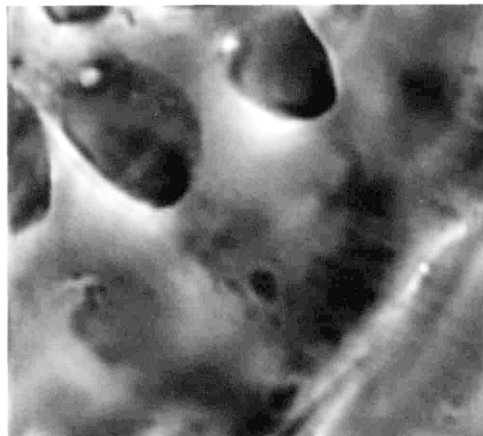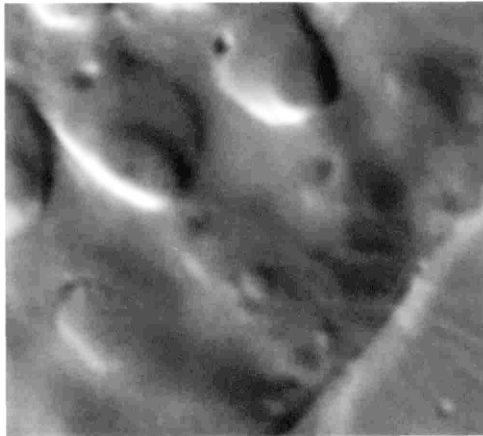
Plate 4.15

Chapter 5

Discussion

We illustrated a method for three-dimensional reconstruction of an object based on DIC microscope images. A signal processing model of the DIC microscope was developed. Parameters of this model for our microscope were measured. Deconvolution based on this model was used to reconstruct 3D objects. The methods were tested on simulated and measured data. We were able to reconstruct normalized refractive index gradients in the shear direction. In general, the reconstructed results were a better representation of the object's physical structure than the original images.

For the deconvolution tests, small microspheres were reconstructed more accurately than large spheres. This inaccuracy may be a result of the model assumption that the specimen only phase-shifts light that passes through. In fact, this light is refracted and scattered. The microspheres act as lenses, focusing light to a point. The larger microspheres refract more light and therefore cause greater inaccuracies.

There are several aspects of this project which need further developing. First the validity of the model needs to be examined. The theoretical PSF and measured PSF differ (see Section 3.4). This suggests deficiencies in our model. Currently, we use a measured PSF to construct the deconvolution filter. If the model were made more accurate, an analytical PSF could be used in the deconvolution. Deconvolution results would then be less sensitive to measurement degradations.

If a measured PSF is essential to the method, the measurement could be further optimized. We have not attempted to determine the minimum amount of processing necessary to obtain an accurate PSF measurement. Each PSF measurement is averaged ($100\times$) and background subtracted (see Chapter 3). The PSF measurement is repeated before collecting data on a given day to compensate for slight changes in the microscope configuration. This procedure is time-consuming and could be unnecessarily conservative.

For the deconvolution described in Chapter 4, future work includes developing a better estimate of noise to signal ratio. We currently use a constant approximation. In

the test with simulated microscope images we've identified noticeable effects of using this suboptimal estimate. Consequently, improving the estimate may significantly improve the results.

Throughout Chapter 4, we report our results in terms of normalized refractive index. We are currently implementing a calibration scheme based on mapping phase to intensity using the calibrated slider Wollaston prism (see Section 3.1.3). This calibration removes the effects of gain and offset that vary with microscope illumination and camera gain/offset settings. This calibration allows us to obtain repeatable numerical results. It shows promising progress toward the goal of interpreting the results in terms of the absolute refractive index.

Bibliography

[1] David A. Agard. Optical sectioning microscopy: Cellular architecture in three dimensions. *Annual Review of Biophysics and Bioengineering*, 13:191, 1984.

[2] David A. Agard, Yasushi Hiraoka, Peter Shaw, and John W. Sedat. Flourescence microscopy in three dimensions. *Methods in Cell Biology*, 30:353, 1989.

[3] Max Born. *Principles of Optics*. Pergamon Press, New York, 1975.

[4] Dennis M. Freeman, Douglas A. Cotanche, Farzad Ehsani, and Thomas F. Weiss. Effect of Na^+, K^+, and Ca^{2+} concentration on the isolated tectorial membrane of the chick. In preparation.

[5] Dennis M. Freeman, Donna Hendrix, Devang Shaw, Leslie Fan, and Thomas F. Weiss. Effect of lymph composition on an *in vitro* preparation of the alligator lizard cochlea. Submitted to *Hearing Research*, 1992.

[6] W. Galbraith and G. B. David. An aid to understanding differential interference contrast microscopy: computer simulation. *Journal of Microscopy*, 108:147, 1976.

[7] Sarah Frisken Gibson and Fredrick Lanni. Diffraction by a circular aperture as a model for three dimensional optical microscopy. *Journal of the Optical Society of America A*, 6(9):13, 1989.

[8] Joseph W. Goodman. *Introduction to Fourier Optics*. McGraw Hill Book Company, New York, 1968.

[9] John S. Hartman, Richard L. Gordon, and Delbert L. Lessor. Quantitative surface topography determination by Nomarski reflection microscopy. *Applied Optics*, 19(17):2998, 1980.

[10] Shinya Inoué. *Video Microscopy*. Plenum Press, New York, 1986.

[11] H. Ernst Keller. *Handbook of biological confocal microscopy*, chapter 7: Objective lenses for confocal microscopy, page 77. Plenum Press, 1990.

[12] Walter Lang. Nomarski differential interference contrast microscopy. Technical report, Carl Zeiss, Inc., Oberkochen, West Germany, 1971.

[13] Jae S. Lim. *Two Dimensional Signal and Image Processing.* Prentice Hall, Englewood Cliffs, NJ, 1990.

[14] Alan Oppenheim and Ronald Schafer. *Discrete Time Signal Processing.* Prentice Hall, Englewood Cliffs, NJ, 1989.

[15] Jacques Padawer. The Nomarski interference contrast microscope: An experimental basis for image information. *Journal of the Royal Microsopy Society,* 88:305, 1968.

[16] Maksymilian Pluta. *Advanced Light Microscopy,* volume 2. Elsevier, New York, 1989.

[17] William H Press, Brian P. Flannery, Saul A. Teukolsky, and William T. Vettering. *Numerical Recipes in C.* Cambridge University Press, Cambridge, 1988.

[18] L. Tella. The determination of a microscopes's three dimensional transfer function for use in image reconstruction. Master's thesis, Worcester Polytechnic Institute, Worcester, MA, 1985.

[19] J. J. Zwislocki and L. K. Cefaratti. Tectorial membrane II: stiffness measurements *in vivo. Hearing Research,* 42:211, 1989.